UNIVERSITY OF SUSSEX

Measuring the Muon Neutrino Magnetic Moment in the NOvA Near Detector

Róbert Králik

Supervisor: Dr. Lily Asquith

A thesis submitted in fulfilment of the requirements for the degree of Doctor of Philosophy to the

School of Mathematical and Physical Sciences
University of Sussex

In Brighton, United Kingdom July 14, 2024

I hereby declare that I carried out this thesis independently, and only with the cited sources, literature and other professional sources.

I also declare that this thesis has not been and will not be, submitted in whole or in part to another University for the award of any other degree.

Brighton, United Kingdom,
July 14, 2024

Róbert Králik

Acknowledgements

School of Mathematical and Physical Sciences, University of Sussex

DOCTORAL THESIS

Measuring the Muon Neutrino Magnetic Moment in the NOvA Near Detector

---

by Róbert Králik

ABSTRACT

Measuring an enhanced neutrino magnetic moment would be a clear indication of physics beyond the Standard Model (BSM), shedding light on the correct BSM theory or the potential Majorana nature of neutrinos. It would manifest in the NOvA near detector as an excess of neutrino-on-electron elastic scattering interactions at low electron recoil energies. Leveraging an intense and highly pure muon neutrino beam, along with the finely segmented liquid scintillator detector technology specifically designed for electromagnetic shower separation, enables NOvA to achieve a potentially world-leading sensitivity in probing the effective muon neutrino magnetic moment. Despite facing statistical limitations stemming from the low cross section of the signal process, systematic uncertainties have a significant impact on this result. To address these challenges, the NOvA Test Beam experiment focuses on mitigating some of the largest systematic uncertainties within NOvA by investigating particle interactions and energy deposition in a small-scale replica NOvA detector. This thesis describes the calibration of the NOvA Test Beam detector, which is a crucial step in analysing the Test Beam data before they can be utilised to reduce NOvA systematic uncertainties.COMMENT: *Add final numbers for the analyses, also the POT and such*

Keywords: neutrino NOvA electromagnetic testbeam calibration

Contents

List of Figures

List of Tables

Preface

In this Preface, I provide an overview of the research presented in this thesis, highlighting my personal contributions to the work presented in each chapter.

Chapter **??** presents a comprehensive overview of the relevant literature on neutrinos and their place in the particle physics theory and experiments.

Chapter 1 introduces the NOvA experiment with a complete overview to its technical aspects relevant to either the measurement of the effective muon neutrino magnetic moment, or to the calibration of the NOvA Test Beam detector. This chapter is mainly a collection of work of my NOvA collaborators, their technical design reports for the NOvA experiment and official results. My only contribution to this chapter lies in the addition of new external measurements from the NA61 experiment, to improve the neutrino beam prediction in NOvA.

Chapter **??** details the calibration of the NOvA Test Beam detector, divided into three main sections.

Section **??** describes the Test Beam detector itself, as designed and constructed by my NOvA Test Beam experiment colleagues.

Section **??** presents the data-based simulation of cosmic muons used for the calibration, which originates as a simpler version of the simulation by my colleague. I then improved the event selection, implemented the energy and charge assignment, and produced and validated the simulation and the corresponding calibration samples.

Lastly, Sec. **??** describes the Test Beam detector calibration itself, which uses the NOvA codebase for calibration. I fully implemented the NOvA calibration

Chapter 2 describes the measurement of the effective muon neutrino magnetic moment. Introduces the experimental and theoretical context for the measurement, describes the details of the analysis, including the event selection and the systematic uncertainties and describes the results and discusses their implications.

Finally, chapter **??** concludes the findings of this thesis.

Data-based Simulation of Cosmic Muons

I also inherited the first-version of the data-based simulation of cosmic muons for the Test Beam detector. However, this version of the simulation was just directly taken from the simulation of the muon-removed sample and did not work properly for the Test Beam detector.

I developed and validated the event selection of cosmic muons for the data-based simulation, implemented the energy and charge correction. I developed the data-based simulation of cosmic muons described in Sec. Specifically, I developed the event selection, implemented the energy and charge corrections, actually produced the simulation and the calibration samples, and validated them

Calibration of the NOvA Test Beam Detector

The Test Beam detector calibration (Sec. **??**) uses the same calibration techniques as are used for the other NOvA detectors. I inherited the Test Beam detector calibration when it was technically working, but not for simulation. Therefore, I was the first person to calibrate the simulated Test Beam detector and therefore complete the entire Test Beam detector calibration chain. This allowed for the first proper production of data for the Test Beam analysers. Starting from here, I included the fibre brightness for the Test Beam detector in the same way as is used for the Near and Far NOvA detectors (Sec. **??**).

I implemented the NOvA calibration procedure in full for the Test Beam calibration, specifically adding the Fibre Brightness dependency and implementing it for all the data and simulation samples. I've created my own fibre brightness maps, my own threshold and shielding corrections (found out about the issue), improved the NOvA calibration code, made the attenuation fits for all the samples, did the same for absolute calibration, figured out there is a mistake in geometry, figured out we need to add the underfilled cells to the dead channels, changed the TS correction limits, improved the systematic uncertainty for the absolute calibration, validated the calibration, developed code for the validation

Measurement of the Effective Muon Neutrino Magnetic Moment

I was just told its an interesting analysis, there was a previous NOvA thesis, but it wasn't very well developed, did not use the standard NOvA techniques and did not properly incorporate systematics into their fits/limits. From the ND group, I got the event classifier and the event selection, which however did not work very well for our signal. Additionally, I got the nuone and the nueccmec enhanced samples and the radiative correction weight from them. From NOvA in general I got the nominal ND sample and the data sample, the cross section and PPFX weights and the fitting infrastructure in general. From the LDM analysis I got the general structure of the fitting framework.

I have done the literature review of what is the neutrino magnetic moment and what are its current limits and state of the art measurements. I designed the neutrino magnetic moment weight and developed my own event selection, including using the TMVA, which is not used elsewhere, and the general analysis infrastructure for the neutrino magnetic moment ana. I helped (re)produce the systematic samples for the nueccmec enhanced sample. Technically I also investigated the nominal ND sample and whether it would be better to use the decaf sample, but this led nowhere... Technically I also analysed the electron recoil energy and angle resolution and decided on the binning (although not finished and talked about here). I did the systematics study and implemented the systematic shifts for the detector systematics for numm. I implemented the fitting framework for the neutrino magnetic moment analysis for both the template fit (not used here) and the counting experiment. I did the actual fit and got the final results.

Chapter 1

The NOvA Experiment

The NuMI Off-axis ν_e Appearance (NOvA) [1] experiment is a long-baseline neutrino oscillation experiment based at the Fermi National Accelerator Laboratory (Fermilab) [2]. NOvA receives an off-axis ν_μ and $\overline{\nu}_\mu$ beam from Fermilab's Neutrinos from the Main Injector (NuMI) neutrino source (Sec. 1.1) and measures ν_e or $\overline{\nu}_e$ appearance and ν_μ or $\overline{\nu}_\mu$ disappearance between its two highly active and finely segmented detectors (Sec. 1.4) [3].

The capability to measure both ν_e and the $\overline{\nu}_e$ appearance, coupled with a significant matter effect induced by its long baseline, allows NOvA to address some of the most important questions in neutrino physics to date, such as the neutrino mass ordering, the octant of θ_{23}, and the possible Charge conjugation - Parity (CP) symmetry violation in the neutrino sector [3–7]. NOvA data also enables measurements of θ_{13}, θ_{23} and $|\Delta m^2_{32}|$ [3], measurements of neutrino differential cross sections in the Near Detector (ND) [8–11], constraints on possible sterile neutrino models [12, 13], monitoring for supernova neutrino activity [14, 15], searches for magnetic monopoles [16], and constraints on the neutrino electromagnetic properties (this thesis). Using two functionally identical detectors mitigates the dominant systematic uncertainties of neutrino oscillation measurements, described in Sec. 1.8.

NOvA started taking data in February 2014 and is expected to run through 2026 [17], or until Fermilab begins redirecting its efforts towards the startup of the upcoming Deep Underground Neutrino Experiment (DUNE) experiment [18].

1.1 The Neutrino Beam

The neutrino beam for NOvA comes from the Fermilab-based NuMI neutrino source [19]. The schematic description of NuMI is shown in Fig. 1.1, starting on the left hand side with $120\,\mathrm{GeV}$ protons from the Main Injector (MI), part of the Fermilab accelerator complex. The proton beam is divided into $10\,\mu s$ long pulses, with $\sim 5 \times 10^{13}$ Protons On Target (POT) per spill every $\sim 1.3\,s$ long cycle time, resulting in a proton beam power of $\sim 800\,kW$ (current record $959\,kW$ [20]), with upgrades currently underway to surpass $1\,MW$ [21].

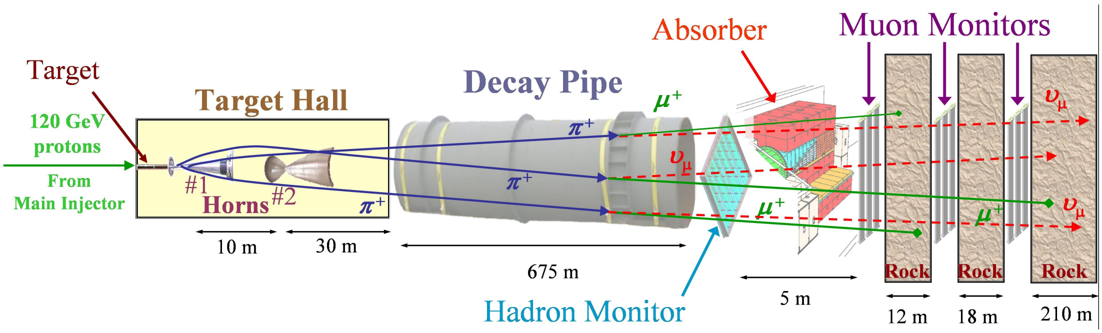

Figure 1.1: The NuMI neutrino beam starts on the left hand side with protons from the MI impinged on a graphite target producing mainly pions and kaons. These are then focused and charge-selected by two focusing horns, after which they decay inside the decay pipe into a high-purity ν_μ or $\overline{\nu}_\mu$ beam. The residual hadrons are stopped and monitored in the hadron absorber and the remaining muons are recorded with muon monitors and absorbed inside the rock. Figure from [19].

The proton beam passes through a collimating baffle before hitting a $\sim 1.2\,m$-long (equal to about two interaction lengths) graphite target [22], producing hadrons, predominantly pions and kaons [19]. These are then focused and selected by two parabolic magnetic 'horns'. The focused hadrons pass through a $675\,m$-long decay pipe filled with helium to create a low density environment for hadrons to propagate and decay in flight into either neutrinos or antineutrinos. High energy hadrons that do not decay in the decay pipe are absorbed within a massive aluminium, steel, and concrete hadron absorber and monitored with a hadron monitor. The leftover muons are ranged out in dolomite rock after the absorber and monitored using three muon monitors. The hadron and muon monitors are ionization chambers, used to monitor the quality, location and relative intensity of the beam.

Using a positive current inside the horns focuses positively charged particles, which then decay into neutrinos, and removes negatively charged particles. Reversing the horn current focuses negatively charged particles, which decay into antineutrinos, and defocuses positively charged particles. The neutrino mode is therefore called Forward Horn Current (FHC) and the antineutrino mode is called Reverse Horn Current (RHC). The composition of the neutrino beam for both these modes at the NOvA ND is shown in Fig. 1.2, displaying the very high purity of the ν_μ or $\overline{\nu}_\mu$ component in the FHC ro RHC beam respectively [19].

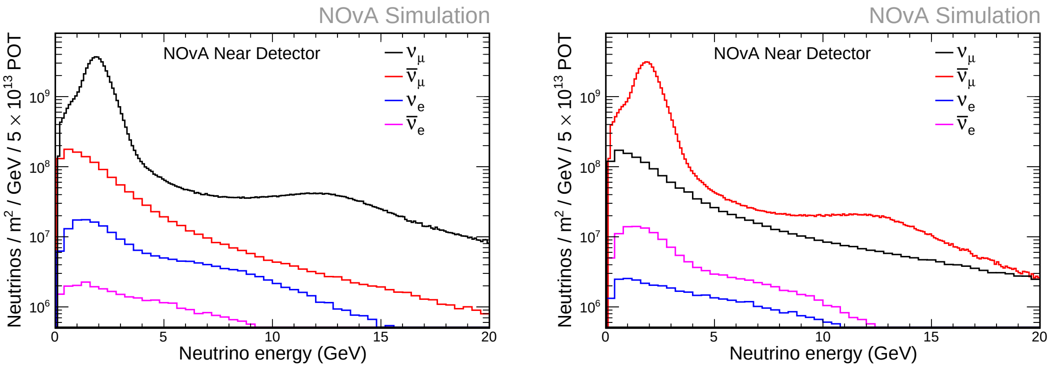

Figure 1.2: The components of the neutrino beam at the NOvA ND per one NuMI spill in the FHC regime shown on the left and the RHC regime on the right. The ν_μ ($\overline{\nu}_\mu$) composition in the FHC (RHC) regime is 93.8% (92.5%), with a wrong sign contribution of 5.3% (6.6%) and only 0.9% (0.9%) contamination by ν_e ($\overline{\nu}_e$), showing the high purity of ν_μ and $\overline{\nu}_\mu$ in the neutrino beam for NOvA. Beam composition values calculated for neutrinos with energies between $1-5\,\mathrm{GeV}$. Figures are from internal NOvA repository [23].

The resulting neutrino beam energy distribution is peaked at $\sim\ 7\,\mathrm{GeV}$ with a wide energy band. However, thanks to the kinematics of the dominant pion decay, by placing the NOvA ND and Far Detector (FD) $14.6\,\mathrm{mrad}$ ($\approx\ 0.8\,^\circ$) off the main NuMI beam axis, NOvA achieves a narrow band neutrino flux peaked at $1.8\,\mathrm{GeV}$ [7, 24], as can be seen in Fig. 1.3. Using an off-axis neutrino flux increases the neutrino beam around $2\,\mathrm{GeV}$ about 5-fold compared to the on-axis flux and narrow-band peak enhances background rejection for the ν_e appearance analysis [24].

1.2 The NOvA Detectors

The two main NOvA detectors are the ND, located in Fermilab $\sim\ 1\,\mathrm{km}$ from the NuMI target and $\sim\ 100\,\mathrm{m}$ under ground, and the FD, located $\sim\ 810\,\mathrm{km}$ from Fermilab at Ash River in north Minnesota, partially underground with a rock overburden [24]. NOvA also operated a detector prototype called Near Detector on the Surface (NDOS), which was used for early research and development of detector components and analysis [4]. Additionally, NOvA operated a Test Beam detector, described in detail in Sec. ??. The scales of the ND and FD are shown in Fig. 1.4.

All NOvA detectors are highly segmented, highly active, functionally identical

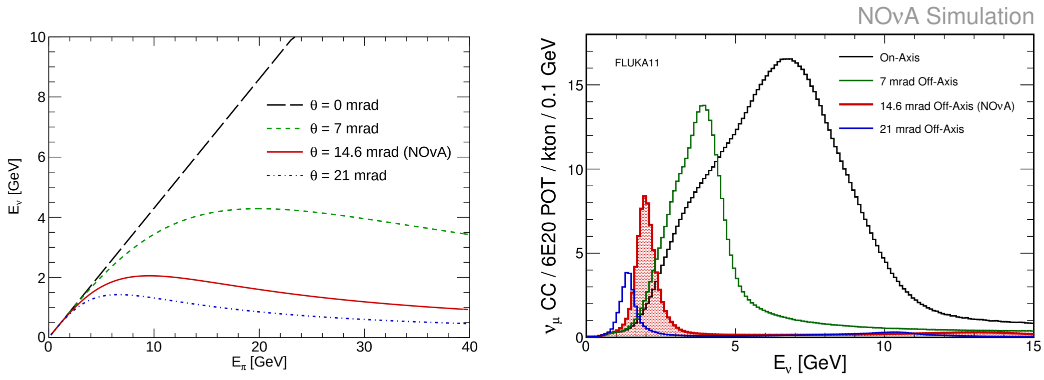

Figure 1.3: (Left) Dependence of the neutrino energy on the parent pion's energy and (right) neutrino energy distribution for an on-axis beam and three different off-axis beam designs. The case for NOvA is shown in red and results in a narrow neutrino energy distribution around $2\,\mathrm{GeV}$, with limited dependence on the parent pion's energy. Figure from [24]

tracking calorimeters made up of Polyvinyl chloride (PVC) cells filled with liquid scintillator. Each cell is a long rectangular cuboid with depth of $5.9\,\mathrm{cm}$ and width of $3.8\,\mathrm{cm}$ (with some variations), with cell length extending to the full width/height of each detector, which is $\sim 4.1\,\mathrm{m}$ for the ND and $\sim 15.6\,\mathrm{m}$ for the FD [24]. An example of a FD cell is shown on the right of Fig. 1.4.

Cells are connected side-by-side into a 16 cell-wide extrusions with $3.3\,\mathrm{mm}$-wide walls between cells and $4.9\,\mathrm{mm}$-wide walls on the outsides of the extrusions. The first and last cell of each extrusion are $\sim 3\,\mathrm{mm}$ narrower than the rest of the cells. Two extrusions are connected side-by-side to form a 32 cell-wide module, with each module having a separate readout (see Sec. 1.3). In the FD, 12 modules are connected side-by-side to form one plane of the detector. In the ND only 3 modules make up a plane. Planes are positioned one after another, alternating between vertical and horizontal orientation, and grouped into diblocks, each containing 64 planes. The FD contains 14 diblocks, totalling 896 planes, whereas the ND contains 3 diblocks totalling 192 planes. The ND also contains a Muon Catcher region, positioned right after the active region, consisting of 22 planes of the normal NOvA detector design, 2 modules high and 3 modules wide, sandwiched with 10 steel plates to help range out muons mainly from the ν_μ charged current interactions [4, 24].

The NOvA coordinate system is centred with $(0, 0, 0)$ in the centre of the first plane, relative to the beam direction. The x axis runs from left to right when facing the detector, y axis from bottom to top and z axis runs perpendicular to the planes

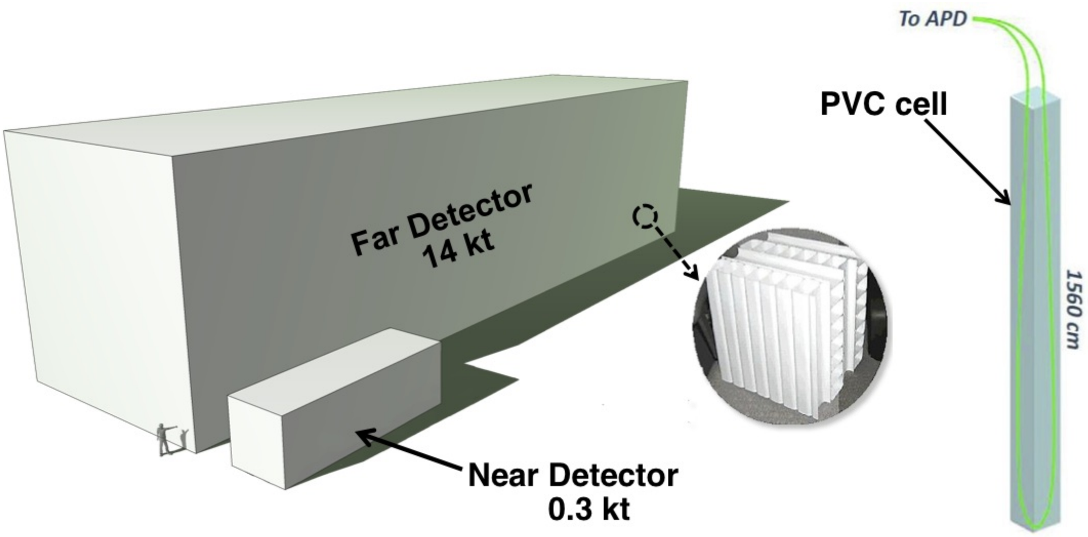

Figure 1.4: Schematic description of the scale and composition of the NOvA ND and FD. The inset shows a photo of the orthogonal planes made out of PVC cells. An example of a FD cell containing liquid scintillator and a looped WLS fibre attached to an APD is shown on the right [25].

along the beam direction.

Each cell is filled with a liquid scintillator consisting of mineral oil with 4.1% pseudocumene as the scintillant [26]. Each cell contains a single wavelength shifting fibre with double the length of the cell, looping at one end and connecting to the readout at the other. The PVC walls of the cells are loaded with highly reflective titanium dioxide, with light typically bouncing off the PVC walls ~ 8 times before being captured by the Wavelength Shifting (WLS) fibre [24].

The final dimensions of the FD are $15.6\,\mathrm{m} \times 15.6\,\mathrm{m} \times 60\,\mathrm{m}$ with a total mass of $14\,\mathrm{kT}$ and for the ND the dimensions are $3.8\,\mathrm{m} \times 3.8\,\mathrm{m} \times 12.8\,\mathrm{m}$ with a mass of about $0.3\,\mathrm{kT}$ [17]. The active volume, consisting only of the liquid scintillator without the PVC structure, makes up about 70% of the total detector volume [24].

The NOvA detectors are specifically designed for electromagnetic shower identification, with a radiation length of $38\,\mathrm{cm}$, which amounts to ~ 7 planes for particles travelling perpendicular to the detector planes [4]. This is particularly useful to distinguish electrons from π^0s.

We can calculate the minimum energy an electron needs to have to cross one cell ($5.9\,\mathrm{cm}$) of the NOvA detector by using the measured scintillator density $0.86\,\mathrm{g/cm^3}$ [27], which gives us the required range of $\sim 5\,\mathrm{g/cm^2}$. Comparing this to measured values for the electron range [28] in the continuous slowing down approximation in a Polyethylene (approximation of the NOvA scintillator [29]), gives us an estimate of the lowest detectable electron energy as $E_e \gtrsim 10\,\mathrm{MeV}$.

1.3 Readout and Data Acquisition

The signal from the WLS fibres is read out by an Avalanche Photodiode (APD), converting the scintillation light into electrical signal, with a high quantum efficiency of $\sim 85\%$ and a gain of 100 [24]. An example APD is shown in Fig. 1.5. Both ends of each fibre correspond to a single readout channel and are connected to one of the 32 pixels on the APD, organized in four rows of 8 pixels, with each APD reading out signal from one module. To maximise the signal to noise ratio, the APDs are cooled to $-15\,^{\circ}\mathrm{C}$ by a thermoelectric cooler, with heat carried away by a water cooling system.

The combination of the APD quantum efficiency and the light yield, determined by the PVC reflectivity and the scintillator and WLS fibre responses, result in a signal requirement of at least 20 Photo Electron (PE) in response to minimum ionizing radiation at the far end of the FD cell.

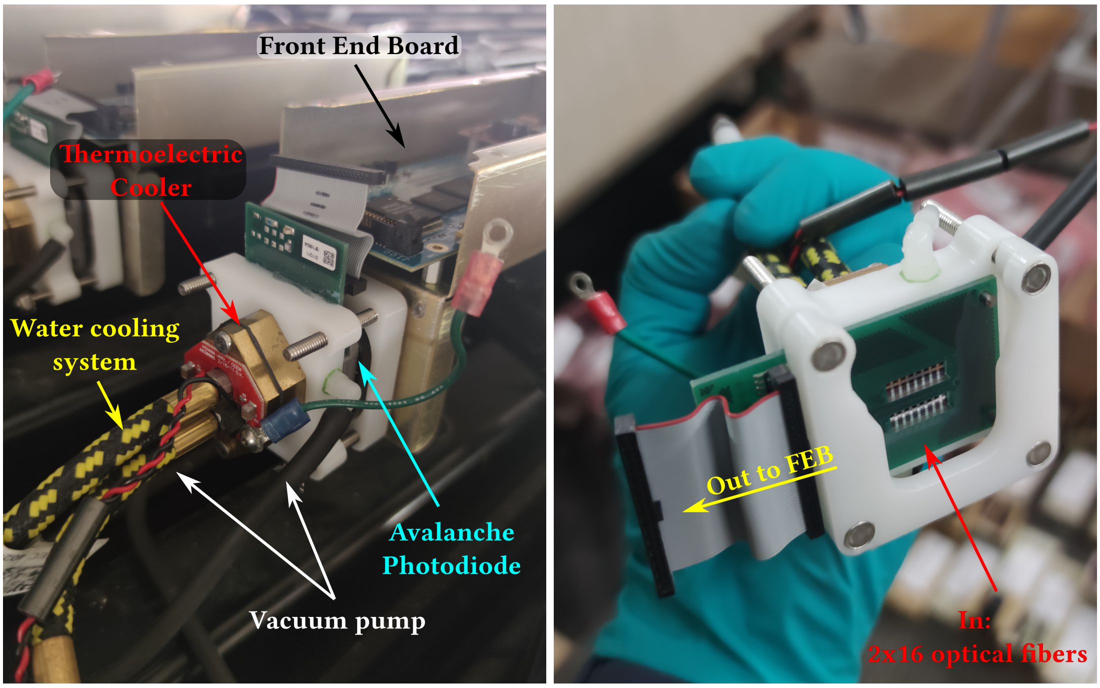

Figure 1.5: The modules with APDs for NOvA mounted on top of the detector on the left picture, and shown from the bottom on the right. The individual components of the module are described. The left picture shows a disconnected ribbon cable and ground cable, which are normally connected to the front end board.

Each APD is connected to a single Front End Board (FEB), shown in Fig. 1.6. The

FEB amplifies and integrates the APD signal, determines its amplitude and arrival time, before passing it to the Data Acquisition (DAQ) system. On the FEB the APD signal is first passed to a custom NOvA Application-Specific Integrated Circuit (ASIC), which is designed to maximize the detector sensitivity to small signals. ASICs amplify, shape and combine the signal, before sending it to an Analog-to-Digital Converter (ADC). The combined noise from the APD and the amplifier is equivalent to about 4 PEs, which, compared to an average PE yield from the far end of the FD cell of 30, results in a good signal and noise separation [24]. The digitized data from an ADC is sent to a Field Programmable Gate Array (FPGA), which extracts the time and amplitude of the ADC signals, while subtracting noise based on a settable threshold. The FPGAs employ multiple correlated sampling methods to reduce noise and improve time resolution of the signal [30].

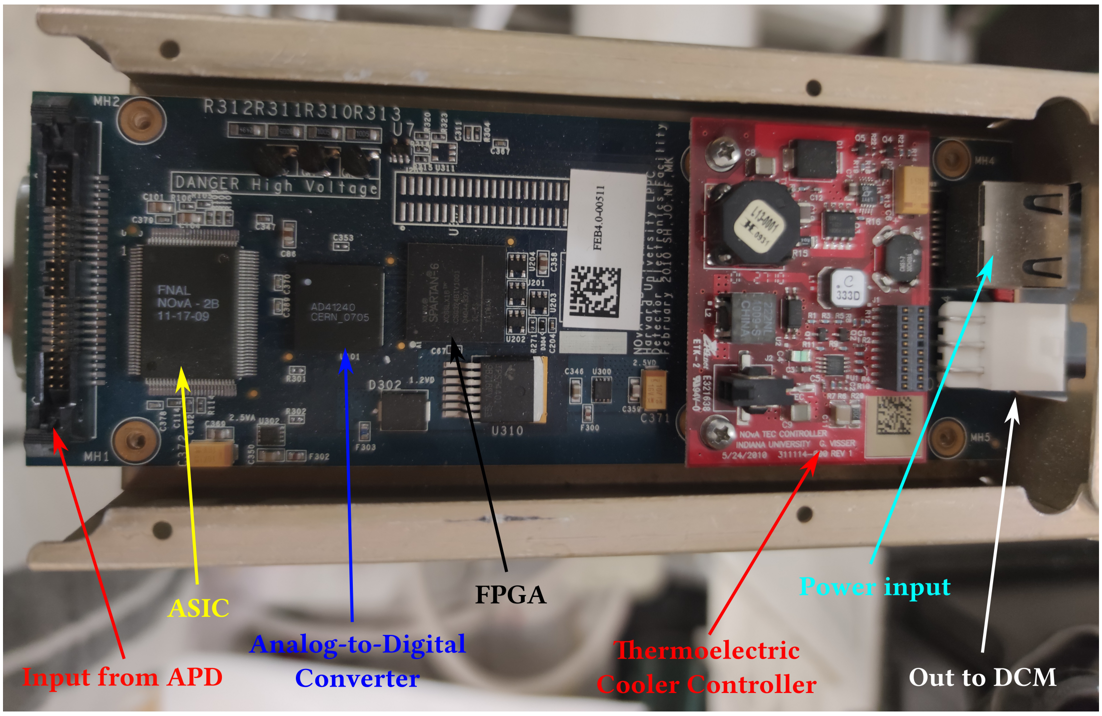

Figure 1.6: An example of a NOvA FEB with individual components labelled.

All of the NOvA front end electronics (APDs and FEBs) are operated in a continuous readout mode, without requiring any external triggers [24]. Due to higher detector activity during beam spills, the ND FEBs work at a higher frequency of 8 MHz, whereas the FD FEBs suffice with 2 MHz sampling frequency [30].

Data from up to 64 FEBs are concentrated in a Data Concentration Module (DCM), which concatenates and packages the data into 5 ms time slices, before sending it to the buffer nodes. DCMs are also connected to the timing system and pass a single unified timing measurement to the FEBs to maintain synchronization across the detector [30].

The buffer nodes cache the data for at least 20 seconds while receiving information from the trigger system. Each trigger uses a time window based either on the time of the NuMI beam spill, on a periodic interval for monitoring and for the readout of cosmic events, or on one of the activity-based data-driven triggers [30]. Data that fall within any of the trigger windows are sent to a data logger system, where they are merged to form events, before being written to files for offline processing and sent to an online monitoring system. Files are organized based on a unique combination of run and subrun numbers, with runs corresponding to data taking periods with constant detector conditions and limited to either 64 subruns or 24 hours. Subruns are delineated either by a 2 GB file size constraint or a 1-hour timeout limit [31].

The detectors are continuously monitored to ensure data stability and quality. Subruns with suboptimal detector conditions or with events failing basic quality criteria are flagged as 'bad' and recorded in a 'bad runs list' [31]. Additionally, individual readout channel are assessed on a per-subrun basis, with those with too high or too low hit rates marked as 'bad' [32]. Both the 'good runs' list and the 'bad channel' maps are used to inform event processing and during simulation to emulate real detector conditions.

1.4 Simulation

To extract neutrino oscillation parameters, or to test a hypothesis, NOvA uses a series of simulations to make predictions according to various physical models [33]. The simulation chain can be divided into four parts: simulation of the neutrino beam, simulation of neutrino interactions within the NOvA detectors, simulation of cosmic particles interacting in the NOvA detector and simulation of the detector and readout response.

To simulate the neutrino beam, NOvA uses a simulation based on the GEANT4 v9.2.p03 [34] Monte Carlo (MC) event generator with a detailed model of the NuMI beamline [35], as described in Sec. 1.1. The simulation starts with the $120\,\mathrm{GeV/c}$

MI protons interacting within the long carbon target and producing hadrons, mainly π, K and secondary protons. This is followed by transport and possible further interaction of hadrons within the focusing system, until finally ending with hadron decays producing the neutrino beam.

To account for the inherently imprecise theoretical models used in GEANT4, NOvA uses the Package to Predict the Flux (PPFX) to incorporate external measurements of yields and cross sections of hadron interactions inside the target and the other NuMI materials into the neutrino beam prediction [36]. The current version of PPFX is limited by the results available during its creation and only corrects the most frequent interactions while assigning conservative systematic uncertainties to the rest (see Sec. 1.8). For the most common π, K and p production, PPFX uses the NA49 measurements [37–39] of $158\,\mathrm{GeV/c}$ protons interacting on a thin (few percent of interaction length) carbon target. To expand the kinematic coverage, PPFX uses a few data points from Barton et al [40] for the π production and K/π ratios from the Main Injector Particle Production (MIPP) [41] experiment for the production of K. These results have to be scaled to the $20 - 120\,\mathrm{GeV/c}$ incident proton moment seen throughout NuMI using the FLUKA [42, 43] MC generator.

There are two new experiments that measure the production and interaction of hadrons on various targets and incident energies, specifically designed to improve the prediction of neutrino beams. The most impactful measurements from the NA61 experiment are of the $120\,\mathrm{GeV/c}$ protons on a thin carbon target [44–46], of the hadron incident interactions on various materials [47], and of the $120\,\mathrm{GeV/c}$ protons on a NuMI replica target [48]. Additionally, the Fermilab-based EMPHATIC experiment [49] is currently analysing a broad range of hadron production and secondary and tertiary interaction measurements for neutrino beam prediction with a significant involvement of NOvA and DUNE collaborators. Inclusion of the results from both of these measurement is currently under way and will significantly improve the neutrino beam prediction in NOvA [48].

The output of the neutrino beam simulation is passed to the simulation of neutrino interactions inside the detectors, which is done with the GENIE v3.0.6 [50] neutrino MC generator. GENIE allows users to choose the particular models for different types of neutrino interactions and particle propagation within the nucleus, as well as possible tunes to external measurements. The four main interaction modes in GENIE are the Quasi-Elastic (QE) Charged Current (CC) scattering, the Resonant baryon production (Res), the Deep Inelastic Scattering (DIS), and the Coherent π (COHπ) production. The special case of the two particle - two hole (2p2h) interaction via Meson Exchange Current (MEC) and the Final State Interaction (FSI) inside a nucleus are also considered. The initial state of the nucleus is represented by a local Fermi gas in the QE and 2p2h models, while a global relativistic Fermi gas is used for all other processes. All of these are set by the Comprehensive Model Configuration (CMC), which is currently `N1810j0000` for NOvA. Additionally, NOvA adds a costume tune to the NOvA ν_μCC data for a better constraint of the CCMEC interactions. NOvA also uses a set of external π interaction measurements to constrain the FSI model. Table 1.1 shows the list of models and tunes for different interaction modes in NOvA [7].

Table 1.1: Models and tunes used in the NOvA simulation of neutrino interactions.

Interaction	Model	Tune
CCQE	València [51]	External $\nu - \mathrm{D}$ data [52]
CCMEC	València [53, 54]	NOvA ν_μCC data
Res & COHπ	Berger-Sehgal [55, 56]	External $\nu - A$ data
DIS	Bodek-Yang [57, 58]	External $\nu - A$ data
FSI	Semi-classical cascade [59]	External $\pi -^{12}$ C data

Since the FD is on the surface NOvA also uses a simulation of cosmic rays generated with the MC Cosmic-Ray Shower Generator (CRY) [60]. The simulated cosmic muons are also used to calibrate NOvA detectors [36].

Particles that are created from neutrino interactions and cosmic rays are propagated through the NOvA detectors using the GEANT4 v10.4.p02 [34], which outputs the energy deposited in the scintillator. This is then passed to a custom NOvA software of the light model [36], which calculates the amount of scintillation light produced for the deposited energy based on a Poisson distribution. The scintillation light production is parametrized using the Birks-Chou model [61], which corrects for the recombination in organic scintillators at high deposited energies. The scintillator light yield and the inherent production of the Cherenkov light, which can affect the light readout, are tuned to NOvA data [9]. The light collection by the WLS fibres, its transport to the APDs, and the APD response use a parametrized simulation, as the NOvA cells and their readout are generally the same across the detectors [36]. The simulation of the readout electronics is done by another custom NOvA parametrized model, which accounts for random noise in the readout electronics and outputs true events in the same format as the real data.

Due to the high neutrino rate in the ND, there are neutrinos interacting in the surrounding rock creating particles, mainly muons, that make it to the detector and act as background. However, since only a few 'rock muons' make it into the detector, it would be very time consuming to run a simulation which includes the rock around the ND for every neutrino. Instead, NOvA creates a separate simulation that includes the surrounding rock and then overlays these results into the nominal NOvA simulation chain to match the NuMI neutrino rate [36].

1.5 Data Processing and Event Reconstruction

Both data and simulation events for all NOvA detectors are passed through the same event reconstruction and particle identification algorithms. The reconstruction was specifically developed with the ν_e appearance search in mind, focusing on identifying the ν_eCC signal against the ν_μCC and Neutral Current (NC) backgrounds. Each NOvA detector has to deal with different challenges, with multiple neutrinos interacting during one beam spill in the ND, and a large cosmic background in the FD [62].

The output from the DAQ system for each channel is called a *raw hit*. Hits are grouped into $550\,\mu\text{s}$-long windows and passed to an offline reconstruction chain [62]. Reconstruction starts by grouping hits into *slices* based on their proximity to other hits in both time and space [63]. Slices are designed to ideally contain only a single neutrino interaction event.

For events that produce hadronic and electromagnetic showers, reconstruction first identifies straight lines through major features using a modified Hough transform [64], representing particle directions. These lines are passed to the Elastic Arms algorithm [65] to identify *vertex* candidates from their intersection points. Hits are then clustered into *prongs*, which are collections of hits with a start point, based on the vertex, and a direction, using a k-means algorithm called FuzzyK [66, 67]. Here 'fuzzy' means that each hit can belong to multiple prongs. Prongs are first created separately for each view (also called 2D prongs) and then, if possible, view-matched into 3D prongs (from here on referred to as prongs) [62]. Figure 1.7 shows an example of a simulated electron shower, where the reconstructed vertex is shown as a red cross and the prong as a red shaded area. The prong groups together all the hits that are part of the shower, while removing the background hits, shown in grey.

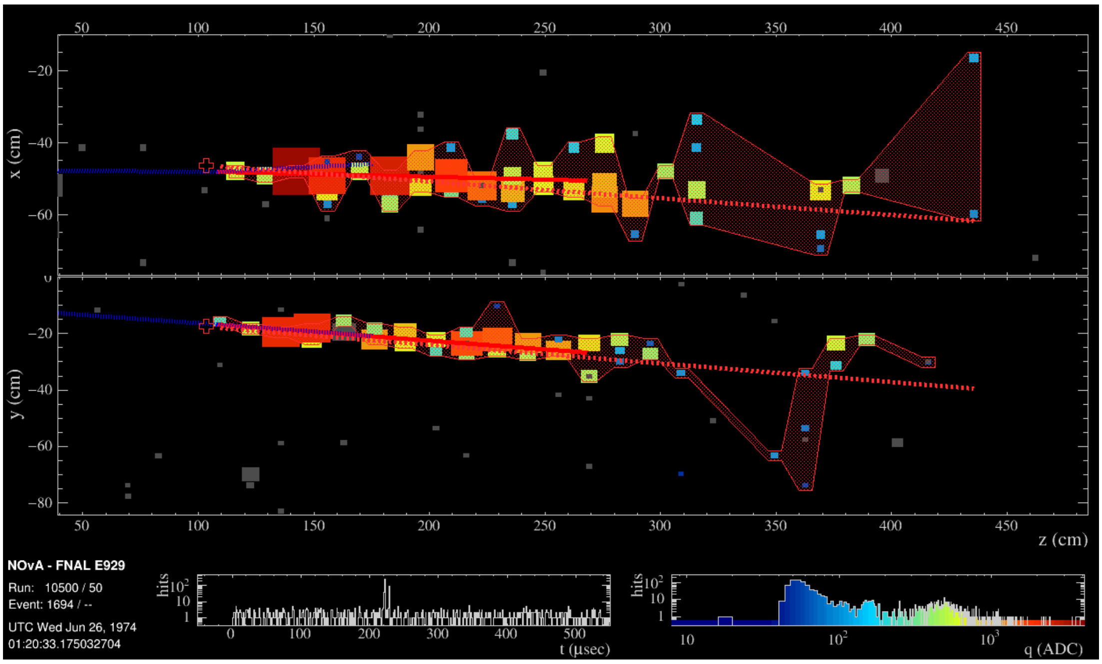

Figure 1.7: Reconstruction of a simulated single electron event in the NOvA ND. The red cross is the reconstructed vertex, the shaded area shows the cluster of hits into a prong and the dotted red line shows the estimated shower direction. The blue dotted line shows the true direct of the scattering neutrino and the solid red line the true momentum of the scattered electron. Figure from internal NOvA database [68].

For particles that are represented by tracks rather than showers (especially muons), the reconstruction takes the slice hits and forms 'Kalman tracks' based on a Kalman filter [69]. In addition to the start point and the direction, which exist also for prongs, tracks also contain information on the vector of trajectory points that make up the track and on the end point - and therefore on the track length. A parallel tracking algorithm takes in the Elastic Arms vertex and the Fuzzy-K prongs and forms Break Point Fitter (BPF) tracks [70, 71], using a model of Coulomb scattering and energy loss. BPF tracks also contain an information on the particle 4-momenta based on various particle assumptions, most notably the muon assumption. For cosmic particles, mostly muons, NOvA uses another track reconstruction algorithm, called 'window cosmic track' [72]. It uses a sliding 5 plane-long window, in which it fits a straight line to the recorded hits. The window starts from the end of the detector and then slides forward and repeats the fitting process until all hits are processed. This way it accounts for possible Coulomb scattering of cosmic muons. The intersection of each cosmic track with the edge of the detector (or extrapolation of the track to the edge of the detector) is reconstructed as the 'cosmic ray vertex'.

To identify individual particles and remove backgrounds, NOvA uses several Machine Learning (ML) algorithms, outputs of which are used in combination with the information from classical reconstruction algorithms for Particle Identification (PID). The most common topologies for particles interacting in NOvA detectors are shown in Fig. 1.8. Muons are easily identifiable as single long tracks which decay into an electron (or positron) if stopping inside of the detector. Both electrons and π^0's produce electromagnetic showers, but thanks to the low-Z composition and high granularity of the detector, there is a gap between the interaction vertex and the electromagnetic shower for the π^0.

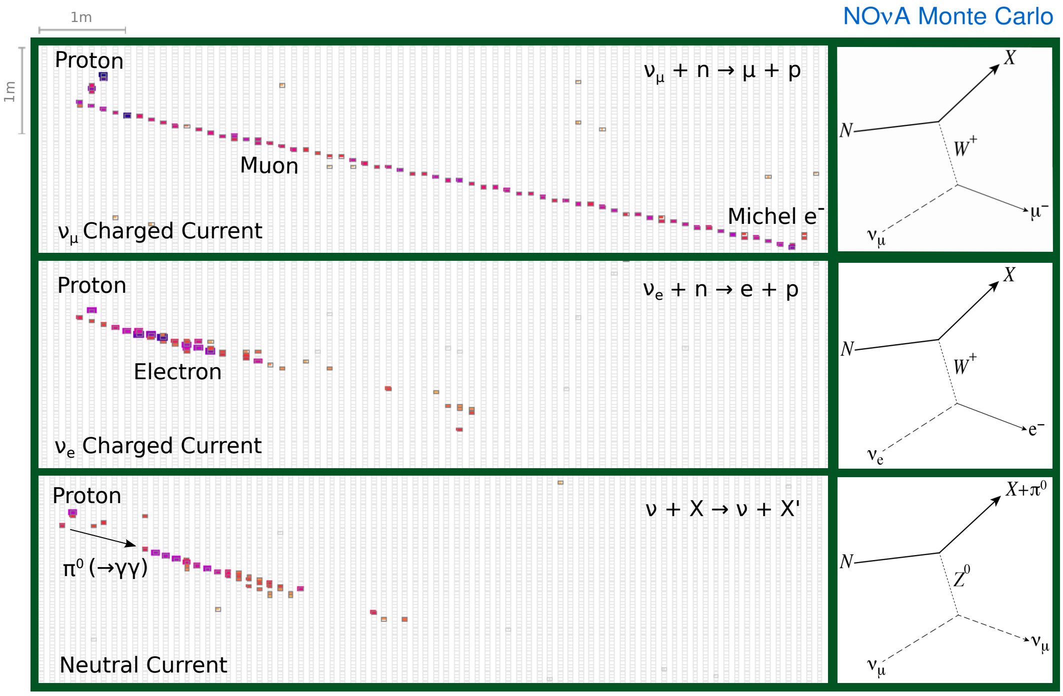

Figure 1.8: Different event topologies as seen in the NOvA detectors with corresponding Feynman diagrams [62]. Each event is a simulated 2.15 GeV neutrino interacting in a NOvA detector producing a 0.78 GeV proton and a second 1.86 GeV particle depending on the interactions type. The figure shows only one view and the colouring represents the deposited energy.

One of the ML algorithms that NOvA employs is a Convolutional Neural Network (CNN) based on the GoogLeNet [73] architecture named Convolutional Visual Network (CVN) [74]. When it is applied to identify entire events it is called *EventCVN* and uses slice hits to classify interactions into one of the five categories: ν_e, ν_μ, ν_τ, NC, or cosmic. The same architecture, but applied to the Fuzzy-K prongs, is called *ProngCVN* [75], and is used to identify what particles the prongs most likely correspond to. This assignment is useful in calculation of prong energy, as described in Sec. 1.7. Another ML algorithm is specifically designed for identifying muons and is based on a Boosted Decision Tree (BDT). It is called Reconstructed Muon Identifier (ReMId) [69] and uses the reconstructed Kalman tracks as inputs.

1.6 Detector Calibration

The energy deposited within NOvA detectors is represented by the peak ADC values for each cell the particle passed through, obtained from the readout electronics, as described in Sec. 1.3. The conversion of the peak ADC values into physical units of energy requires calibrating the NOvA detectors [76], while accounting for the attenuation of light along the WLS fibres, or for differences between individual cells. The purpose of calibration is to calculate a conversion factor from $\mathrm{ADC} \rightarrow \mathrm{MeV}$ for every part of the detector, so that the same energy deposited anywhere and at any time, is recorded as the same value of the reconstructed energy.

NOvA uses cosmic ray muons for calibration due to their abundance in the NOvA detectors and their consistent energy deposition. To calculate the absolute energy scale, NOvA selects a subsample of muons stopping inside of the detectors when they are almost exactly Minimum Ionising Particle (MIP) and therefore have a well understood energy deposition. The cosmic muons are collected using a periodic trigger with the same length as the beam trigger, whilst removing events with timestamps overlapping with the beam spill window. The simulation of cosmic muons is created using the CRY [60] MC generator, as outlined in Sec. 1.4.

Cosmic muon tracks are reconstructed using the window cosmic track algorithm described in Sec. 1.5. The selection of well reconstructed cosmic tracks requires that at least 80% of all hits from the reconstructed slice contribute to the track [29]. Each track must have at least 2 hits in both the x and y views and the difference in the number of planes the track crossed between the views must be at most 10% of the total number of planes. Also, the plane where each track starts or stops in one view must be within 3 planes of the start or stop plane in the other view. Additionally, since tracks that do not cross many planes tend to not be reconstructed very well, the extent of each track in the z direction must be at least $70\,\mathrm{cm}$ and tracks must have at least 20% of their total track direction in the z axis. Tracks with on average more than 6 cells per plane and with path lengths through the cell larger than $10\,\mathrm{cm}$ are removed for the same reason. Furthermore, all the reconstructed tracks must start at most $10\,\mathrm{cm}$ from the edge inside of the detector and stop at most $10\,\mathrm{cm}$ outside of the detector. Lastly, tracks with trajectory points far away from each other are also removed. The selection of stopping muons for the absolute energy scale relies on identifying Michel electrons, which are produced by decaying muons at the end of their tracks, as can be seen on the top panel of Fig. 1.8.

Since the energy deposited in a cell is proportional to the distance the particle travels through the cell, the input variable for calibration is the deposited energy divided by the path length through the cell PE/cm. To ensure the path length is well calculated, all hits used in calibration must satisfy the so-called 'tricell' condition, shown in Fig. 1.9. This means that for each calibration hit, there must be a corresponding hit in both of the surrounding cells in the same plane for the same track. The path length can then be calculated simply from the height of the cell and the angle of the reconstructed track. In case there is a bad channel in a neighbouring cell (right side of Fig. 1.9), this channel is ignored and the tricell condition looks one cell further [76]. If the tricell condition fails, the hit can still pass the 'z tricell' condition, which is a longitudinal equivalent of the tricell condition and requires a hit in both the neighbouring planes in the same view and with the same cell number. The 'z tricell' hits are saved separately and may be used if there are no hits satisfying the original tricell condition. This is especially useful for the cells on the edge of the detector, which fail the tricell condition due to only having one neighbouring cell.

The calibration conversion factor from the signal recorded by the detector readout to the deposited energy can be expressed by as

$$E_{dep}\ [\mathrm{MeV}] = \mathsf{Signal}\ [\mathrm{ADC}] \times S_d \times TS_{d,i}^{\textsc{Calib}} \times R_{d,i}\,(t) \times A_d\,(t)\,. \qquad (1.1)$$

The calibration scale therefore consists of four separate and complementary factors:

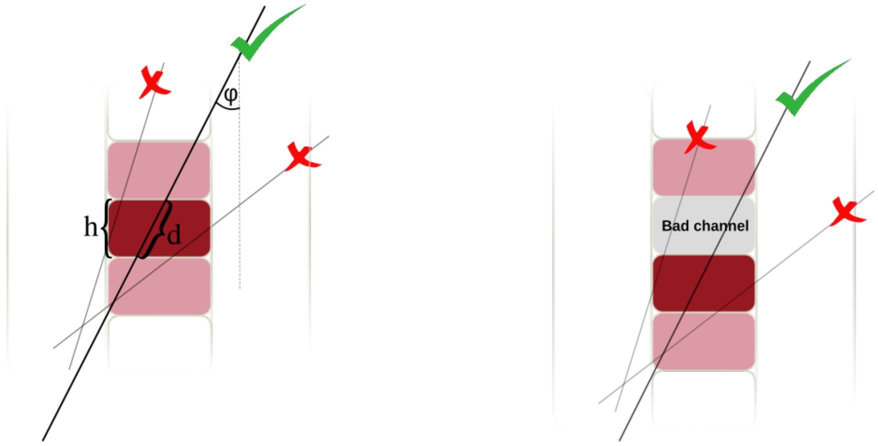

Figure 1.9: Illustration of the tricell condition. Only the hits with two surrounding hits in the same plane are used in the NOvA calibration, as shown on the left plot. This is to ensure a good quality of the path length (d) reconstruction, which is calculated from the known cell height (h) and the reconstructed track angle (φ). In case the hit is next to a bad channel, as shown on the right plot, the bad channel is ignored and the tricell condition requires a hit in the next cell over.

the Scale (S_d), the Threshold and Shielding correction ($TS_{d,i}$), the Relative calibration ($R_{d,i}(t)$) and the Absolute calibration ($A_d(t)$), all described below. Each part is calculated for each detector separately, as indicated by the subscript d. The threshold and shielding correction is only used during calibration and is omitted when applying the calibration results. The relative and absolute calibrations are calculated for each time period separately to account for possible changes in the energy deposition throughout the time, possibly caused by the ageing of the scintillator oil, or of the readout electronics. The time periods are either determined by a fixed time interval, or by running conditions separated by significant changes to the readout or the DAQ systems, including the summer shutdown.

The threshold and shielding correction and the relative calibration calculate a calibration factor for each position within the detector to account for variations caused by the attenuation of light as it travels through the WLS fibres, or by differences between individual cells. This is expressed with a subscript i in Eq. 1.1. For data, the position of a hit in the detector is described by the plane number, cell number and the position within the cell (w). w is calculated as the projection of the cosmic track to the central cell axis and its value is equivalent to the x axis (y axis) coordinate of the projection for the horizontal (vertical) cells, with the 0 value at the centre of the cell [76].

For simulation, the calibration does not use the plane number to determine the position within a detector, as by construction all detector planes should have the same readout. This significantly reduces the requirements for the number of events that need to be simulated, reconstructed, and calibrated, especially for the FD with 896 planes. However, in reality there are some variations in the detector response between individual planes, caused by different *brightness* qualities of the fibres, zipped or twisted fibres, different qualities of the scintillator, possible air bubbles, and potentially other factors. To include these differences in simulation without having to simulate every cell individually, all the cells are divided into 12 equally populated Fibre Brightness (FB) bins based on the uncorrected average response in the center of that cell, as shown in Fig. 1.10. These FB bins describe the relative differences in the detector response between individual cells [77].

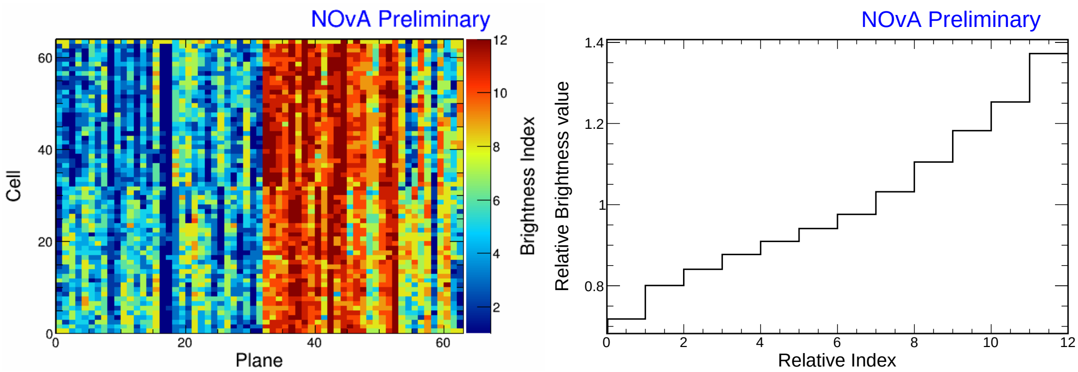

Figure 1.10: Distribution of the NOvA detector cells into 12 brightness bins (left plot), each representing a relative difference in energy response (right plot) due to different brightnesses of the fibres, scintillators, or readout. This is an example from the NOvA Test Beam detector, described in Sec. ??, where the left side of the detector (planes 1-32) has clearly lower response relative to the right side of the detector (planes 33-64).

1.6.1 Scale

The scale calibration factor from Eq. 1.1 is a simple conversion from the peak ADC value into the number of PEs. This factor only depends on the APD gain (which was different in the beginning of NOvA data taking) and on the FEB type (different between detectors, as described in Sec. 1.3).

1.6.2 Threshold and Shielding Correction

The threshold and shielding correction accounts for two assumptions, which hold true in most cases in NOvA, but fall short for some hits at the bottom of the detector, or far away from the readout, especially for the FD [76].

The first assumption is that the ADC response to the photon signal is linear, which is mostly true except close to the APD threshold. Energy deposited far away from the readout may produce photons that get attenuated enough to be shifted below the threshold. However, due to natural fluctuations of the number of photons created by the energy deposition, the same deposited energy may also produce photons that would make it over the threshold, therefore making it appear that the actual deposited energy was higher then in reality, introducing a bias to the calibration. The threshold correction is calculated using simulation, as the ratio between the mean of the Poisson distribution of the true number of the created PE ($\mathrm{PE}_{Poisson\lambda}$) and the number of the 'reconstructed' PE seen by the APD (PE_{Reco}).

The second assumption is that the spectrum of cosmic muons is uniform within each detector. Again, this is generally true, but breaks down in the FD, which is big enough for the top of the detector to shield the bottom of the detector and therefore affect the energy distribution. The shielding correction is calculated from simulation as a ratio between the expected deposited energy if the particle was a MIP (E_{MIP}), which is estimated from simulation for the NOvA scintillator as $E_{\mathrm{MIP}} = 1.78\,\mathrm{MeV/cm}$ and the true deposited energy (E_{true}).

The total threshold and shielding correction is calculated for simulated events in each cell, FB bin and w as

$$TS_i = \frac{\mathrm{PE}_{Poisson\lambda}}{\mathrm{PE}_{Reco}} \frac{E_{\mathrm{MIP}}}{E_{True}}. \tag{1.2}$$

To ensure that the correction changes smoothly across each cell position, the final correction is calculated as a fit to the mean correction value along w in each cell and FB bin.

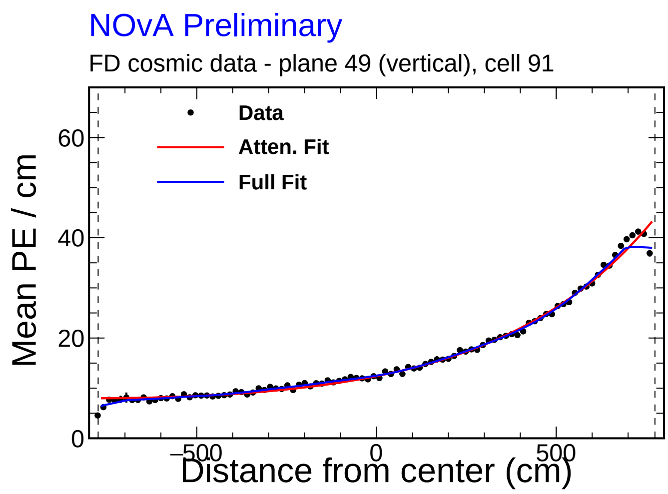

Figure 1.11: Example attenuation fit for a single cell in the NOvA FD across its full length, as shown by dashed vertical lines. The red line shows the initial exponential fit and the blue line shows the full fit after the LOWESS correction, both described in text. Figure from [78].

1.6.3 Relative Calibration

The main goal of the relative calibration is to correct for the attenuation of the scintillator light as it travels through the WLS fibre to the readout. The attenuation in each cell is estimated by performing an 'attenuation fit' to the mean response in PE/cm, as shown in Fig. 1.11. The relative calibration scale is then calculated as the ratio between the average response in PE/cm across the entire detector (can differ between detectors) and the result of the attenuation fit in each particular position within the detector. The response after applying the relative calibration scale is expressed as Corrected Photo Electronss (PECorrs). Since the relative calibration scale is calculated for each cell independently, it effectively corrects for the relative differences between detector cells as well as for the attenuation. Therefore, the resulting distribution of PECorr/cm should be uniform across the detector, especially along the plane, cell and w [76].

The first step to do the attenuation fit is to create 'attenuation profiles' for each cell. Attenuation profiles are profile histograms of mean detector response over the path length through the cell, in the units of PE/cm, along the position within the cell. An example attenuation profile is shown in Fig. 1.11 as black dots. The threshold and shielding correction described in Sec. 1.6.2 is applied to the attenuation profiles before doing the attenuation fit, which consists of two steps.

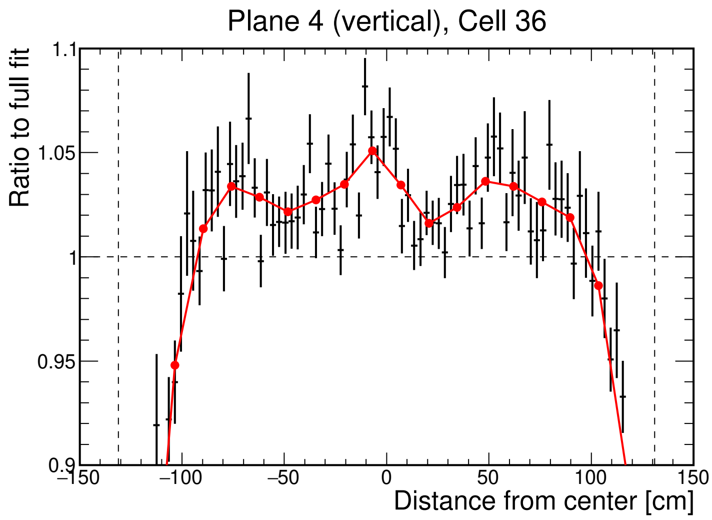

Figure 1.12: Example LOWESS correction for the residual differences after the exponential part of the attenuation fit of the NOvA relative calibration. This is an example for a single cell in the NOvA Test Beam detector with black points showing the residual differences and red line the LOWESS correction, both described in text.

1. The first step is a three-parameter exponential fit according to

$$y = C + A\left(\exp\left(\frac{w}{X}\right) + \exp\left(-\frac{L+w}{X}\right)\right), \tag{1.3}$$

   where y is the fitted response, L is the length of the cell and C, A and X are the fitted parameters representing the background, attenuation scale and attenuation length respectively. An example of the exponential fit is shown as a red curve in Fig. 1.11.

2. The second step is the smoothing out of residual differences between the exponential fit and the original distribution with the Locally Weighted Scatter plot Smoothing (LOWESS) method, shown in Fig. 1.12. The residual differences get evened out by creating a smooth distribution of 20 locally weighted points across the length of each cell. The result of the LOWESS correction is then combined with the exponential fit into the full attenuation fit, shown as a blue line in Fig. 1.11.

Even after applying the LOWESS correction, there are sometimes large differences between the attenuation fit and the fitted response. This is usually caused by a small number of events in that cell, common for cells at the edge of the detector. To ensure a good quality of the attenuation fit, the total χ^2 between the attenuation fit and

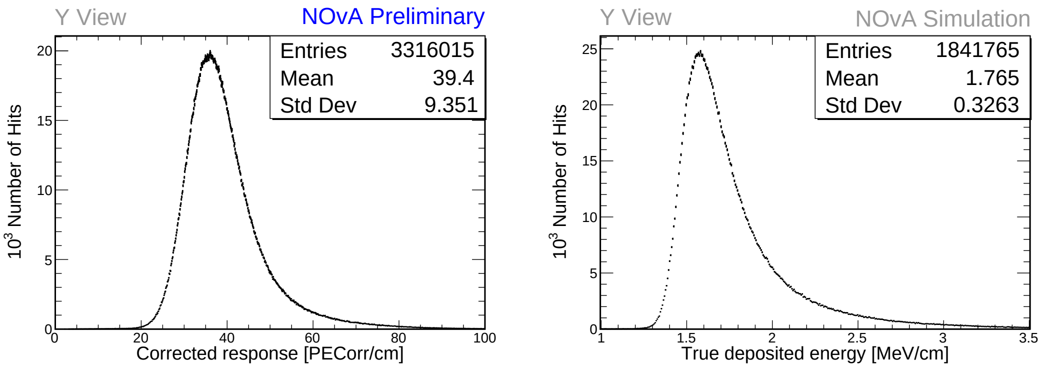

Figure 1.13: The absolute energy scale is calculated as the ratio between the simulated mean true deposited energy (right) and the mean reconstructed energy response (left) for selected stopping muons in each view and each data period or simulation.

the fitted response is calculated and only cells with the final $\chi^2 \leq 0.2$ are counted as *calibrated*. Cells with $\chi^2 > 0.2$ are ignored in further processing and marked as *uncalibrated*.

1.6.4 Absolute Calibration

The absolute calibration only uses hits from muons stopping inside of the detector, in a track window $1 - 2\,\mathrm{m}$ from the end of their tracks. This is when they are approximately MIP and their energy deposition is well understood. Additionally, hits at the edges of each cell are removed to mitigate the effects at the end of the WLS fibres and the lower number of events at the edge of the detector [29].

First, the relative calibration results are applied to the selected stopping muon hits to get a distribution of the corrected detector response in $PECorr/\mathrm{cm}$, as shown on the left of Fig. 1.13. The mean of this distribution is called the *reconstructed* Muon Energy Unit (MEU) and is calculated separately in each of the two views, and in each time period or version of simulation. Analogously, the mean of the true deposited energy in MeV/cm from simulation, shown on the right of Fig. 1.13, is called the *true* MEU. The absolute energy scale (the absolute calibration scale) is then the ratio between the true and the reconstructed MEU value, where both the MEU values are taken as a simple average over the two views

$$\text{Absolute Energy Scale} = \frac{\mathrm{MEU}_{True}\ [\mathrm{MeV}/\mathrm{cm}]}{\mathrm{MEU}_{Reco}\ [\mathrm{PE\textsc{Corr}}/\mathrm{cm}]}. \tag{1.4}$$

The values of the absolute energy scales for each data period and simulation, as well as the results of the attenuation fit, are saved in a set of lookup tables, which are then used any time a hit is recorded in the NOvA detector and processed and reconstructed with the NOvA algorithms described above.

1.7 Energy Estimation

The deposited energy from detector calibration (Sec. 1.6) is only the first step in estimating the neutrino energy (E_ν) required for the main NOvA analyses.

For the ν_μ disappearance analysis, the ν_μ energy is measured as the sum of the muon energy and the energy of the hadronic shower [7]. The muon energy is identified from the length of its track, without the need of the calibration results. The energy of the hadronic shower is estimated from simulation as a fit to the 2D distribution of the true ν_μ energy minus the reconstructed muon energy, versus the visible (not corrected for the dead material) deposited energy of the hadronic system [75].

For the ν_e appearance analysis, the ν_e energy is calculated using a quartic fit to the 2D distribution of the electromagnetic versus the hadronic calorimetric energies, both corrected for the energy deposition in the dead material (PVC cells) [75]. The dead material correction is currently just a simple scaling of the deposited energy from calibration for all particles and is calculated from the measurement of the π^0 mass peak in the NOvA ND. This correction is correct only for electromagnetic showers and is not directly applicable to hadronic showers. The fit to determine the ν_e energy keeps the normalization of both the electromagnetic and the hadronic energies free, so the exact value of the dead material correction is not important. It is however used in other, non-neutrino oscillation analyses.

1.8 Systematic Uncertainties

There are several known unknowns that can affect the results of NOvA measurements, represented by systematic shifts of the predictions. The impact of these uncertainties is assessed by varying the prediction independently for each systematic shift and passing all predictions through the same analysis procedures as the nominal (non-shifted) sample. The nominal and systematically shifted predictions are then compared to determine the systematic uncertainty on the measured parameters. This approach inherently accounts for the effects of systematic uncertainties on background composition, event selection, reconstruction, and other aspects of the analysis.

The primary sources of systematic uncertainties in NOvA include the simulations of neutrino flux, neutrino interaction, and detector modelling, as explained in Sec. 1.4, as well as the detector calibration procedure. Other sources of systematic uncertainties are relevant only to specific analyses and are not discussed here. In NOvA, the 3-flavour [7] and the sterile [13] neutrino oscillation analyses use the ND data to constrain the FD prediction by fitting the ND prediction to data, significantly reducing the effect of the neutrino beam and neutrino interaction systematic uncertainties. On the other hand, these are the leading sources of systematic uncertainties for the ND-only analyses, such as the cross section analyses [8–11], or the neutrino magnetic moment analysis. Detector calibration and modelling uncertainties are significant across all NOvA measurements.

The systematic uncertainty on the neutrino beam prediction arises from two sources: hadron production and beam focusing [36]. Hadron production uncertainties are estimated using the multi-universe technique within the PPFX (see Sec. 1.4), which involves creating 100 alternative universes where inputs from external measurements of hadron production cross-sections are varied within their respective uncertainties. Beam focusing uncertainties are contained in 20 parameters accounting for uncertainties in horn and target positions, horn current, beam position on the target, beam spot size, and the effect of Earth's magnetic field in the beam pipe. Since all these uncertainties can be correlated, particularly in an off-axis detector such as NOvA, a Principal Component Analysis (PCA) is performed to estimate the bin-to-bin covariances in true energy for each neutrino flavour, detector and beam mode [79]. PCA reduces the number of required neutrino flux systematic uncertainty parameters from 20×100 to only 8 *"principal components"* (each with positive and negative shifts) for the ND analyses, or 5 for the ND+FD analyses. Additionally, the principal components are uncorrelated by construction and ordered by their effect on the neutrino beam prediction.

Neutrino interaction-related uncertainties involve 77 adjustable parameters, most of which are provided directly by GENIE [50] to account for theoretical uncertainties in the prediction. These include knobs to adjust the axial and vector masses for the

QE and Res interactions, π angular distribution in the Res π production, parameters of the Bodek-Yang DIS model, or branching ratios for the radiative and single η resonance decays. Additionally, NOvA has developed its own set of systematic uncertainties [80], either based on its own measurements, or on discrepancies observed in other experiments. For example, the NOvA MEC tune has associated uncertainties based on the dependence of the tune on the transferred four momentum or on the neutrino energy.Furthermore, a discrepancy between Res data at low transfer energies and their prediction in the NOvA ND motivated a conservative $100\,\%$ one-sided systematic uncertainty, allowing for a complete suppression of Res events with low energy transfers.

NOvA adapted a theory-based systematic uncertainty for the long-range dependence of CCQE interactions [81, 82]. Data-simulation discrepancies in external experiments motivated additional systematic uncertainties for DIS interactions at high neutrino energies [83], for the distance that a parton travels before hadronization in DIS interactions [84], for COHπ production [85], or for the FSI model [86]. Lastly NOvA applies a $2\,\%$ systematic uncertainty on the ratio of ν_eCC and ν_μCC cross sections to account for their potential differences due to radiative corrections or second class currents [87].

Systematic uncertainties in the simulation of the detector response arise mainly from the light model tuning described in Sec. 1.4. This includes the uncertainty on the overall normalization on the amount of light produced by deposited energy and a special uncertainty for the amount of Cherenkov light. The Cherenkov light uncertainty is calculated by profiling over various Cherenkov scaling factors during the light model tune and using the 3σ confidence interval around the best fit value as the Cherenkov systematic uncertainty, resulting in a $\pm 6.2\,\%$ uncertainty. Similarly, the light level uncertainty is determined by profiling over the overall light level scaling factor, resulting in a $\pm 5\,\%$ uncertainty.

There are three systematic uncertainties arising from the calibration procedure: the absolute energy scale, the calibration shape (representing) and detector ageing. Measurements of some "standard candles" mainly in the ND are used to set the systematic uncertainty on the absolute energy scale, calculated as the data-simulation difference. The standard candles include beam muons, beam protons, rock muons,

π^0 mass peak measurement and Michel electrons. Results of all these measurements combined lead to a $5\,\%$ systematic uncertainty on the absolute energy scale [88]. The calibration shape uncertainty accounts for the residual variations in the relative energy deposition along the cell, especially on cell edges. The shape and size of the calibration shape systematic uncertainty is determined by a fit to a data-simulation ratio, resulting in a steep rise at cell edges, where the uncertainty is up to $30\,\%$, while being fixed to $0\,\%$ in the cell centre [89]. Lastly, the detector ageing uncertainty is implemented as a time-dependent decrease of light level by $4.5\,\%$ a year, with a corresponding increase in the overall calibration scale to compensate [90].

Chapter 2

Measuring the Muon Neutrino Magnetic Moment

In this analysis, I aim to detect a potential signal of the effective muon neutrino magnetic moment in the NOvA ND. This signal would manifest as an excess of neutrino-on-electron (ν-on-e) elastic scattering interactions at low electron recoil energies, proportional to the value of the effective neutrino magnetic moment, over the Standard Model (SM) background. If no significant excess is observed, I will establish an upper limit on the effective muon neutrino magnetic moment.

Detecting the neutrino magnetic moment (μ_ν) would provide definitive evidence of new Beyond Standard Model (BSM) physics, and measuring its value would help identify the appropriate BSM theory. As current and planned experiments can only detect an anomalously large neutrino magnetic moment, observing such a signature would strongly suggest that neutrinos are Majorana particles and would have significant implications for astrophysics and cosmology [91].

The best model-independent experimental results on the neutrino magnetic moment come from experiments searching for dark matter using xenon-based detectors. These highly sensitive detectors detect solar neutrinos, which are part of the background in dark matter searches but can be reanalyzed for other purposes. In 2020, the XENON1T experiment observed [92] a low energy excess of solar neutrinos, which could correspond to a signal from an anomalously large effective magnetic moment within $\mu_{\nu_\odot} \in (0.14, 0.29) \times 10^{-10} \mu_B$ at $90\,\%$ Confidence Level (C.L.), where $\nu_\odot$ marks solar neutrinos. However, this result was disfavoured by the follow-up XENONnT experiment in 2022 [93], which saw no excess and set the current world-leading limit on neutrino magnetic moment at $\mu_{\nu_\odot} < 0.063 \times 10^{-10} \mu_B$ at $90\,\%$ C.L.. Other solar neutrino experiments also reported null results regarding neutrino magnetic moment [94, 95], placing less stringent limits on its value. Given some basic assumptions [95, 96] this limit for solar neutrinos would correspond to a limit on muon neutrino effective magnetic moment of $\mu_{\nu_\mu} < 0.137 \times 10^{-10}\mu_B$. However, the relationship between effective magnetic moments of different neutrino flavours may be non-trivial, especially in the context of possible new BSM physics, and studying muon neutrinos remains an important endeavour [97].

The best results for ν_μ and $\overline{\nu}_\mu$ come from accelerator-based stopped pion neutrino sources [98, 99], which also do not observe any low energy excess and provide an upper limit on the effective muon neutrino magnetic moment of $\mu_{\nu_\mu} < 6.8 \times 10^{-10}\mu_B$ at $90\,\%$ C.L. [98]. Stopped pion neutrino sources provide well-understood beams made up of ν_μ, $\overline{\nu}_\mu$ and ν_e with energies up to $52.8\,\mathrm{MeV}$. Slightly looser limits come from pion decay-in-flight accelerator-based measurements (similar to NOvA)[100, 101], which provide a limit of $\mu_{\nu_\mu} < 8.5 \times 10^{-10}\mu_B$ at $90\,\%$ C.L..

Thanks to the very intense and highly pure beam of muon neutrinos and antineutrinos, and a detector designed for the reconstruction and identification of events with electrons in the final state, NOvA is well-positioned to provide a highly competitive, and possibly even world-leading, measurement (or limit) of the effective muon neutrino magnetic moment. A previous analysis of NOvA ND data for a measurement of the effective muon neutrino magnetic moment was presented in a thesis [102], providing a (statistics-only) limit of $\mu_{\nu_\mu} < 15.8 \times 10^{-10}\mu_B$ at $90\,\%$ C.L..

Additionally, ν-on-e elastic scattering interactions are used in various other analyses in NOvA, specifically in efforts to constrain the neutrino beam prediction [103, 104] and in the search for Light Dark Matter (LDM) [105]. These analyses developed various tools and methods that can be utilized in the search for a neutrino magnetic moment.

In this chapter, I will provide an overview of the theory of neutrino electromagnetic interactions in Sec. 2.1, focusing on the effective neutrino magnetic moment and its implications for ν-on-e measurements and other theoretical considerations. In Sec. 2.2, I will discuss the analysis strategy, the signal and background definition, as well as the data and simulation samples and the analysis weights. Following this, in Sec. 2.3 I will explain the selection of events for this analysis, while in Sec. 2.4 I will address the relevant systematic uncertainties. I will present the results of this analysis in Sec. 2.5 and discuss their implications in Sec. 2.6. Finally, section 2.7 will summarise the findings of this analysis.

2.1 Theory of the Neutrino Magnetic Moment

As was described in Sec. **??**, neutrinos in the SM are massless and electrically neutral particles. However, even SM neutrinos can have electromagnetic interaction through loop diagrams involving charged leptons and the W boson, covered by the neutrino charge radius [91].

In general BSM theories, considering interactions with a single photon as shown on Fig. 2.1, neutrino electromagnetic interactions can be described by an effective interaction Hamiltonian [106]

$$\mathcal{H}_{em}^{(\nu)}(x) = \sum_{k,j=1}^{N} \overline{\nu}_k(x)\, \Lambda_\mu^{kj} \nu_j(x)\, A^\mu(x)\,. \tag{2.1}$$

Here $\nu_k(x)\,, k = 1, ..., N$, are neutrino fields in the mass basis with N neutrino mass states, Λ_μ^{kj} is a general vertex function and $A^\mu(x)$ is the electromagnetic field.

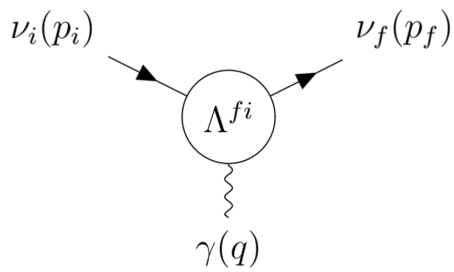

Figure 2.1: Effective coupling of neutrinos with one photon electromagnetic field.

The vertex function $\Lambda_\mu^{fi}(q)$ is generally a matrix and, in the most general case consistent with the SM gauge invariance [107, 108], can be written in terms of linearly independent products of Dirac matrices (γ) and only depends on the four momentum of the photon $(q = p_f - p_i)$:

$$\begin{aligned}\Lambda_\mu^{fi}(q) =& \mathbb{F}_1^{fi}\left(q^2\right) q_\mu + \mathbb{F}_2^{fi}\left(q^2\right) q_\mu \gamma_5 + \mathbb{F}_3^{fi}\left(q^2\right) \gamma_\mu + \mathbb{F}_4^{fi}\left(q^2\right) \gamma_\mu \gamma_5 + \\ & \mathbb{F}_5^{fi}\left(q^2\right) \sigma_{\mu\nu} q^\nu + \mathbb{F}_6^{fi}\left(q^2\right) \epsilon_{\mu\nu\rho\gamma} q^\nu \sigma^{\rho\gamma},\end{aligned} \tag{2.2}$$

where $\mathbb{F}_i^{fi}(q^2)$ are six Lorentz invariant form factors and δ and ϵ are the Dirac delta and the Levi-Civita symbols respectively.

Applying conditions of hermiticity $\left(\mathcal{H}_{em}^{(\nu)\dagger} = \mathcal{H}_{em}^{(\nu)}\right)$ and of the gauge invariance of the electromagnetic field, the vertex function can be rewritten as

$$\Lambda_{\mu}^{fi}\left(q\right)=\left(\gamma_{\mu}-q_{\mu}\not{q}/q^{2}\right)\left[\mathbb{F}_{Q}^{fi}\left(q^{2}\right)+\mathbb{F}_{A}^{fi}\left(q^{2}\right)q^{2}\gamma_{5}\right]-i\sigma_{\mu\nu}q^{\nu}\left[\mathbb{F}_{M}^{fi}\left(q^{2}\right)+i\mathbb{F}_{E}^{fi}\left(q^{2}\right)\gamma_{5}\right], \tag{2.3}$$

where $\mathbb{F}_{Q}^{fi}, \mathbb{F}_{M}^{fi}, \mathbb{F}_{E}^{fi}$ and $\mathbb{F}_{A}^{fi}$ are hermitian matrices representing the charge, dipole magnetic, dipole electric and anapole neutrino form factors respectively. It is clear that the vertex function only depends on the square of the four momentum of the photon q^2. In coupling with a real photon $(q^2 = 0)$ these form factors become the neutrino charge and magnetic, electric and anapole moments respectively. Additionally, the neutrino charge radius corresponds to the second term in the expansion of the charge form factor [106].

The above expression can be simplified [109] as

$$\Lambda_{\mu}^{fi}\left(q\right)=\gamma_{\mu}\left(Q_{\nu_{fi}}+\frac{q^{2}}{6}\langle r^{2}\rangle_{\nu_{fi}}\right)-i\sigma_{\mu\nu}q^{\nu}\mu_{\nu_{fi}}, \tag{2.4}$$

where $Q_{\nu_{fi}}$, $\langle r^2\rangle_{\nu_{fi}}$, and $\mu_{\nu_{fi}}$ are the neutrino charge, effective charge radius (also containing anapole moment), and an effective magnetic moment (also containing electric moment) respectively. This is possible thanks to the similar effects of the neutrino charge radius and the anapole moment, and of the neutrino magnetic and electric moments, on neutrino interactions. Therefore, these are the three neutrino electromagnetic properties (charge, effective charge radius and effective magnetic moment) measured in experiments.

The neutrino electric charge is primarily constrained through measurements of the neutrality of matter and through cosmological observations, which provide much better constraints than neutrino oscillation experiments [106]. On the other hand, the neutrino charge radius would manifest as an increase in the size of the ν-on-e elastic scattering coupling constants, allowing it to be studied in neutrino oscillation experiments such as NOvA. Additionally, the value of the neutrino charge radius in the SM is only an order of magnitude smaller than the current world-leading limits [110] and measuring it could either confirm the validity of neutrino interactions in the SM, or open possibilities to non-standard contributions to neutrino scattering [106]. However, measurement of the neutrino charge radius is not part of this analysis, but may be included in the future re-analysis of the ν-on-e interactions in the NOvA ND.

2.1.1 Neutrino Electric and Magnetic Dipole Moments

The size and effect of neutrino electromagnetic properties depend on the specific BSM theory applied. Evaluating one loop diagrams in the minimally extended SM with three right-handed Dirac neutrinos, as described in Sec. ??, gives the first approximation of the electric and magnetic moments, which are now 3×3 matrices with elements:

$$\left.\begin{matrix} \mu_{kj}^{D} \\ i\epsilon_{kj}^{D} \end{matrix}\right\} \simeq \frac{3eG_F}{16\sqrt{2}\pi^2}\left(m_k \pm m_j\right)\left(\delta_{kj} - \frac{1}{2}\sum_{l=e,\mu,\tau} U_{lk}^{\star} U_{lj}\frac{m_l^2}{m_W^2}\right), \tag{2.5}$$

where m_k, m_j are the neutrino masses and m_l are the masses of charged leptons which appear in the loop diagrams [106]. The D superscript denotes Dirac neutrinos and M denotes Majorana neutrinos throughout this section. Also, e is the electron charge, G_F is the Fermi coupling constant, U is the Pontecorvo-Maki-Nakagawa-Sakata (PMNS) neutrino oscillation matrix, and m_W is the mass of the W boson. Higher order electromagnetic corrections were neglected, but can also have a significant contribution, depending on the theory.

It can be seen that Dirac neutrinos have no diagonal electric moments $\left(\epsilon_{kk}^{D} = 0\right)$ and their diagonal magnetic moments are approximately

$$\mu_{kk}^{D} \simeq \frac{3eG_F m_k}{8\sqrt{2}\pi^2} \simeq 3.2 \times 10^{-19}\left(\frac{m_k}{\text{eV}}\right)\mu_B, \tag{2.6}$$

where μ_B is the Bohr magneton which represents the value of the electron magnetic moment [106]. Neutrino magnetic moments are therefore strongly suppressed by the smallness of neutrino masses, with theoretical predictions in Eq. 2.6 several orders of magnitude below the reach of current experiments [109].

The transition magnetic moments in the minimally extended SM from Eq. 2.5 are suppressed with respect to the largest of the diagonal magnetic moments by at least a factor of 10^{-4} due to the m_W^2 in the denominator. The transition electric moments are even smaller due to the mass difference in Eq. 2.5. Therefore an experimental observation of a magnetic moment larger than in Eq. 2.6 would indicate physics beyond the minimally extended SM [106, 111].

The suppression of the neutrino magnetic moment by the smallness of its mass can be also expressed in a general case [111]. The 'natural' upper limits on the size of the neutrino magnetic moment for any BSM theory that has New Physics (NP) generated at a scale Λ_{NP} can be expressed as [112]

$$\mu_\nu^D\,(\mu_B) \lesssim 3 \times 10^{-15} \frac{m_\nu^D\,(\mathrm{eV})}{\left[\Lambda_{NP}\,(\mathrm{TeV})\right]^2}. \tag{2.7}$$

Therefore for $\Lambda_{NP} \simeq 1\mathrm{TeV}$ and $m_\nu^D \lesssim 1\mathrm{eV}$ the limit becomes $\mu_\nu^D \lesssim 3 \times 10^{-15}\mu_B$, well below the current experimental capabilities. However, these upper bounds only apply if NP is generated well above the electroweak scale $\Lambda_{EW} \sim 100\,\mathrm{GeV}$ [106].

For Majorana neutrinos, the magnetic and electric form factors (and therefore the magnetic and electric moment matrices) are antisymmetric, thus Majorana neutrinos only have transition moments. The simplest extension of the SM that includes Majorana neutrinos requires either the addition of a Higgs triplet, or right-handed neutrinos together with a Higgs singlet [106]. Neglecting the Feynman diagrams which depend on the model of the scalar sector, the magnetic and electric dipole moments are

$$\left.\begin{array}{c}\mu_{kj}^M \\ \epsilon_{kj}^D\end{array}\right\} \simeq \mp \frac{3ieG_F}{16\sqrt{2}\pi^2}\,(m_k \pm m_j) \sum_{l=e,\mu,\tau} \mathrm{Im}/\mathrm{Re}\,[U_{lk}^\star U_{lj}]\,\frac{m_l^2}{m_W^2}, \tag{2.8}$$

where Im is for μ_{kj}^M and Re is for ϵ_{kj}^D. These are difficult to compare to the Dirac case, due to possible presence of Majorana phases in the PMNS matrices, but it is clear that they have the same order of magnitude as Dirac transition dipole moments. However, the neglected model dependent contributions can enhance the transition dipole moments for Majorana neutrinos [106].

The natural upper bound on the Majorana magnetic moment is less strict compared to the Dirac neutrinos, due to the antisymmetric nature of Majorana magnetic moment, which requires additional Yukawa couplings in the BSM theory compared to Dirac neutrinos, which can enhance the maximal possible magnetic moment [111]. The limit for Majorana neutrinos can be expressed as

$$\mu_{\alpha\beta}^M\,(\mu_B) \leq 4 \times 10^{-9} \frac{\left[m_\nu^M\right]_{\alpha\beta}(\mathrm{eV})}{\left[\Lambda_{NP}\,(\mathrm{TeV})\right]^2} \frac{m_\tau^2}{\left|m_\alpha^2 - m_\beta^2\right|}, \quad \alpha, \beta \in \{e, \mu, \tau\}\,. \tag{2.9}$$

Here, the neutrino magnetic moment is expressed in the flavour basis instead of the mass basis, since the charged lepton masses are diagonal here. The two bases are related by

$$\mu_{ij} = \sum_{\alpha\beta} \mu_{\alpha\beta} U^{\star}_{\alpha i} U_{\beta j}. \tag{2.10}$$

and the effect of the neutrino magnetic moment on neutrino interactions does not depend on the choice of the basis[113].

These considerations imply, that if a magnetic moment $\mu \gtrsim 10^{-15}\mu_B$ were measured, neutrinos are almost certainly Majorana particles [111].

Effective neutrino magnetic moment

As mentioned above, the neutrino magnetic moment measured in experiments is the so-called effective neutrino magnetic moment, which is a combination of electric and magnetic dipole moments and depends on the neutrino source and oscillations. In the ultra-relativistic limit, the effective neutrino magnetic moment is

$$\mu^2_{\nu_l}\left(L, E_\nu\right) = \sum_j \left| \sum_k U^{\star}_{lk} e^{\mp i \Delta m^2_{kj} L/2E_\nu} \left(\mu_{jk} - i\epsilon_{jk}\right) \right|^2, \tag{2.11}$$

where the minus sign in the exponent is for neutrinos and the plus sign for antineutrinos [106]. Therefore, the only difference between the effective neutrino and antineutrino magnetic moment is in the phase induced by neutrino oscillations. For experiments with baselines short enough that neutrino oscillations would not have time to develop $(\Delta m^2 L/2E_\nu \ll\sim 1)$, such as the NOvA ND, the effective magnetic moment is the same for neutrinos and antineutrinos and is independent of the neutrino energy.

Since the effective magnetic moment depends on the initial neutrino flavour, it is different for experiments studying neutrinos from different sources. Additionally, experiments such as solar neutrino experiments, need to include matter effects on the neutrino oscillations. Therefore the reports on the value (or upper limit) of the effective neutrino magnetic moment are not directly comparable between different types of neutrino experiments.

2.1.2 Measuring the Neutrino Magnetic Moment

The most sensitive method to measure the neutrino magnetic moment is the low energy elastic scattering of (anti)neutrinos on electrons [106]. The schematic diagram for this interaction is shown in Fig. 2.2, where the recoil electron's kinetic energy is defined as ($T_e = E_{e\prime} - m_e$) and the recoil angle with respect to the incoming neutrino beam (θ) is shown.

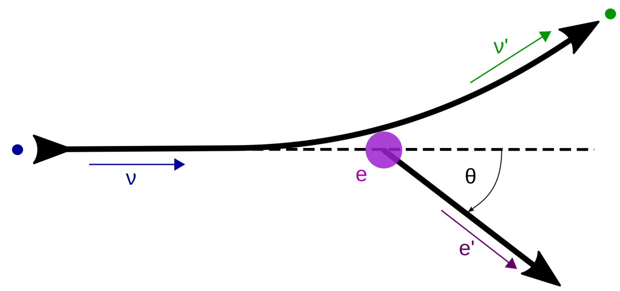

Figure 2.2: Neutrino-on-electron elastic scattering diagram

Since the ν-on-e interaction is governed by simple $2 \to 2$ kinematics, it can be shown that

$$(P_\nu - P_{e'})^2 = (P_{\nu'} - P_e)^2 , \tag{2.12}$$

$$m_\nu^2 + m_e^2 - 2E_\nu E_{e'} + 2E_\nu p_{e'} \cos\theta = m_\nu^2 + m_e^2 - 2E_{\nu'} m_e . \tag{2.13}$$

From the energy conservation

$$E_\nu + m_e = E_{\nu'} + E_{e'} = E_{\nu'} + T_e + m_e \Rightarrow E_{\nu'} = E_\nu - T_e \tag{2.14}$$

it follows that

$$E_\nu p_{e'} \cos\theta = E_\nu E_{e'} - E_{\nu'} m_e = E_\nu (T_e + m_e) - (E_\nu - T_e) m_e = T_e (E_\nu + m_e) , \tag{2.15}$$

$$\cos\theta = \frac{E_\nu + m_e}{E_\nu} \sqrt{\frac{T_e^2}{E_{e'}^2 - m_e^2}} = \frac{E_\nu + m_e}{E_\nu} \sqrt{\frac{T_e^2}{T_e^2 + 2T_e m_e}} . \tag{2.16}$$

And finally

$$\cos\theta = \frac{E_\nu + m_e}{E_\nu} \sqrt{\frac{T_e}{T_e + 2m_e}} . \tag{2.17}$$

Which can be rearranged to get

$$T_e = \frac{2m_e E_\nu^2 \cos^2\theta}{(E_\nu + m_e)^2 - E_\nu^2 \cos^2\theta}. \tag{2.18}$$

The electron's kinetic energy is therefore constrained as

$$T_e \leq \frac{2E_\nu^2}{2E_\nu + m_e}, \tag{2.19}$$

which corresponds to the limit $\cos\theta \to 1$ when the recoil electron goes exactly forward in the incident neutrino direction, as depicted in Fig. 2.3.

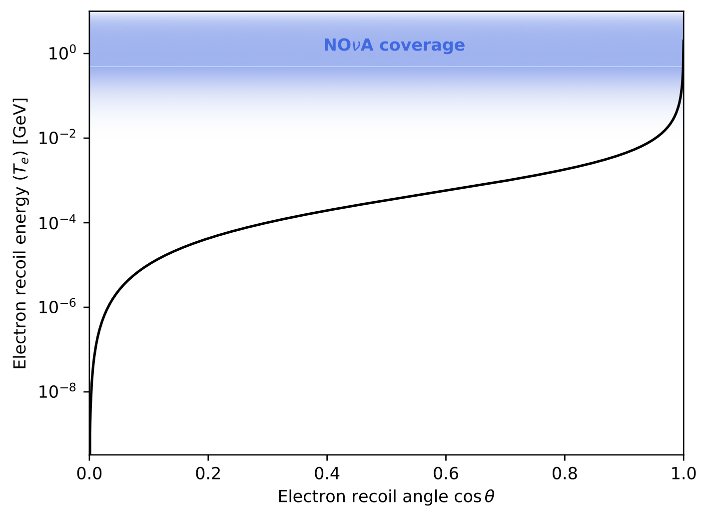

Figure 2.3: Relation between the recoil electron's kinetic energy and angle for the ν-on-e elastic scattering. The coverage of the NOvA detectors for measuring the electron recoil energy is shown in blue. Only very forward electrons are therefore recorded in NOvA.

Considering $E_\nu \sim$ GeV, it is useful to approximate $\frac{m_e^2}{E_\nu^2} \to 0$. Additionally, considering only very small electron recoil angles, meaning $\theta^2 \cong (1 - \cos^2\theta)$, applied to Eq. 2.17 results in

$$T_e\theta^2 \cong T_e\left(1 - \left(\frac{E_\nu + m_e}{E_\nu}\right)^2 \frac{T_e}{T_e + 2m_e}\right) = T_e\left(1 - \left(1 + \frac{2m_e}{E_\nu}\right)\frac{T_e}{T_e + 2m_e}\right), \tag{2.20}$$

therefore

$$T_e\theta^2 \cong \frac{2m_e T_e}{T_e + 2m_e}\left(1 - \frac{T_e}{E_\nu}\right) = 2m_e\left(\frac{1}{1 + \frac{2m_e}{T_e}}\right)\left(1 - \frac{T_e}{E_\nu}\right), \tag{2.21}$$

and finally

$$T_e\theta^2 \cong 2m_e\left(1-\frac{T_e}{E_\nu}\right) < 2m_e. \tag{2.22}$$

This is a strong limit that very clearly distinguishes the ν-on-e elastic scattering events from other similar interactions involving single electron (mainly the ν_eCC interactions).

Neutrino Magnetic Moment Cross Section

In the ultra-relativistic limit, the neutrino magnetic moment interaction flips the neutrino helicity, while the SM weak interaction conserves it, which means it is possible to add the two contributions to the total ν-on-e cross section incoherently (without interference terms) [106]:

$$\frac{d\sigma_{\nu-on-e}}{dT_e} = \left(\frac{d\sigma_{\nu-on-e}}{dT_e}\right)_{\text{SM}} + \left(\frac{d\sigma_{\nu-on-e}}{dT_e}\right)_{\text{MAG}}. \tag{2.23}$$

The SM contribution can be expressed as [106, 114]:

$$\left(\frac{d\sigma_{\nu-on-e}}{dT_e}\right)_{\text{SM}} = \frac{2G_F^2 m_e}{\pi}\left\{g_1^2 + g_2^2\left(1-\frac{T_e}{E_\nu}\right)^2 - g_1 g_2\frac{m_e T_e}{E_\nu^2}\right\}, \tag{2.24}$$

where the coupling constants g_1 and g_2 differ between neutrino flavours and between neutrinos and antineutrinos. Their values are:

$$g_1^{\nu_e} = g_2^{\overline{\nu}_e} = \sin^2\theta_W + 1/2, \qquad g_2^{\nu_e} = g_1^{\overline{\nu}_e} = \sin^2\theta_W, \tag{2.25}$$

$$g_1^{\nu_{\mu,\tau}} = g_2^{\overline{\nu}_{\mu,\tau}} = \sin^2\theta_W - 1/2, \qquad g_2^{\nu_{\mu,\tau}} = g_1^{\overline{\nu}_{\mu,\tau}} = \sin^2\theta_W, \tag{2.26}$$

where $\sin^2\theta_W \cong 0.23$.

The total SM cross section, and therefore the number of SM ν-on-e interactions, depends on the neutrino energy and the minimum measured electron recoil energy. However, in general the cross section for for ν_e is about 2.5 times larger than for the $\overline{\nu}_e$, about 6 times larger than for $\nu_{\mu/\tau}$ and about 7 times larger than for $\overline{\nu}_{\mu/\tau}$.

The neutrino magnetic moment contribution is [106, 115]:

$$\left(\frac{d\sigma_{\nu-on-e}}{dT_e}\right)_{\text{MAG}} = \frac{\pi\alpha^2}{m_e^2}\left(\frac{1}{T_e}-\frac{1}{E_\nu}\right)\left(\frac{\mu_{\nu_l}}{\mu_B}\right)^2, \tag{2.27}$$

where α is the fine structure constant and μ_{ν_l} is the effective magnetic moment of ν_l. The total cross section now only depends on the neutrino energy and on the effective magnetic moment, but is the same for neutrinos and antineutrinos.

The comparison of the SM and the neutrino magnetic moment differential cross sections is shown in Fig.2.4. Whereas the SM cross section is approximately uniform for $T_e \rightarrow 0$, the neutrino magnetic moment cross section rises to infinity. However, this reach is limited by the experimental capabilities of detecting electrons with very low energies. The (possible) NOvA coverage is shown with a shaded blue region, with current capability reaching $T_e = 0.5\,\mathrm{GeV}$. Future analyses might extend this reach to lower T_e, with the lowest possible detectable electron recoil energy $T_{e,min} \approx 0.01\,\mathrm{GeV}$, as discussed in Sec. 1.2.

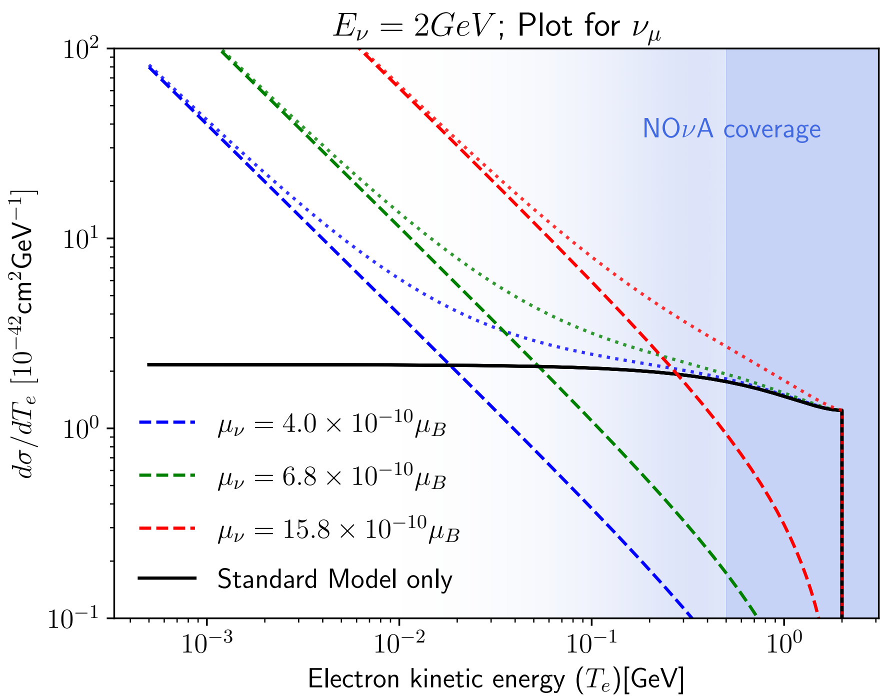

Figure 2.4: Comparison of the neutrino magnetic moment (coloured) and the SM (black) cross sections for the ν-on-e elastic scattering. Different colours depict different values of the neutrino magnetic moment, with red corresponding to the previous NOvA measurement, green the LSND result, and blue a possible ultimate NOvA sensitivity, as discussed in the introduction to this chapter. Dashed lines are the individual cross sections and dotted lines are the added total cross section with the standard model contribution. NOvA coverage of electron recoil energies is shown in shaded blue.

Calculating the ratio of the neutrino magnetic moment and the SM cross sections, as shown in Fig. 2.5, can serve as a proxy to estimate the number of neutrino magnetic moment events in relation to the predicted number of SM events, if the E_ν and T_e are known. Additionally, comparing the ratio of the total cross sections can reveal the expected total number of neutrino magnetic moment events as a function of the predicted number of SM events. Considering $E_\nu = 2\,\text{GeV}$, $\mu_\nu = 6.8 \times 10^{-10}\mu_B$ (current best limit for ν_μ from LSND), and integrating differential cross sections for ν_μ in Eq. 2.24 and 2.27 from $T_{e,min}$ to $T_{e,max} \to 2\,\text{GeV}$ results in

$$\frac{\sigma_{\text{MAG}}}{\sigma_{\text{SM}}} \approx \begin{cases} 0.035 & T_{e,min} = 0.5\,\text{GeV}, \\ 0.14 & T_{e,min} = 0.01\,\text{GeV}. \end{cases} \tag{2.28}$$

Therefore, at the current NOvA detection capabilities, there are about 0.035 times as many neutrino magnetic moment ν-on-e events than SM ones. This can be compared with the expected statistical uncertainty on the SM background, which in the case of Poisson distributed events is the square root of the number of predicted events. Consequently, it is possible to assess the minimal number of SM ν-on-e events necessary for the magnetic moment signal to be detected above the SM background (without considering systematic uncertainties) as

$$N_{SM} > 1/0.035^2 \approx 816. \tag{2.29}$$

However, this approximation is calculated only for one value of E_ν, but can be used to assess the sensitivity of the experiment.

As can be seen in Fig. 2.4 and Fig. 2.5, the magnetic moment contribution exceeds the SM contribution for low enough T_e. This can be approximated as [106]:

$$T_e \lesssim \frac{\pi^2\alpha^2}{G_F^2 m_e^3}\left(\frac{\mu_\nu}{\mu_B}\right)^2 \simeq 2.9 \times 10^{19}\left(\frac{\mu_\nu}{\mu_B}\right)^2 [\text{MeV}]\,, \tag{2.30}$$

which does not depend on the neutrino energy. Therefore, experiments sensitive to lower energetic electrons are significantly more sensitive to the neutrino magnetic moment.

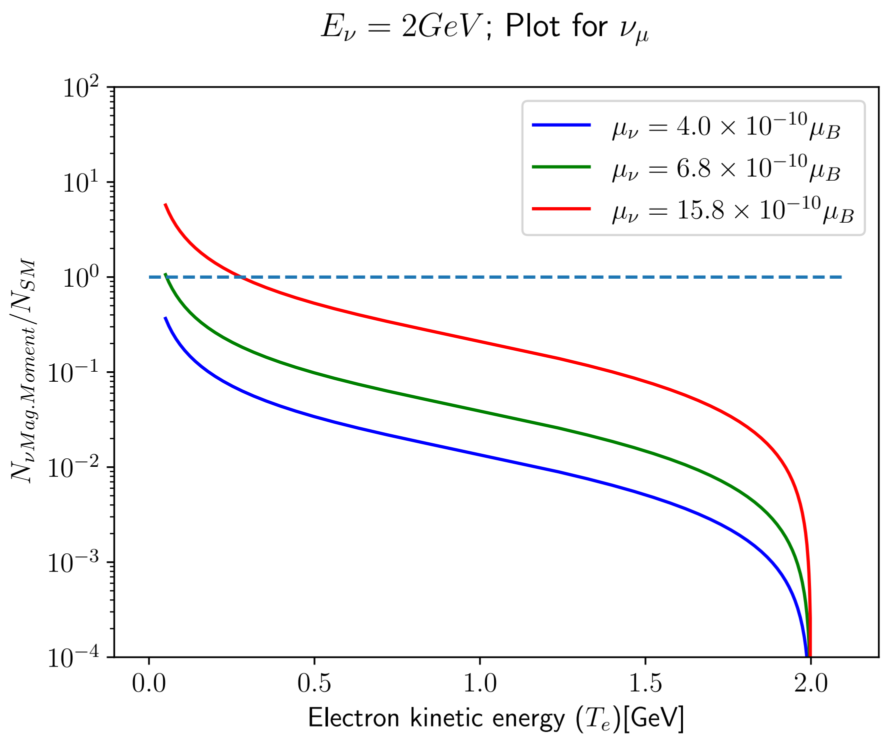

Figure 2.5: Ratio of the neutrino magnetic moment cross section to the SM cross section for the ν-on-e elastic scattering of 2 GeV ν_μ. Different colours depict different effective muon neutrino magnetic moment values, with red corresponding to the previous NOvA measurement, green the LSND result, and blue a possible ultimate NOvA sensitivity, as discussed in the introduction to this chapter.

2.2 Analysis Overview

Our analysis strategy for measuring the effective muon neutrino magnetic moment in the NOvA ND is based on comparing the total number of reconstructed and selected events in data with the prediction. The predicted events consist of the signal, which depends on the size of the effective muon neutrino magnetic moment, and of the background, which corresponds to the SM-only (null) hypothesis without any neutrino magnetic moment. We define the signal as true ν-on-e elastic scattering interactions, created with the use of the neutrino magnetic moment cross section instead of the SM cross section, as described in Sec. 2.1.2. Additionally, the signal events are required to have their true interaction vertex contained within the ND to exclude events originating from outside of the detector.

The data used in this analysis were collected from the start of NOvA ND data taking on the August 22$^{\text{nd}}$, 2014, until February 3$^{\text{rd}}$, 2021. This is the ND data that were used in the latest NOvA neutrino oscillations result [7], with an additional year. Although more data have been collected since February 2021, they are still being processed and are not available at the time of writing this thesis. The total exposure of the data sample is approximately 13.8×10^{20} POT. This exposure is used throughout this chapter to scale the predicted distributions and number of events.

This analysis uses the standard NOvA simulation and reconstruction tools, as were discussed in Sec. 1.4 and 1.5. The simulation was created with approximately four times larger statistics than the data to limit statistical uncertainties from simulation. The total exposure for the simulation is approximately 55.4×10^{20} POT. For the systematic uncertainty studies only a portion of this full sample is used, specifically 19.3×10^{20} POT.

Corrections for known limitations in the simulation are applied in the form of analysis weights applied to each event based on how it is affected by specific variations in the simulation. This includes the corrections for the neutrino beam prediction based on the external measurements used by the PPFX (Sec. 1.4), and, for the non-ν-on-e background only, also the internal and external measurements that constrain the neutrino interaction prediction inside GENIE.

The cross section corrections are not applied to the ν-on-e events, as they are assumed to be known precisely from theory. However, the GENIE MC simulation only considers tree-level SM ν-on-e interactions [103], as described in Sec. 2.1.2, and doesn't account for any higher order terms, which are described by radiative corrections. Radiative corrections can be expressed by two adjustments to the tree-level SM ν-on-e cross section [116]. First, the values of the weak coupling constants are changed as [117]

$$g_1^{\nu_e} \to 0.7276, \quad g_1^{\nu_\mu} \to -0.2730, \quad g_2 \to 0.2334. \tag{2.31}$$

Second, there are additional terms added to the cross section equation. Considering only one-loop corrections, the full ν-on-e cross section can be expressed as[1] [118]

$$\left(\frac{d\sigma_{\nu-on-e}}{dy}\right)_{\text{Rad. Corr.}} = \frac{G_F^2 s}{\pi}\left\{g_1^2\left(1+\frac{\alpha}{\pi}X_1\right)+g_2^2\left(1-y\right)^2\left(1+\frac{\alpha}{\pi}X_2\right)-g_1 g_2\frac{m_e y}{E_\nu}\right\}, \tag{2.32}$$

where

$$y = \frac{T_e + E_\gamma}{E_\nu}, \tag{2.33}$$

$s = 2E_\nu m_e + m_e^2$ is the Mandelstam variable,

$$X_1 = -\frac{2}{3}\log\left(\frac{2yE_\nu}{m_e}\right)+\frac{y^2}{24}-\frac{5y}{12}-\frac{\pi^2}{6}+\frac{23}{72} \tag{2.34}$$

and

$$X_2 = -\frac{2}{3}\left(1-y\right)^2\log\left(\frac{2yE_\nu}{m_e}\right)-\frac{y^2}{18}-\frac{\pi^2}{6}\left(1-y\right)^2-\frac{2y}{9}+\frac{23}{72}. \tag{2.35}$$

In practice, radiative corrections can be implemented as a weight, where each true ν-on-e event is weighted by a ratio

$$\text{weight}_{\text{Rad. Corr.}}\left(E_\nu, T_e\right) = \left(\frac{d\sigma_{\nu-on-e}}{dy}\right)_{\text{Rad. Corr.}} \Big/ \left(\frac{d\sigma_{\nu-on-e}}{dy}\right)_{\text{GENIE 3}}; \tag{2.36}$$

Analogically to the radiative correction weight, it is possible to create a neutrino magnetic moment weight as a ratio between the neutrino magnetic moment and the SM differential cross sections for the ν-on-e interactions. This can then serve to predict the number of ν-on-e events created by the neutrino magnetic moment interac-

[1]There is technically a third correction term X_3 by the $g_1 g_2$ term, which is however negligible for $E_\nu \sim$ GeV.

tion (which make up the signal), without the need for an additional simulation. This is possible thanks to the theoretically very well understood properties of the ν-on-e interaction, as described in Sec. 2.1.2. Therefore, the signal sample is created from the true ν-on-e sample, with the magnetic moment weight applied. The weight has a form:

$$\text{weight}_{\nu\text{Mag. Mom.}}(E_\nu, T_e) = \left(\frac{d\sigma_{\nu-on-e}}{dy}\right)_{\nu\text{Mag. Mom.}} \Bigg/ \left(\frac{d\sigma_{\nu-on-e}}{dy}\right)_{\text{GENIE 3}}, \tag{2.37}$$

where

$$\left(\frac{d\sigma_{\nu-on-e}}{dy}\right)_{\nu\text{Mag. Mom.}} = E_\nu \left(\frac{d\sigma_{\nu-on-e}}{dT_e}\right)_{\nu\text{Mag. Mom.}}. \tag{2.38}$$

Due to the relatively low cross section of the ν-on-e interaction, the nominal simulation sample contains very few ν-on-e events, which could result in a significant statistical uncertainty from simulation. To avoid this, we created a ν-on-e-enhanced simulation sample, which is mainly made up of ν-on-e events with a total exposure of 1.72×10^{24} POT. There are a few non-ν-on-e background events overlaid on top of the ν-on-e events to properly account for the possible reconstruction effects of the pileup of neutrino interactions in a single spill [103], since in the real detector, the hits from the true ν-on-e interaction can be clustered together into another interaction, or additional hits can be clustered together into the ν-on-e event. To save up on unnecessary disk space and processing usage, the enhanced ν-on-e sample does not include any cross section related parameters and variables, as the ν-on-e interaction is assumed to be known exactly from theory. Therefore, we do not apply cross section weights or account for cross section systematic uncertainties for ν-on-e events.

The cross section tuning procedure in NOvA (Sec. 1.4) applies large weights to MEC events in some parts of the parameter space. However, after the full event selection (Sec. 2.3) only a small number of MEC events remain in the detector. This was shown to be an issue especially for the ν_eCC MEC events [103]. Applying large tuning corrections to a small number of events results in large statistical fluctuations. To avoid this, we created another special sample with enhanced number of ν_eCC MEC events, following the same procedure as for the ν-on-e-enhanced sample, with an exposure of 1.99×10^{24} POT.

A summary of the simulation samples and analysis weights for the four different types of signal and background components is shown in Tab. 2.1. In the following chapter, the ν_eCC MEC background is added into the 'Other background' sample, even though it is created from a separate simulation.

Table 2.1: Overview of the simulation samples and analysis weight used for the different signal and background components.

Signal type	Sample	Weight
Signal	Enhanced ν-on-e	Flux & ν Mag. Moment
ν-on-e background	Enhanced ν-on-e	Flux & Rad. Corr.
ν_eCC MEC background	Enhanced ν_eCC MEC	Flux & Cross Sec.
Other background	Nominal ND	Flux & Cross Sec.

2.3 Event Selection

We are searching for ν-on-e elastic scattering events, characterised by a single very forward going electron shower, specifically focusing on low electron recoil energies. The main backgrounds for our analysis come from ν_eCC interactions, which produce an electron with additional activity, and interactions that produce π^0, which decays into two photons producing electromagnetic showers, where each can look similar to the ν-on-e signal. Additionally, there are ν_μCC interactions, which are generally easy to distinguish from our signal, however, their very high abundance in the NOvA ND makes them a dominant background nevertheless.

I explain the motivation behind each cut of the event selection and discuss their effect on the neutrino magnetic moment events below. I also consider possible improvements to the event selection for a future (re-)analysis.

The strategy for event selection is as follows. First, I remove events that failed reconstruction or data collection, described in Sec. 2.3.1 and 2.3.2. Then, I apply preselection cuts that remove obvious background (Sec. 2.3.3), while limiting the reduction of the signal efficiency to about $0.25\,\%$. Following this, I apply the containment cuts (Sec. 2.3.4) that remove events that are either not fully contained within the detector, or events that originate from outside of the detector, such as rock muons. Afterwards, I perform a cut-based Multi Variate Analysis (MVA) on a selection of variables useful for distinguishing the signal from the background, discussed in Sec. 2.3.5, and evaluate their combined performance on the signal selection. I choose the cut values that result in the best statistical significance, based on a chosen Figure Of Merit (FOM). Given that we are searching for a very limited number of signal events on top of a large background, I chose a simple statistics-only FOM

$$\text{FOM} = \frac{\text{Signal}}{\sqrt{\text{Background}}}. \tag{2.39}$$

The summary of the cut values for the event selection of neutrino magnetic moment signal is presented in Tab. 2.2, showing the label for the event selection variable, its description and the cut value chosen. After the full event selection, the predicted number of signal events for $\mu_\nu = 10^{-9}\mu_B$ is 56.80 and the total number of background events under the SM hypothesis is 700.33.

2.3.1 Data Collection Quality

To ensure good data quality, we apply the following criteria to data (not applied to simulation) [119]. A cut on the time of each spill relative to other spills and on the exposure of each spill, where every spill is required to have at least 2^{12} POT. Additionally, the current in the focusing horn is required to be within $-202\,\mathrm{kA} < I_{Horn} < -196.4\,\mathrm{kA}$, the position of the beam to be within $\pm 2\,\mathrm{cm}$ in both x and y axis, and that the width of the beam to be within 0.57 and $1.58\,\mathrm{cm}$. Furthermore, incomplete events, or events with issues in one or more DCMs are removed.

2.3.2 Reconstruction Quality

As described in Sec. 1.5, electrons are reconstructed by slicing, then vertexing, then clustering into prongs. To identify electrons we require a valid reconstructed vertex and at least one reconstructed prong. Even though electrons only consist of a single shower, we don't reject events with more than one prong in a slice, as the reconstruction can wrongly assign noise hits as a separate prong. These false secondary prongs can be removed later in the event selection.

Figure 2.6 and Tab. 2.3 show that about $68\,\%$ of signal events do not have a valid reconstructed vertex. This is due to the concentration of signal events at very low electron recoil energies, which results in events that can consist of a small number of hits, or even a single hit. As can be seen in the bottom plot in Fig. 2.6, events with small true electron recoil energies have much smaller vertex reconstruction efficiency than the higher energetic electrons. However, ongoing work is improving the vertex reconstruction in the NOvA detectors with a use of ML instead of the currently used Hough transform combined with Elastic Arms [120]. Improving NOvA vertex reconstruction at low energies can enhance our event selection in the future.

Table 2.2: Summary of the variables and their cut values for the event selection of neutrino magnetic moment signal. Showing the category of the event selection variable, its label, description and the cut value chosen.

	Label	Description	Cut
Reco Qual.	**Valid Vtx**	Valid reconstructed vertex	> 0
	N^o Prongs	Number of reconstructed prongs	> 0
	Hits / Plane	Number of hits per plane	< 6
	Low E_{Shower}	Low cut on calorimetric energy of the most energetic shower	$> 0.5\,\mathrm{GeV}$
Pre-selection	**N^o Hits Loose**	Preliminary cut on the total number of hits for all prongs in a slice	< 280
	Prong Length	Length of the longest prong	$< 640\,\mathrm{cm}$
	$E\theta^2$ **Loose**	Preliminary cut on the product of the calorimetric energy and angle squared of the leading shower	$< 0.064\,\mathrm{GeV} \times \mathrm{rad}^2$
Fiducial	**Vertex**	x position	$> -177\,\mathrm{cm}$ $< 177\,\mathrm{cm}$
		y position	$> -177\,\mathrm{cm}$ $< 177\,\mathrm{cm}$
		z position	$> 50\,\mathrm{cm}$ $< 1170\,\mathrm{cm}$
Containment	**Prong**	Minimum hit position in x	$> -177\,\mathrm{cm}$
		Maximum hit position in x	$< 177\,\mathrm{cm}$
		Minimum hit position in y	$> -185\,\mathrm{cm}$
		Maximum hit position in y	$< 177\,\mathrm{cm}$
		Minimum hit position in z	$> 55\,\mathrm{cm}$
		Maximum hit position in z	$< 1270\,\mathrm{cm}$
Selection	E_{Shower}/E_{Tot}	Fraction of energy contained in the most energetic shower	> 0.91
	N^o Hits	Total number of hits for all prongs in a slice	< 116
	High E_{Shower}	Calorimetric energy of the most energetic shower	$< 1.4\,\mathrm{GeV}$
	ν-on-e ID	CVN-based ν-on-e identifier	> 0.65
	$E\pi^0$ **ID**	CVN-based ν-on-e and π^0 identifier	> 0.63
	$E\theta^2$	Product of the calorimetric energy and angle squared of the leading shower	$< 0.0048\,\mathrm{GeV} \times \mathrm{rad}^2$

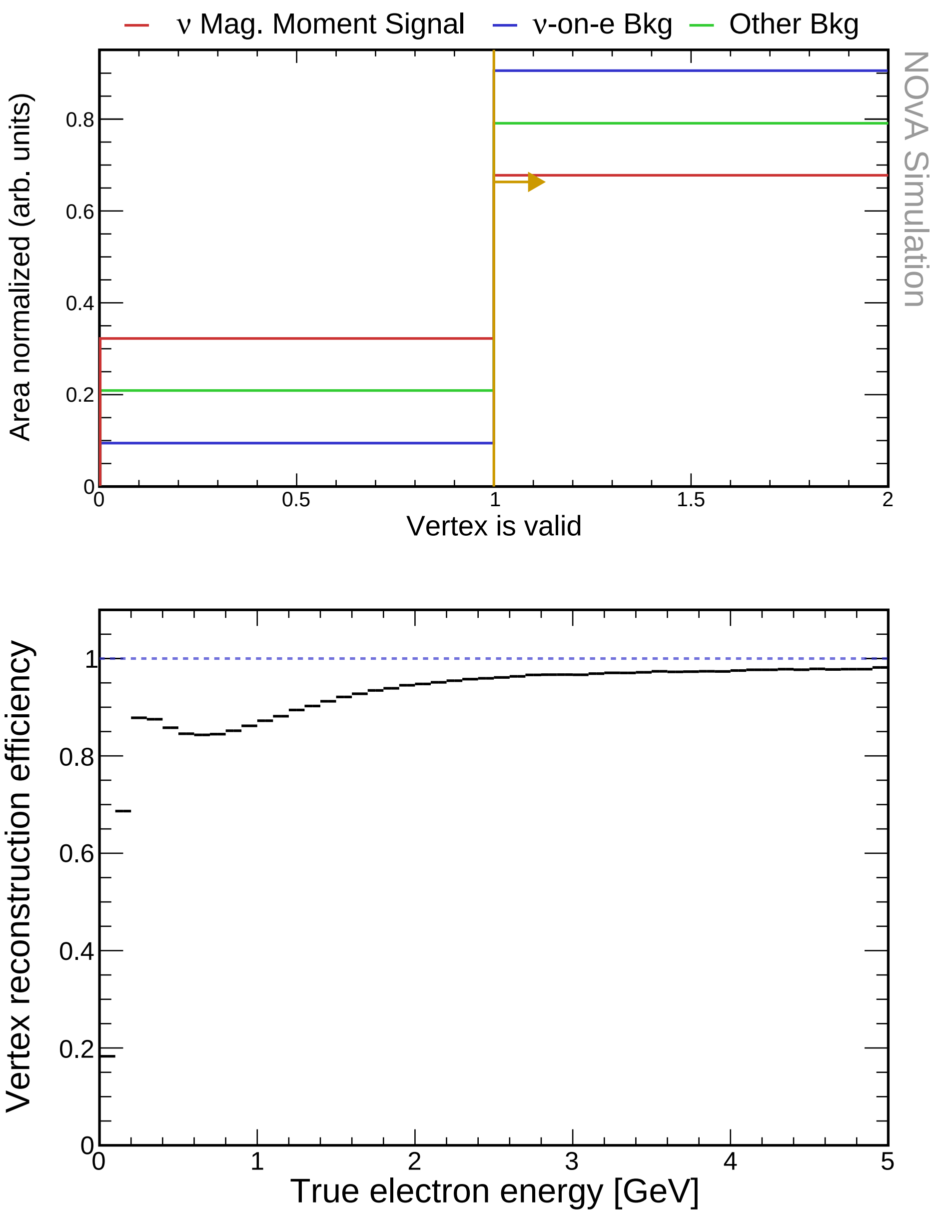

Figure 2.6: Top: Relative comparison of the signal (red), ν-on-e background (blue), and other background (green) events for the vertex reconstruction quality selection. Each histogram is area-normalised and the first bin corresponds to events without a valid vertex and second bin to events with correctly reconstructed vertex. The yellow line indicates the chosen cut value, where all events have to have a valid reconstructed vertex. Bottom: profile histogram of the 'vertex is valid' variable as a function of the true electron energy for the true signal events, showing the significant drop in vertex reconstruction efficiency at low electron recoil energies. No selection was applied prior to making these plots.

Additionally, we limit the number of hits per plane to < 6. This is to remove the so-called 'FEB flashers', which are caused by such a high energy deposit in one cell, that it affects all the other channels on the same APD [121]. The cut value was chosen so that it removes approximately $0.25\,\%$ signal events, which is the same criterion as is used for the pre-selection cuts described below. Relative comparisons between signal and background for the number of prongs and the number of hits per plane are shown in Fig. 2.7.

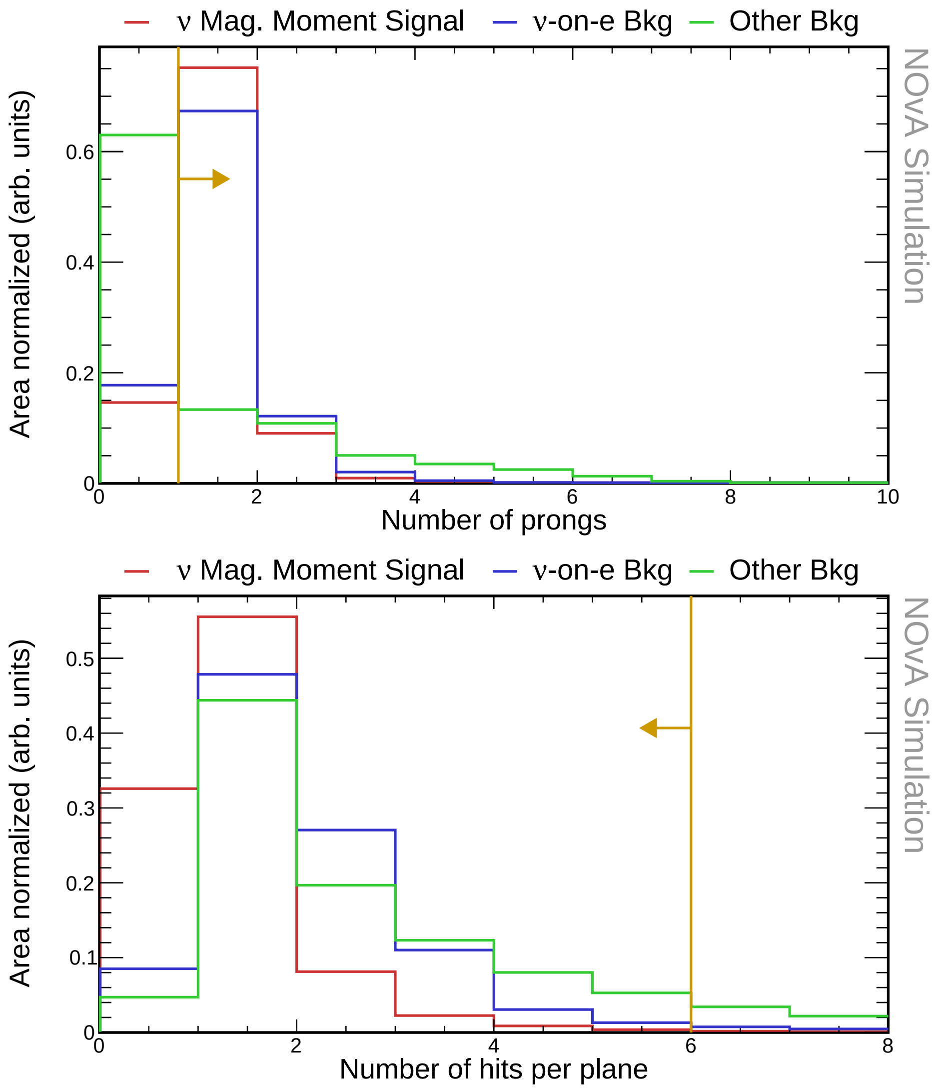

Figure 2.7: Relative comparison of signal (red), ν-on-e background (blue), and other background (green) events in the number of prongs (top) and the number of hits per plane (bottom) distributions. Events in both plots are required to have a valid reconstructed vertex and in the bottom plot also at least one reconstructed prong. Yellow lines indicate the cut values for the shown variables, with arrows pointing towards the preserved events. All histograms are area-normalised.

Furthermore, the reconstructed calorimetric energy of the primary shower is required to be $E_{cal} > 0.5\,\mathrm{GeV}$ as shown in Fig. 2.8. This is primarily due to the limitations of the currently used CVN-based ν-on-e identifiers described in Sec. 2.3.5, which were developed and validated for ν-on-e events with energies above this limit, to avoid the large background at low energies. However, due to the nature of the neutrino magnetic moment signal, which is concentrated at low electron recoil energies, this cut also removes a majority of our signal events, specifically $66.8\,\%$. This large reduction severely impacts the significance of our measurement. On the other hand, it also marks potentially the most impactful improvement available in a future re-analysis. There are other event identifying algorithms available in NOvA that could be explored for ν-on-e events to leverage the low energy sample. Additionally, it is possible to develop a purpose-built ν-on-e identifier focusing on low electron recoil energies.

Table 2.3: Event selection cutflow table for the reconstruction quality cuts showing the number of events and the relative efficiency of each cut for each signal sample. The relative efficiency is calculated as number of events remaining after applying the corresponding cut divided by number of events for all the previous cuts. All the cuts are listed in sequence as they are applied.

Selection	**Signal**		**ν-on-e bkg**		**Other bkg**	
	N_{evt}	ϵ_{rel} (%)	N_{evt}	ϵ_{rel} (%)	N_{evt}	ϵ_{rel} (%)
No Cut	817.34	100	6.82×10^3	100	2.96×10^8	100
Valid Vtx	553.86	67.76	6.17×10^3	90.55	2.34×10^8	79.10
N^o Prongs	472.90	85.38	5.08×10^3	82.25	8.66×10^7	37.00
Hits / Plane	471.14	99.63	4.97×10^3	97.85	7.32×10^7	89.56
Low E_{Shower}	156.37	33.19	3.53×10^3	71.09	4.06×10^7	55.12

2.3.3 Pre-Selection

Pre-selection aims to remove obvious background events without significantly affecting the signal. The criterion we chose for the selection of these cuts is determined by the reduction of the signal efficiency by approximately $0.25\,\%$ with each cut. This results in the total pre-selection reduction of the signal efficiency by approximately $1\,\%$.

The first two variables used for our pre-selection are the same as were used in the event selection for the ν_e appearance ND constraint for the three flavour neutrino oscillation measurements [7]. As we are searching for single electron showers, we

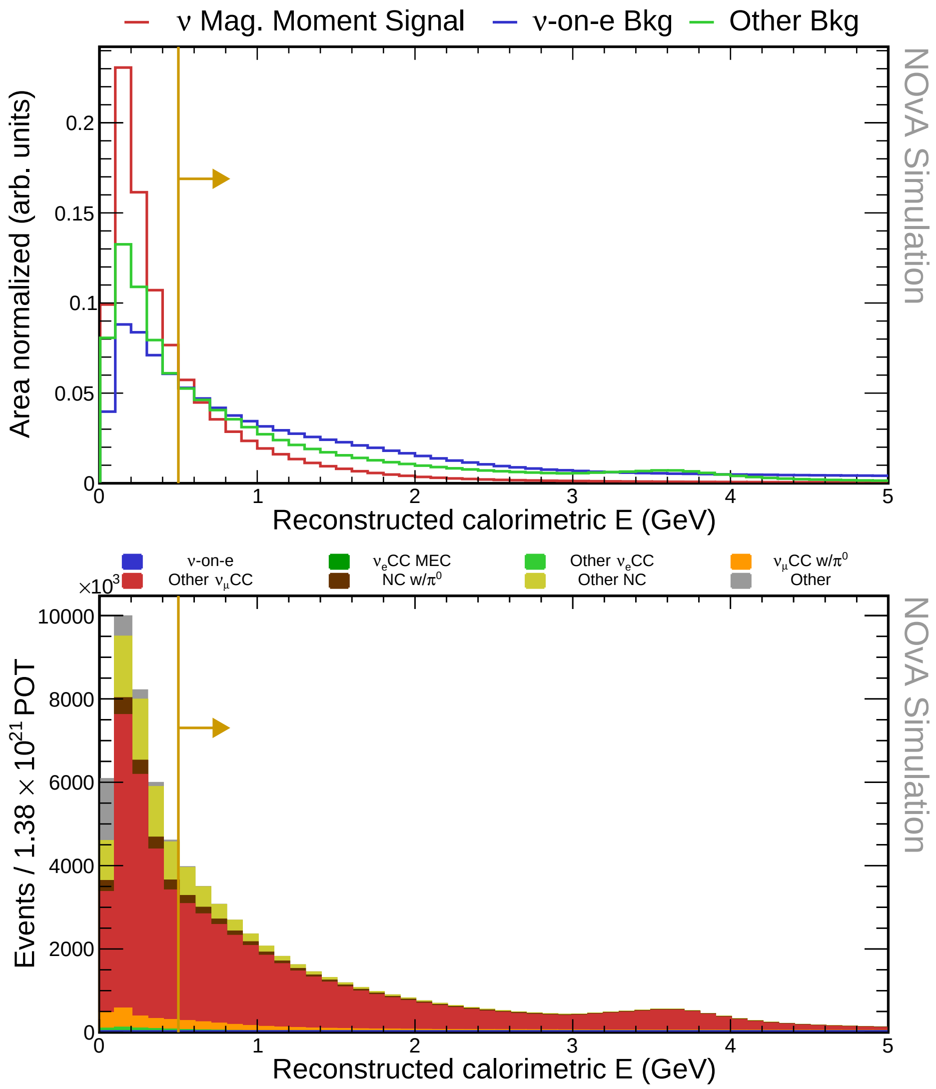

Figure 2.8: Top: Relative comparison of signal (red), ν-on-e background (blue), and other background (green) events in the reconstructed calorimetric energy distribution. All histograms are area-normalised. Bottom: Decomposition of background into various sub-samples, normalised to the data POT exposure. Events in both plots are required to have a valid reconstructed vertex, at least one reconstructed prong and less than 6 hits per plane. Yellow lines indicate the cut value for the reconstructed calorimetric energy, with arrows pointing towards the preserved events.

can reduce backgrounds with multiple final state particles by limiting the total activity in the detector. Specifically, we require that the total number of hits assigned to all the reconstructed prongs is < 280. This is shown in Fig. 2.9. In general, the main background in NOvA consists of the ν_μCC interactions, which are characterised by long muon tracks. We therefore limit the length of the longest reconstructed prong to be $< 640\,\mathrm{cm}$, as shown in Fig. 2.10.

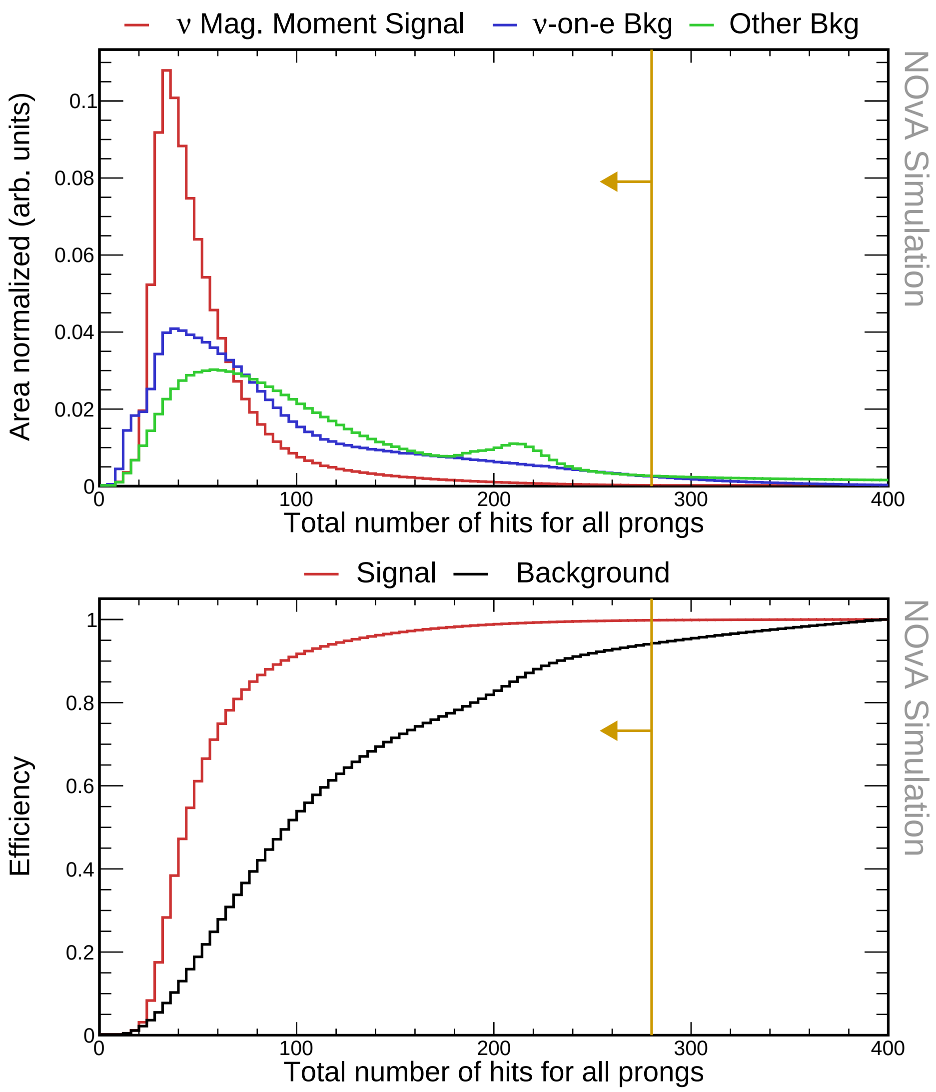

Figure 2.9: Top: Relative comparison of signal (red), ν-on-e background (blue), and other background (green) events in the distribution of total number of hits from all reconstructed prongs in the slice. All histograms are area-normalised. Bottom: Cumulative signal (red) and background (black) efficiency calculated as number of signal/background events left of the bin divided by the total number of signal/background events. Yellow lines indicate the cut value for the maximum number of hits, with arrows pointing towards the preserved events. The reconstruction quality cuts were applied before making these plots.

Additionally, as discussed in Sec. 2.1.2, simple $2 \rightarrow 2$ kinematics dictate that

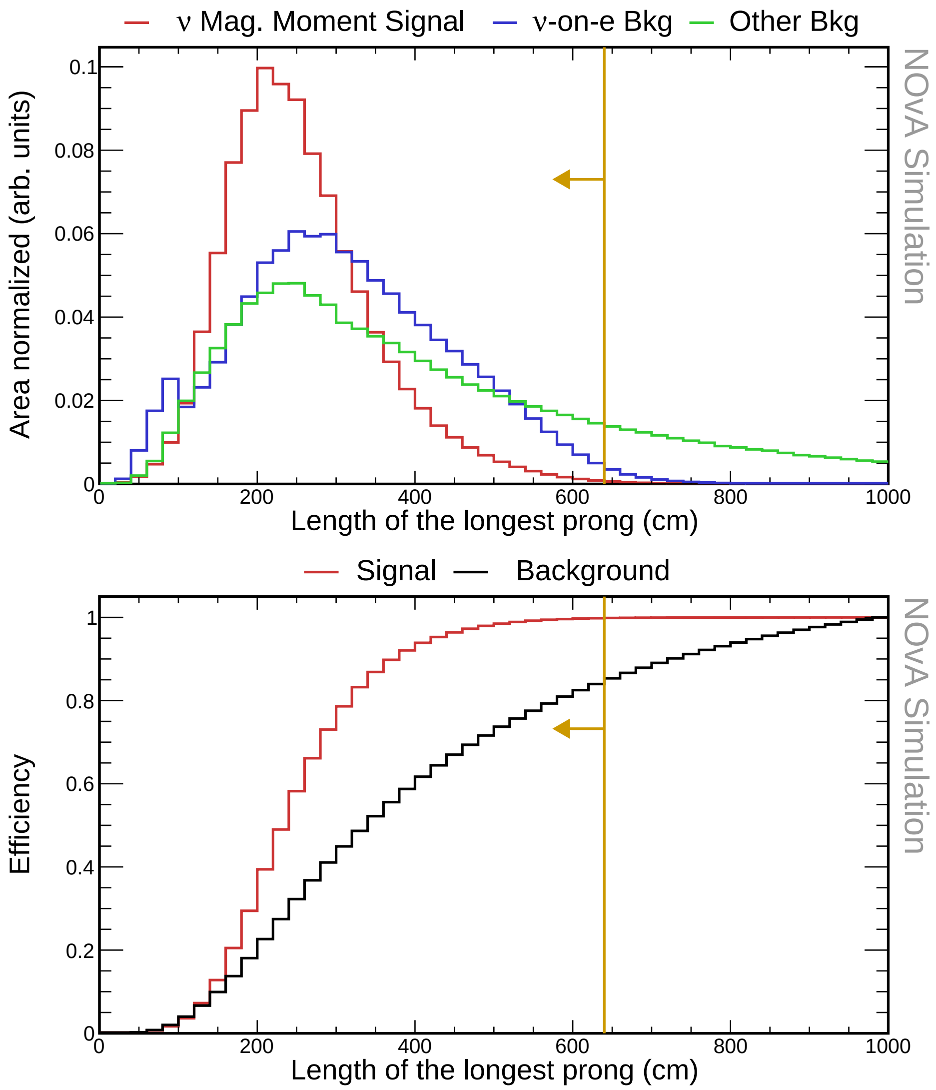

Figure 2.10: Top: Relative comparison of signal (red), ν-on-e background (blue), and other background (green) events in the distribution of the length of the longest reconstructed prong in slice. All histograms are area-normalised. Bottom: Cumulative signal (red) and background (black) efficiency calculated as number of signal/background events left of the bin divided by the total number of signal/background events. Yellow lines indicate the cut value for the maximum length of the longest prong, with arrows pointing towards the preserved events. The reconstruction quality cuts and the number of hits cut were applied before making these plots.

the true electron recoil energy and angle for the ν-on-e interaction are limited by $E\theta^2 < 2m_e$. This can be used to distinguish ν-on-e elastic scattering from ν_eCC interactions, which also have an electron in the final state. However, due to unavoidable reconstruction deficiencies, the reconstructed $E\theta^2$ does not have such a strict cut-off value, and we are placing the pre-selection cut at $E\theta^2 < 0.064$, as can be seen in Fig. 2.11. Furthermore, some of the signal events can be reconstructed with the opposite direction with respect to the beam, which would result in $\theta \approx \pi\,\mathrm{rad}$. However, this reconstruction failure likely does not impact other reconstructed qualities and these events should be preserved for the final sample. For that reason, we are calculating the angle between the outgoing electron and the neutrino beam direction as $\arccos(\text{abs}(\cos\theta))$, which gives the same value whether the shower is reconstructed forward or backwards.

The effect of the pre-selection cuts on the signal and background samples are summarised in Tab. 2.4, where the first row lists the number of events after applying all the reconstruction quality cuts from Sec. 2.3.2. All three of the variables used for the pre-selection are employed again in the MVA, as described in Sec. 2.3.5.

Table 2.4: Pre-selection cutflow table showing the number of events and the relative efficiency of each cut for each signal sample. The relative efficiency is calculated as number of events remaining after applying the corresponding cut divided by number of events for all the previous cuts. All the cuts are listed in sequence as they are applied. The top row corresponds to the sample after applying the reconstruction quality cuts.

Selection	Signal		ν-on-e bkg		Other bkg	
	N_{evt}	ϵ_{rel} (%)	N_{evt}	ϵ_{rel} (%)	N_{evt}	ϵ_{rel} (%)
Reco Quality	156.37	100	3.53×10^3	100	4.28×10^7	100
N^o Hits Loose	156.05	99.79	3.41×10^3	96.46	3.61×10^7	84.35
Prong Length	155.7	99.78	3.37×10^3	98.85	2.61×10^7	72.36
$E\theta^2$ **Loose**	155.14	99.64	3.33×10^3	98.83	8.83×10^6	33.82

2.3.4 Fiducial and Containment Cuts

To ensure all the deposited energy of the recoil electron is contained within the detector and to remove events originating outside of the detector (such as rock muons for the ND), we constrain the position of the reconstructed vertex and all the prongs in the slice. The decision on where to place the exact cut values is made based on the maximum FOM value.

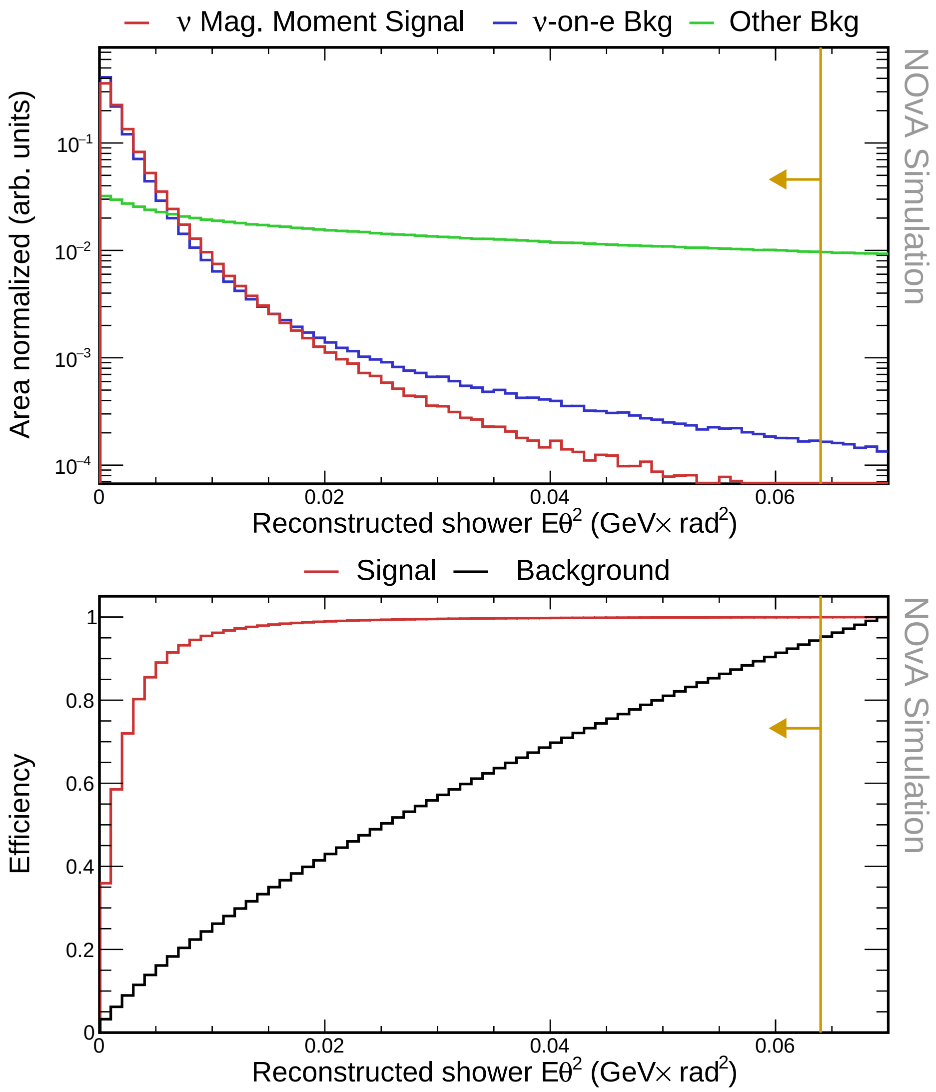

Figure 2.11: Top: Relative comparison of signal (red), ν-on-e background (blue), and other background (green) events in the distribution of the reconstructed energy of the leading shower multiplied by its angle from the incoming neutrino beam direction squared. All histograms are area-normalised with logarithmic y axis. Bottom: Cumulative signal (red) and background (black) efficiency calculated as number of signal/background events left of the bin divided by the total number of signal/background events. Yellow lines indicate the cut value for the depicted variable, with arrows pointing towards the preserved events. The reconstruction quality cuts, the number of hits cut, and the length of the longest prong cuts were applied before making both of these plots.

The reconstructed vertex is required to be within the fiducial volume, which represents a well-understood volume of the detector. To select the fiducial volume, we investigate distributions of the reconstructed vertex in the x, y and z direction, shown in Fig. 2.12, 2.13 and 2.14 respectively. Basic reconstruction quality and pre-selection cuts are applied to make these distributions. Additionally, for the x and y position distributions, we require that the vertex is not placed inside of the Muon Catcher by requiring $\mathsf{Vtx}_Z < 1270\,\mathrm{cm}$, as it can significantly affect these distributions. The slanted distributions in x and y are caused by the off-axis nature of the NuMI beam and the periodic peaks are due to a combination of the detector structure and the choice of binning.

The reconstructed vertex is required to be contained within the following volume:

$$-175\,\mathrm{cm} < \mathsf{Vtx}_X < 175\,\mathrm{cm}, \tag{2.40}$$

$$-175\,\mathrm{cm} < \mathsf{Vtx}_Y < 175\,\mathrm{cm}, \tag{2.41}$$

$$95\,\mathrm{cm} < \mathsf{Vtx}_Z < 1170\,\mathrm{cm}. \tag{2.42}$$

Furthermore, we constrain the extreme positions (minimum and maximum) of all the hits within the most energetic prong, which is assumed to represent the electron shower for the signal events. We apply the reconstruction quality, pre-selection and fiducial (vertex position) cuts to their distributions, shown in Fig. 2.15-2.20. The extreme hit positions are required to be within the following volume:

$$-175\,\mathrm{cm} < \mathsf{min}_X, \mathsf{max}_X < 175\,\mathrm{cm}, \tag{2.43}$$

$$-175\,\mathrm{cm} < \mathsf{min}_Y, \mathsf{max}_Y < 175\,\mathrm{cm}, \tag{2.44}$$

$$105\,\mathrm{cm} < \mathsf{min}_Z, \mathsf{max}_Z < 1270\,\mathrm{cm}. \tag{2.45}$$

2.3.5 Multivariate Analysis Cuts

Following the removal of obvious backgrounds and events not contained within the detector, we aim to optimise the event selection to achieve the highest significance for measuring the effective muon neutrino magnetic moment. This goal is equivalent to maximising our FOM from Eq. 2.39.

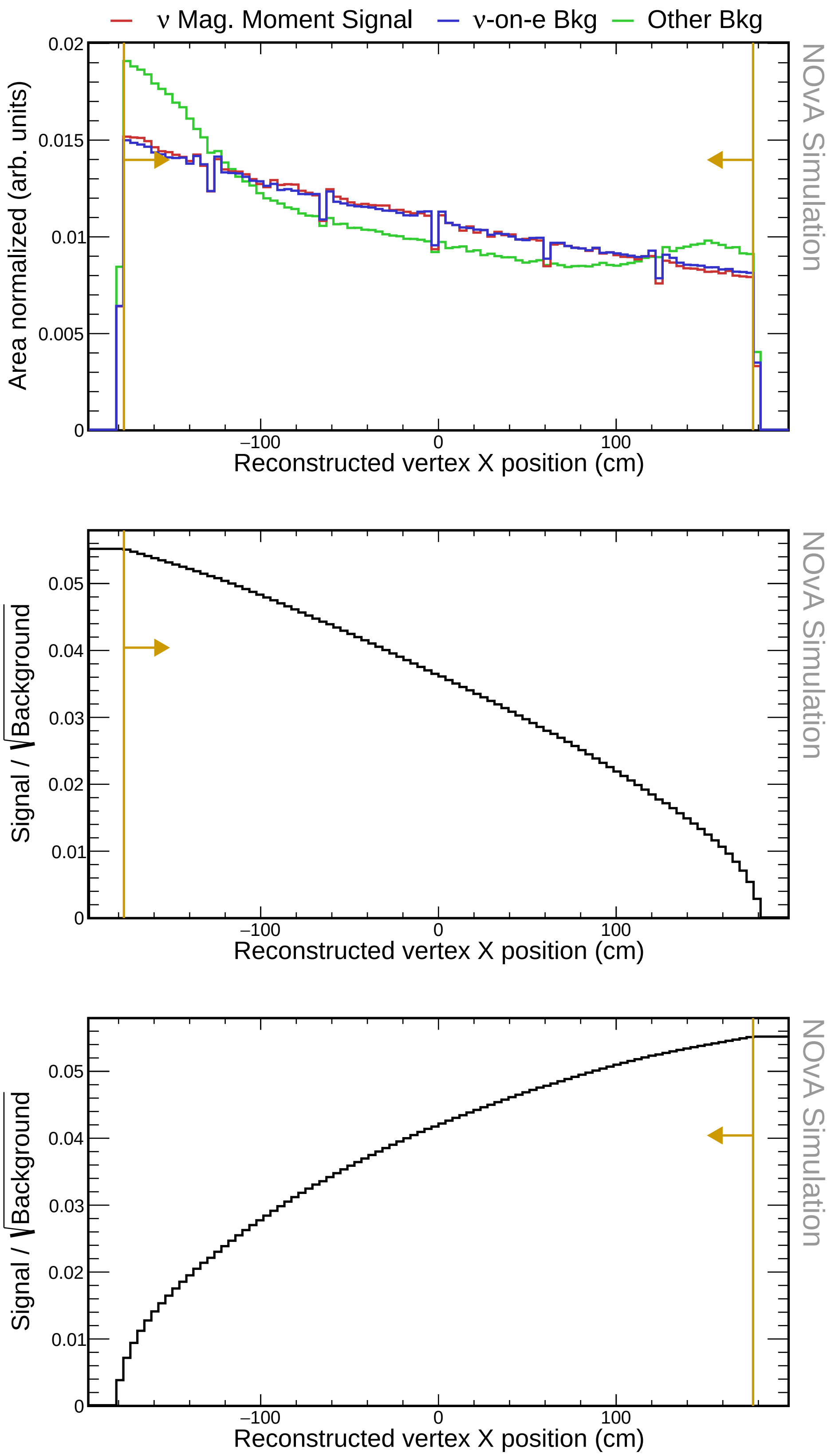

Figure 2.12: Top: Relative comparison of signal (red), ν-on-e background (blue), and other background (green) events in the distribution of the x position of the reconstructed vertex. All histograms are area-normalized. Middle and bottom: Cumulative FOM calculated as the number of signal events, divided by the number of background events from that bin until the end of the plot to the right (middle) or left (bottom). The reconstruction quality and pre-selection cuts were applied prior to making these plots. Additionally, vertex is required to be within the active region of the detector ($Vtx_Z < 1270\,\mathrm{cm}$). Yellow lines show the cut values that create the fiducial volume, with arrows pointing towards the preserved events.

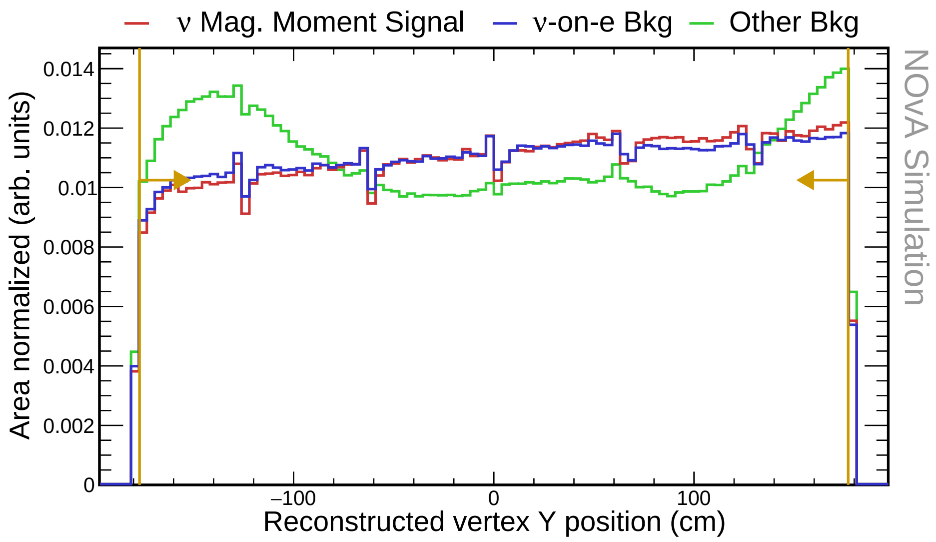

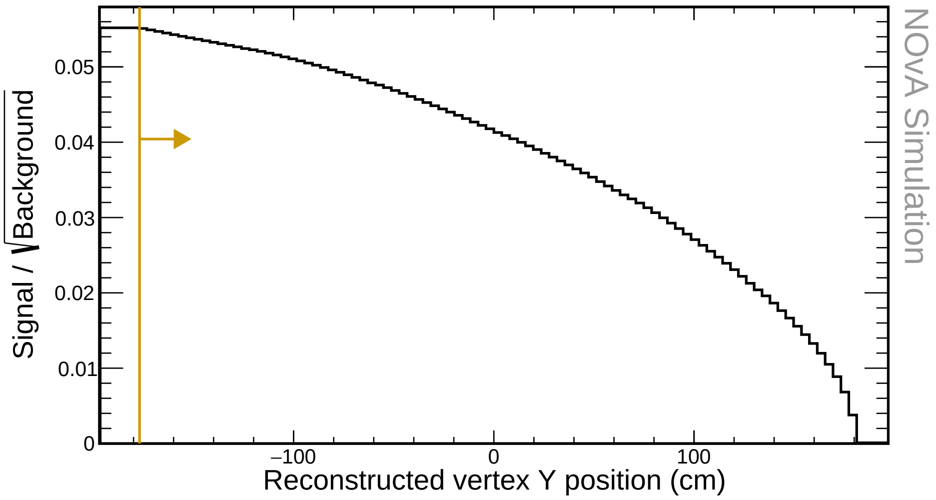

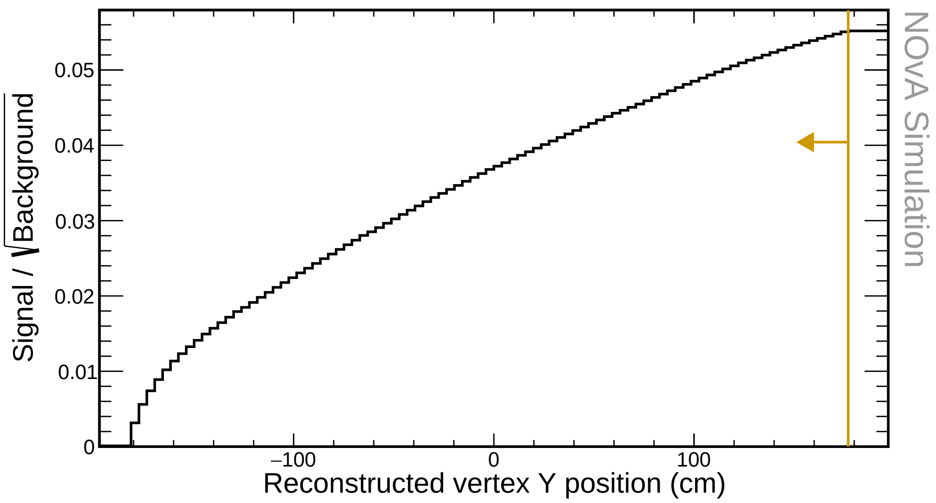

Figure 2.13: Top: Relative comparison of signal (red), ν-on-e background (blue), and other background (green) events in the distribution of the y position of the reconstructed vertex. All histograms are area-normalized. Middle and bottom: Cumulative FOM calculated as the number of signal events, divided by the number of background events from that bin until the end of the plot to the right (middle) or left (bottom). The reconstruction quality and pre-selection cuts were applied prior to making these plots. Additionally, vertex is required to be within the active region of the detector ($Vtx_Z < 1270\,\mathrm{cm}$). Yellow lines show the cut values that create the fiducial volume, with arrows pointing towards the preserved events.

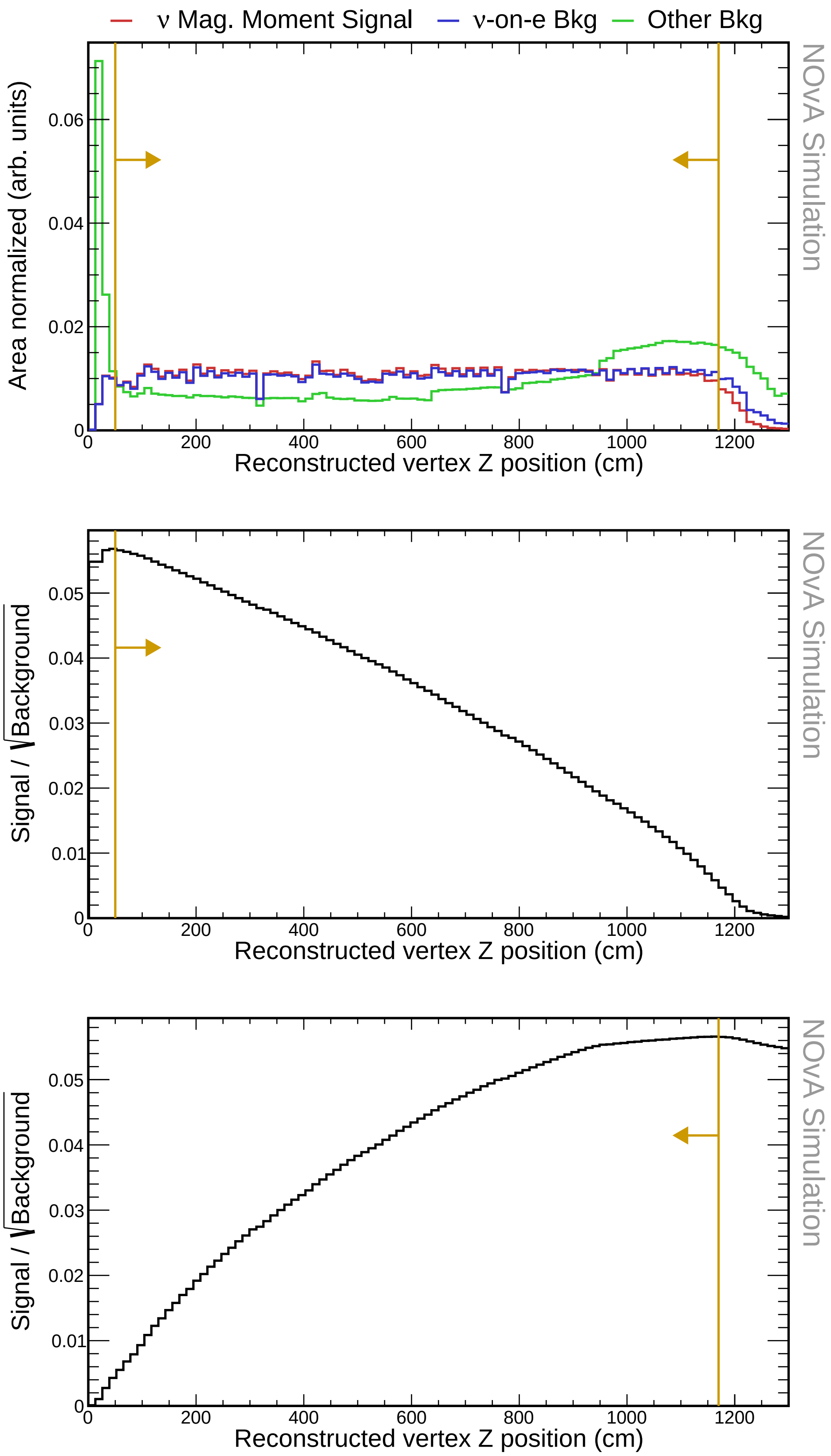

Figure 2.14: Top: Relative comparison of signal (red), ν-on-e background (blue), and other background (green) events in the distribution of the z position of the reconstructed vertex. All histograms are area-normalized. Middle and bottom: Cumulative FOM calculated as the number of signal events, divided by the number of background events from that bin until the end of the plot to the right (middle) or left (bottom). The reconstruction quality and pre-selection cuts were applied prior to making these plots. Yellow lines show the cut values that create the fiducial volume, with arrows pointing towards the preserved events.

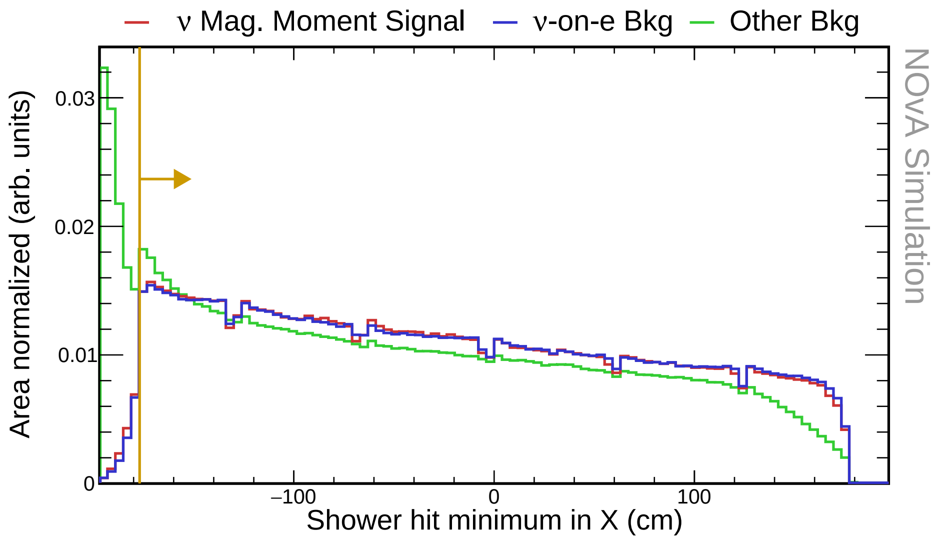

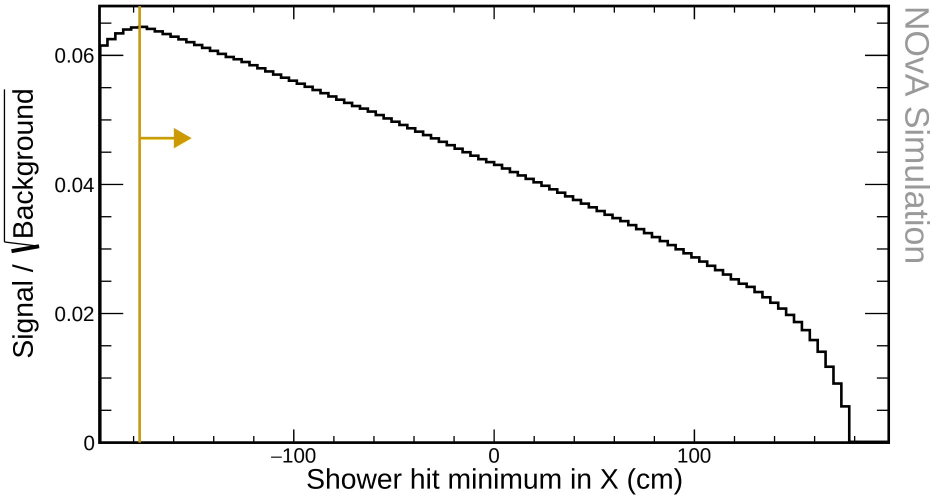

Figure 2.15: Top: Relative comparison of signal (red), ν-on-e background (blue), and other background (green) events in the distribution of the minimum hit position of the most energetic prong along the x axis. All histograms are area-normalized. Bottom: Cumulative FOM calculated as the number of signal events, divided by the number of background events from that bin until the end of the plot in the direction of the yellow arrow. The reconstruction quality, pre-selection and fiducial cuts were applied prior to making these plots. Yellow lines show the cut values that create the containment volume, with arrows pointing towards the preserved events.

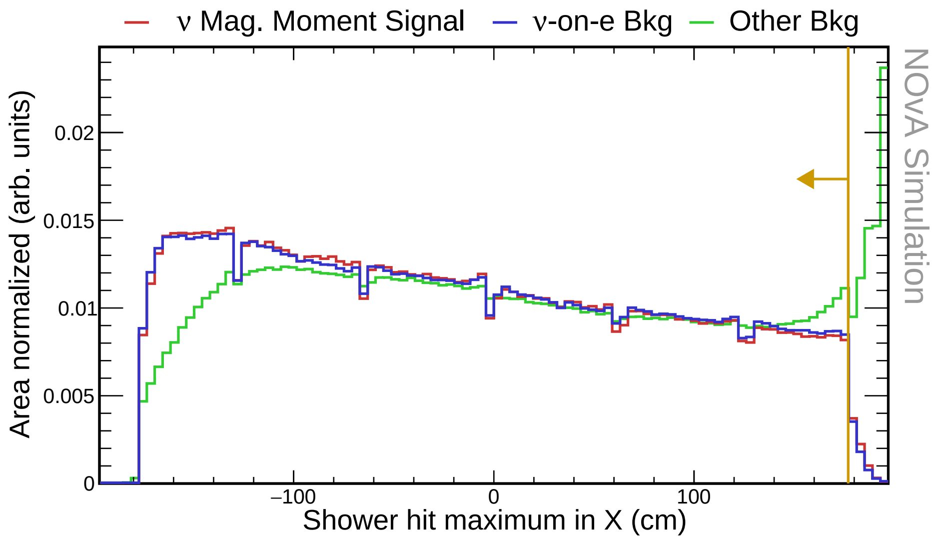

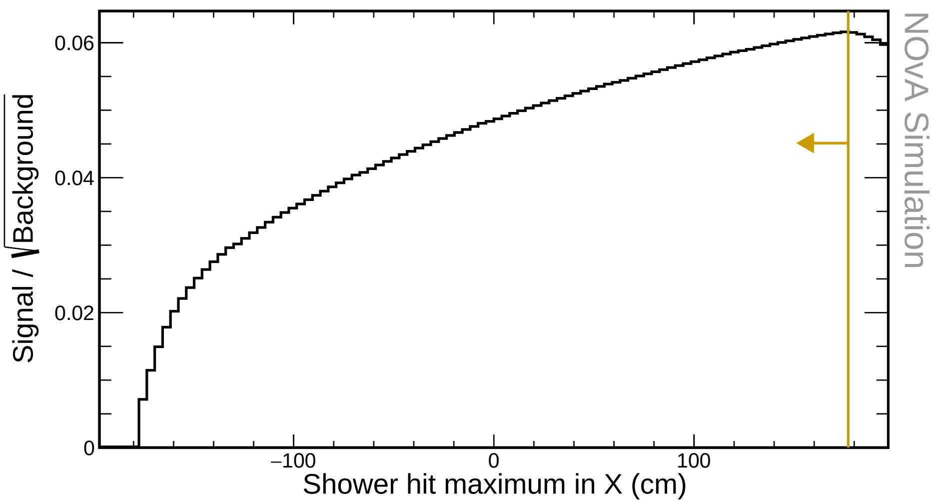

Figure 2.16: Top: Relative comparison of signal (red), ν-on-e background (blue), and other background (green) events in the distribution of the maximum hit position of the most energetic prong along the x axis. All histograms are area-normalized. Bottom: Cumulative FOM calculated as the number of signal events, divided by the number of background events from that bin until the end of the plot in the direction of the yellow arrow. The reconstruction quality, pre-selection and fiducial cuts were applied prior to making these plots. Yellow lines show the cut values that create the containment volume, with arrows pointing towards the preserved events.

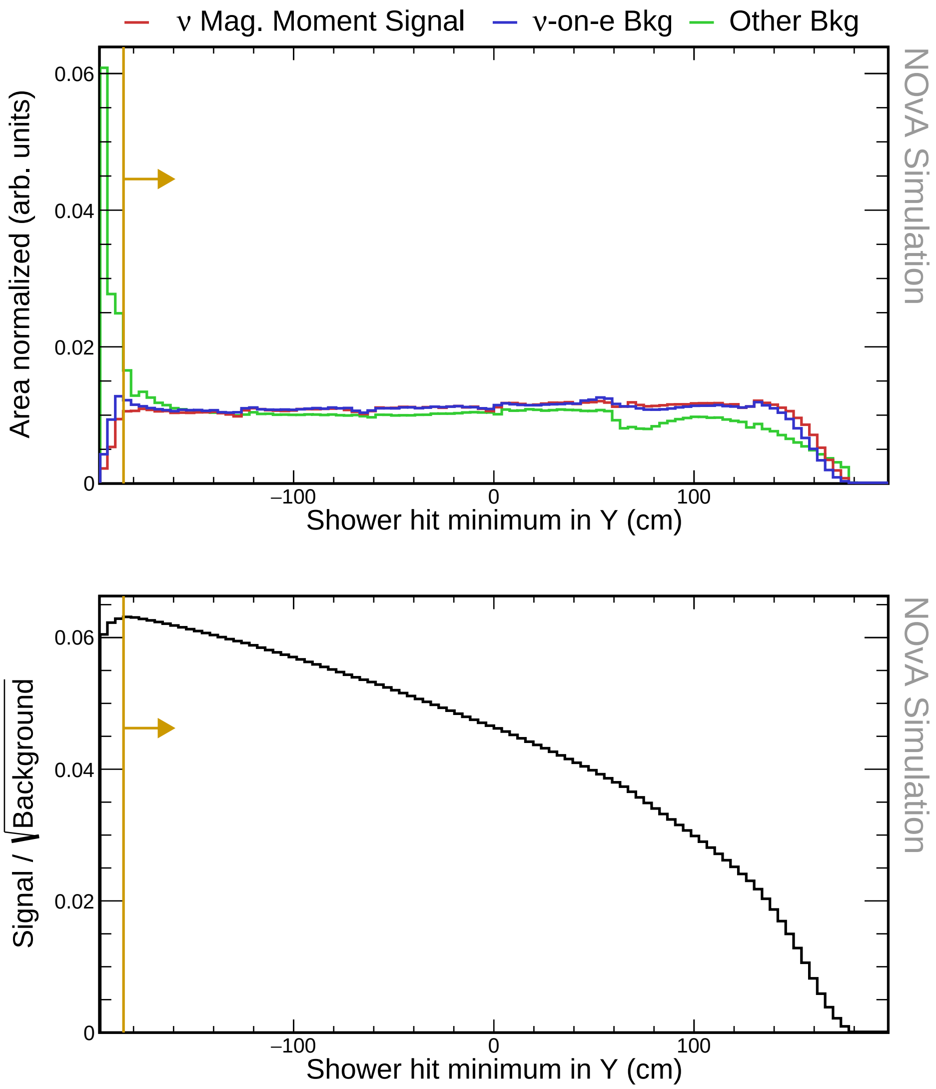

Figure 2.17: Top: Relative comparison of signal (red), ν-on-e background (blue), and other background (green) events in the distribution of the minimum hit position of the most energetic prong along the y axis. All histograms are area-normalized. Bottom: Cumulative FOM calculated as the number of signal events, divided by the number of background events from that bin until the end of the plot in the direction of the yellow arrow. The reconstruction quality, pre-selection and fiducial cuts were applied prior to making these plots. Yellow lines show the cut values that create the containment volume, with arrows pointing towards the preserved events.

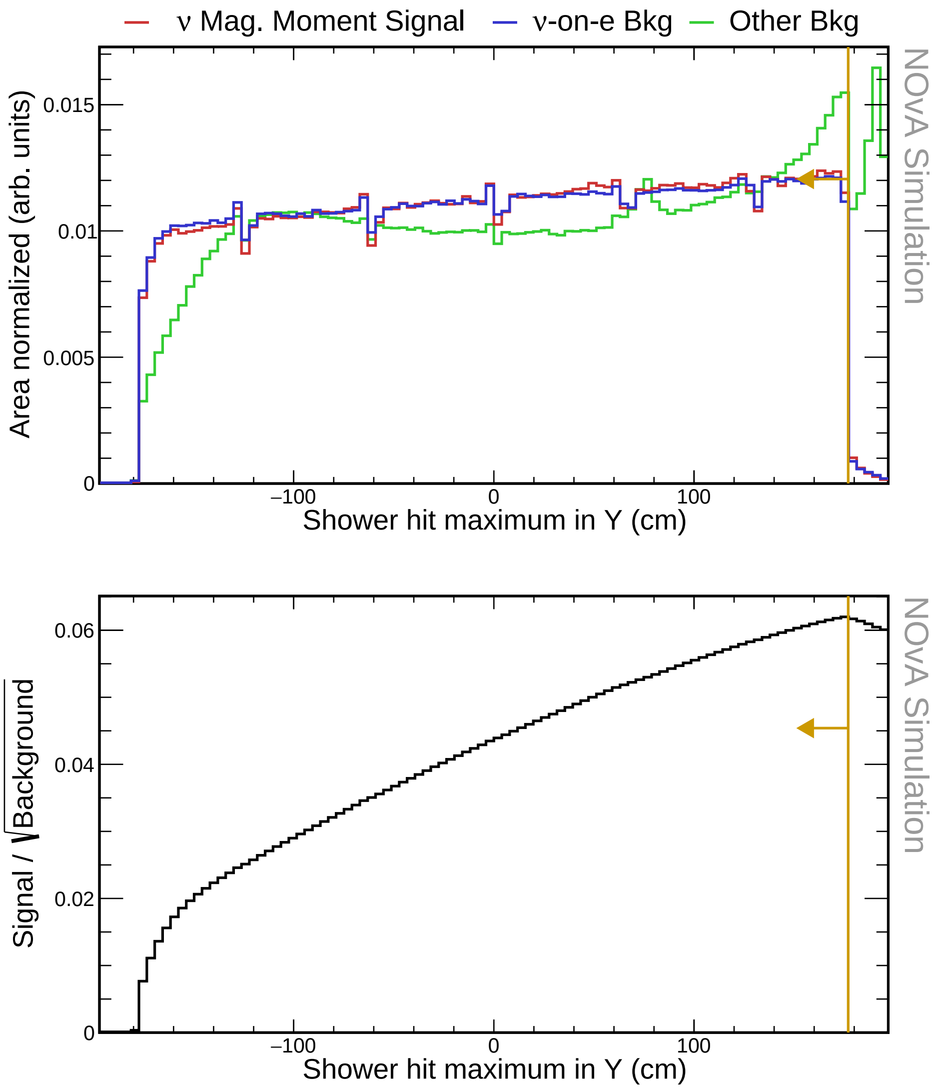

Figure 2.18: Top: Relative comparison of signal (red), ν-on-e background (blue), and other background (green) events in the distribution of the maximum hit position of the most energetic prong along the y axis. All histograms are area-normalized. Bottom: Cumulative FOM calculated as the number of signal events, divided by the number of background events from that bin until the end of the plot in the direction of the yellow arrow. The reconstruction quality, pre-selection and fiducial cuts were applied prior to making these plots. Yellow lines show the cut values that create the containment volume, with arrows pointing towards the preserved events.

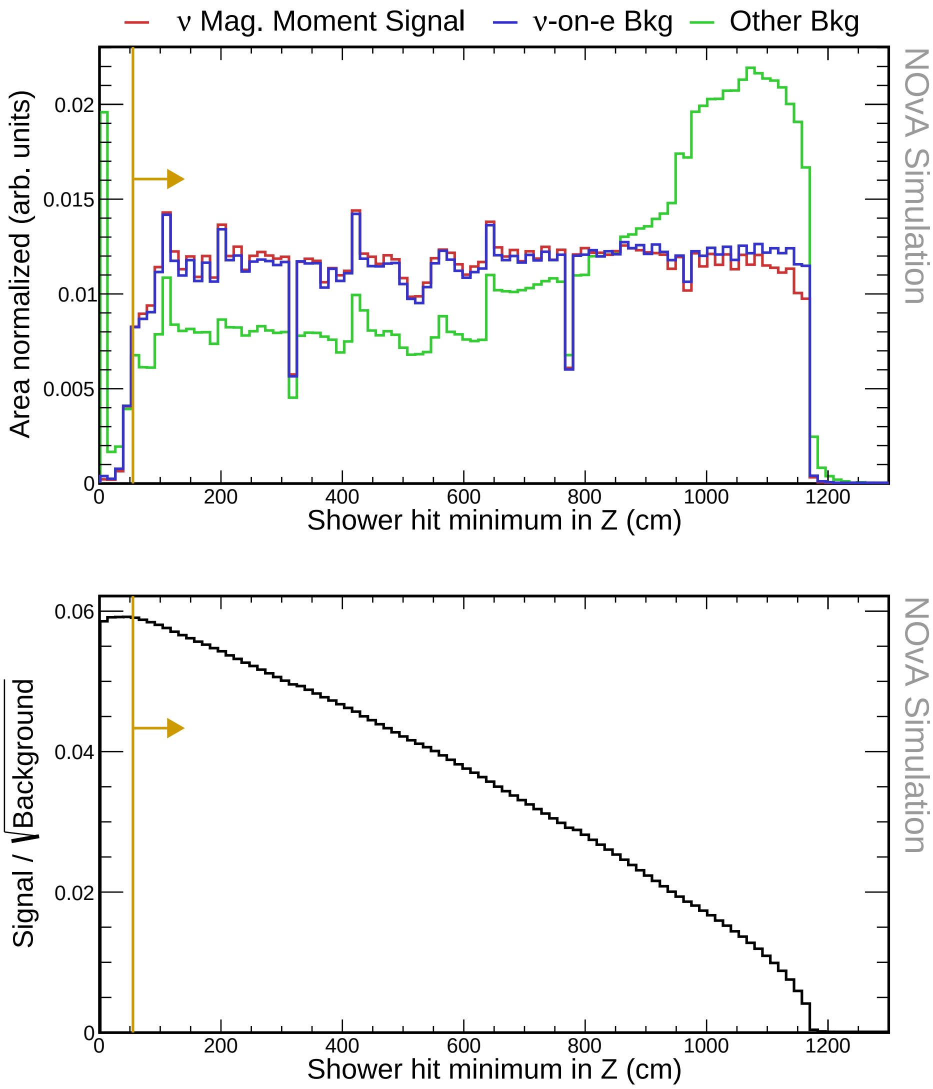

Figure 2.19: Top: Relative comparison of signal (red), ν-on-e background (blue), and other background (green) events in the distribution of the minimum hit position of the most energetic prong along the z axis. All histograms are area-normalized. Bottom: Cumulative FOM calculated as the number of signal events, divided by the number of background events from that bin until the end of the plot in the direction of the yellow arrow. The reconstruction quality, pre-selection and fiducial cuts were applied prior to making these plots. Yellow lines show the cut values that create the containment volume, with arrows pointing towards the preserved events.

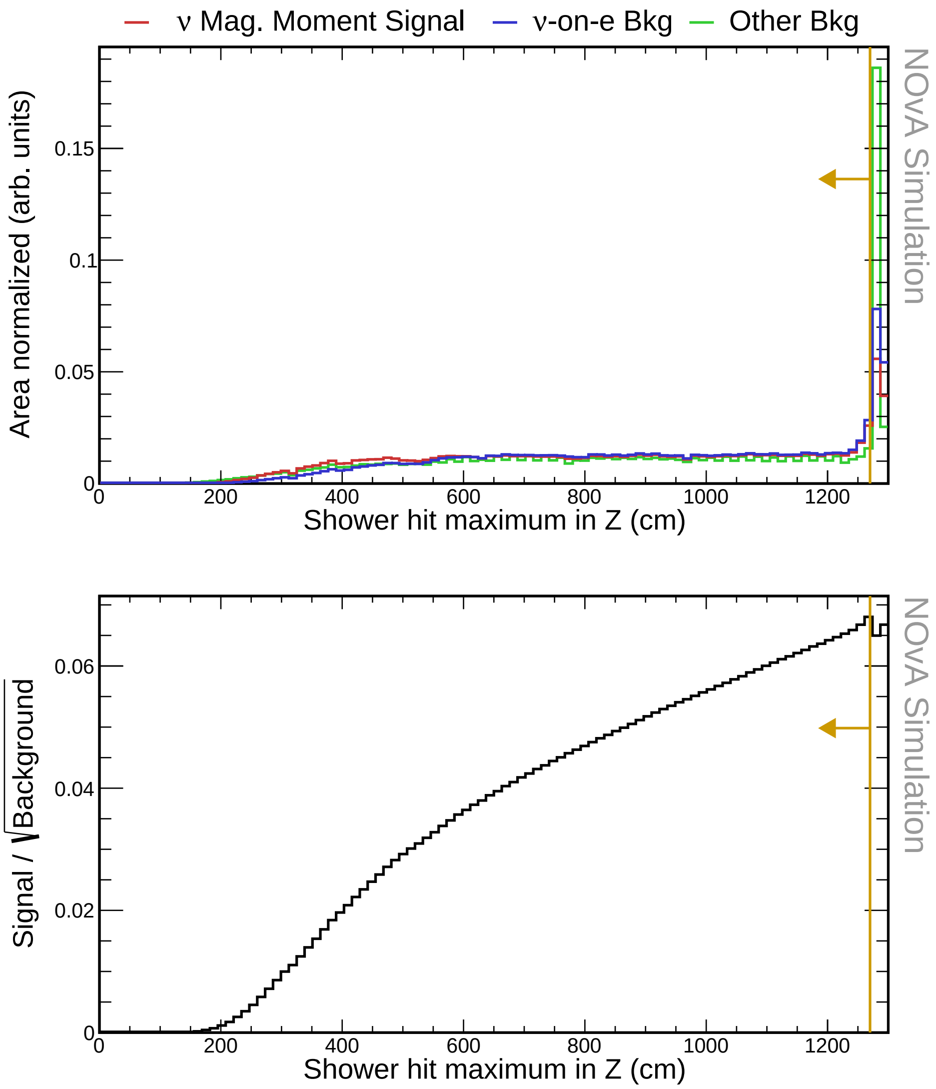

Figure 2.20: Top: Relative comparison of signal (red), ν-on-e background (blue), and other background (green) events in the distribution of the maximum hit position of the most energetic prong along the z axis. All histograms are area-normalized. Bottom: Cumulative FOM calculated as the number of signal events, divided by the number of background events from that bin until the end of the plot in the direction of the yellow arrow. The reconstruction quality, pre-selection and fiducial cuts were applied prior to making these plots. Yellow lines show the cut values that create the containment volume, with arrows pointing towards the preserved events.

For this purpose, we utilised ROOT's [122] Tool for MVA (TMVA) [123]. Specifically, we employed the rectangular cut optimisation method, which uses multivariate parameter fitters to maximise background rejection across the full range of signal efficiencies. We used the MC sampling fitting method, assuming that for each input variable, there is a single cut value (maximum or minimum) that optimally discriminates between signal and background.

TMVA generally performs better with a limited number of input variables that have strong discriminating power. Therefore, we investigated several input variables and selected only those that achieved significant background rejection. There are additional variables not mentioned here that might achieve better final results, providing opportunities for future re-analyses. Additionally, we do not apply any transformations to the input variables prior to optimisation, which might also improve the final result after dedicated study.

The variables considered include those already used in the pre-selection: the total number of hits for all prongs in slice, the length of the longest prong, and $E\theta^2$, as discussed in Sec. 2.3.3. During the TMVA optimisation, we found that the length of the longest prong did not significantly enhance discriminating power and thus removed it from the set of input variables. Additionally, we included the reconstructed energy of the most energetic shower, as used for reconstruction quality selection in Sec. 2.3.2, intending to restrict events with higher energies, since our signal is concentrated at low electron recoil energies.

Additionally, we considered all the variables used for the NOvA ν-on-e analysis for the neutrino flux constraint [103]. The first is the fraction of the reconstructed

Table 2.5: Event selection cutflow table for the containment cuts showing the number of events and the relative efficiency of each cut for each signal sample. The relative efficiency is calculated as number of events remaining after applying the corresponding cut divided by number of event for all the previous cuts. All the cuts are listed in sequence as they are applied. The top row corresponds to the sample after applying the reconstruction quality and pre-selection cuts.

Selection	**Signal**		**ν-on-e bkg**		**Other bkg**	
	N_{evt}	ϵ_{rel} (%)	N_{evt}	ϵ_{rel} (%)	N_{evt}	ϵ_{rel} (%)
Pre-selection	155.14	100	3.33×10^3	100	8.83×10^6	100
Fiducial	143.02	92.19	2.88×10^3	85.60	5.96×10^6	67.57
Containment	117.41	82.09	2.08×10^3	72.12	1.10×10^6	18.38

energy of the most energetic shower (E_{Shower}) to the total energy of all the reconstructed prongs in the entire slice (E_{Tot}). This variable distinguished our signal events, which only have a single shower, from events with multiple showers or additional activity. The second is the gap between the vertex and the most energetic shower, which can distinguish between electron and π^0 events, as the latter should have a characteristic gap several cells long. Additionally, we examined the amount of energy contained within ± 8 planes away from the vertex, besides the energy associated with the most energetic prong, which should distinguish the purely leptonic signal from backgrounds with significant hadronic activity. However, the gap and the vertex energy variables underperformed compared to others and were ultimately not used within the TMVA.

We also utilised two CNN-based event classifiers developed for the NOvA ν-on-e analysis for the neutrino flux constraint [103, 104]. These classifiers are specifically designed to identify ν-on-e interactions. The first, named ν-on-eID, is trained to select ν-on-e events from the primary ν_μCC background, while the second, named $E\pi^0$ID, is trained on events passing the ν-on-eID selection to reject the remaining background with a π^0. These classifiers use a pixel map of the entire slice as input and are designed with the same CNN architecture as ProngCVN and EventCVN described in Sec. 1.5.

The result of the TMVA is a set of cuts on each of the input variables that maximises the FOM. The input variables and the cuts that were selected for them are shown in Fig. 2.21, 2.22, and 2.23. The effect of these cuts is summarised in Tab. 2.6. Applying the TMVA cuts reduces the signal by $51.62\,\%$, the ν-on-e background by $75.03\,\%$ and other background by $99.98\,\%$. The specific values of the cuts resulting from the TMVA are

$$E_{Shower}/E_{Tot} > 0.91, \tag{2.46}$$

$$\text{Total N}^o \text{ hits for all prongs} < 116, \tag{2.47}$$

$$E_{Shower} < 1.4\,\text{GeV}, \tag{2.48}$$

$$E\theta^2 < 0.0048\,\text{GeV} \times \text{rad}^2, \tag{2.49}$$

$$\nu - on - e\text{ID} > 0.65, \tag{2.50}$$

$$E\pi^0\text{ID} > 0.63. \tag{2.51}$$

Table 2.6: Event selection cutflow table for the results of the cut-based Multivariate analysis, showing the number of events and the relative efficiency of each cut for each signal sample. The relative efficiency is calculated as number of events remaining after applying the corresponding cut divided by number of event for all the previous cuts. All the cuts are listed in sequence as they are applied. The top row corresponds to the sample after applying the reconstruction quality, pre-selection, fiducial and containment cuts.

Selection	**Signal**		**ν-on-e bkg**		**Other bkg**	
	N_{evt}	ϵ_{rel} (%)	N_{evt}	ϵ_{rel} (%)	N_{evt}	ϵ_{rel} (%)
Contained	117.41	100	2.08×10^3	100	1.10×10^6	100
E_{Shower}/E_{Tot}	113.03	96.28	2.02×10^3	97.32	4.53×10^5	41.30
N^o Hits	106.48	94.20	1.45×10^3	71.53	4.02×10^5	88.78
High E_{Shower}	85.51	80.31	777.91	53.76	3.01×10^5	74.84
ν**-on-e ID**	72.23	84.47	652.32	83.86	4.40×10^3	1.46
$E\pi^0$ **ID**	67.35	93.24	608.19	93.23	2.83×10^3	64.34
$E\theta^2$	56.80	84.33	519.09	85.35	181.24	6.40

After the full event selection, the predicted number of signal events for $\mu_\nu = 10^{-9}\mu_B$ is 56.80, and the total number of background events under the SM hypothesis is 700.33. This results in

$$\text{Signal Purity} = \frac{\text{Signal}}{\text{Signal+Background}} = 7.50\,\%, \tag{2.52}$$

$$\text{Signal Efficiency} = \frac{\text{Signal}}{\text{Signal}_{\text{No Cut}}} = 6.95\,\%. \tag{2.53}$$

Also,

$$\frac{\text{Signal}}{\sqrt{\text{Background}}} = 2.15 \tag{2.54}$$

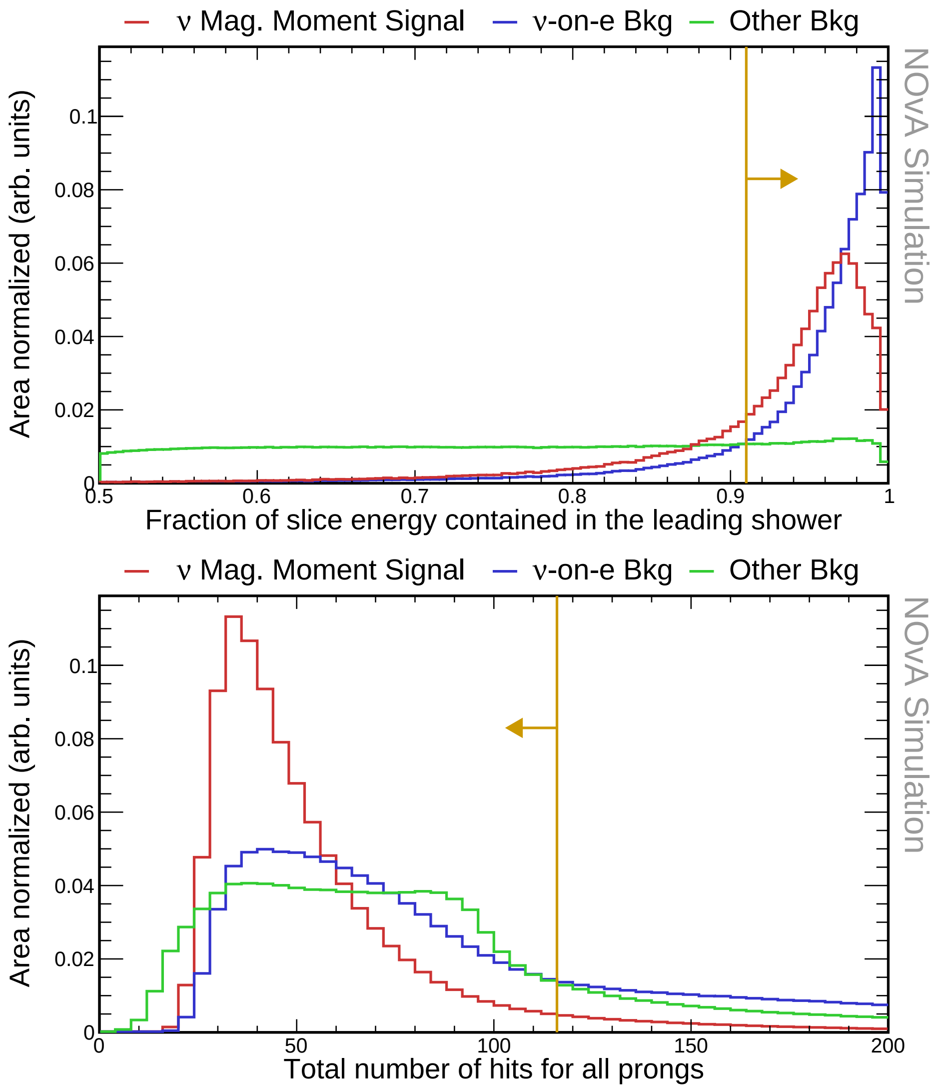

Figure 2.21: Relative comparison of signal (red), ν-on-e background (blue), and other background (green) events in the distribution of the fraction of the total energy contained in the primary shower (top) and of the total number of hits in the slice (bottom). All histograms are area-normalized. The reconstruction quality, pre-selection, fiducial and containment cuts were applied prior to making these plots. Yellow lines show the cut values on the depicted variables, with arrows pointing towards the preserved events.

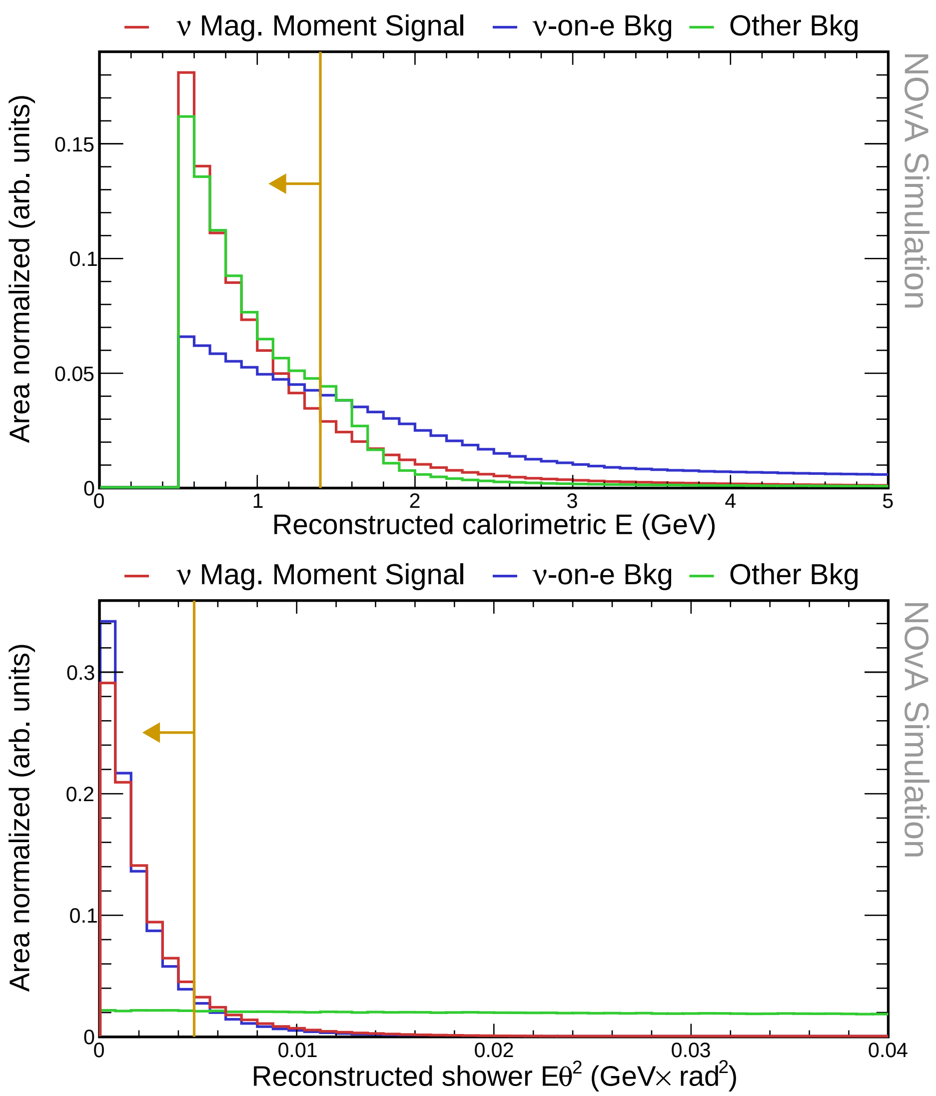

Figure 2.22: Relative comparison of signal (red), ν-on-e background (blue), and other background (green) events in the distribution of the reconstructed energy of the primary shower (top) and of the reconstructed energy multiplied by the angle from the incoming neutrino beam direction squared.(bottom). All histograms are area-normalized. The reconstruction quality, pre-selection, fiducial and containment cuts were applied prior to making these plots. Yellow lines show the cut values on the depicted variables, with arrows pointing towards the preserved events.

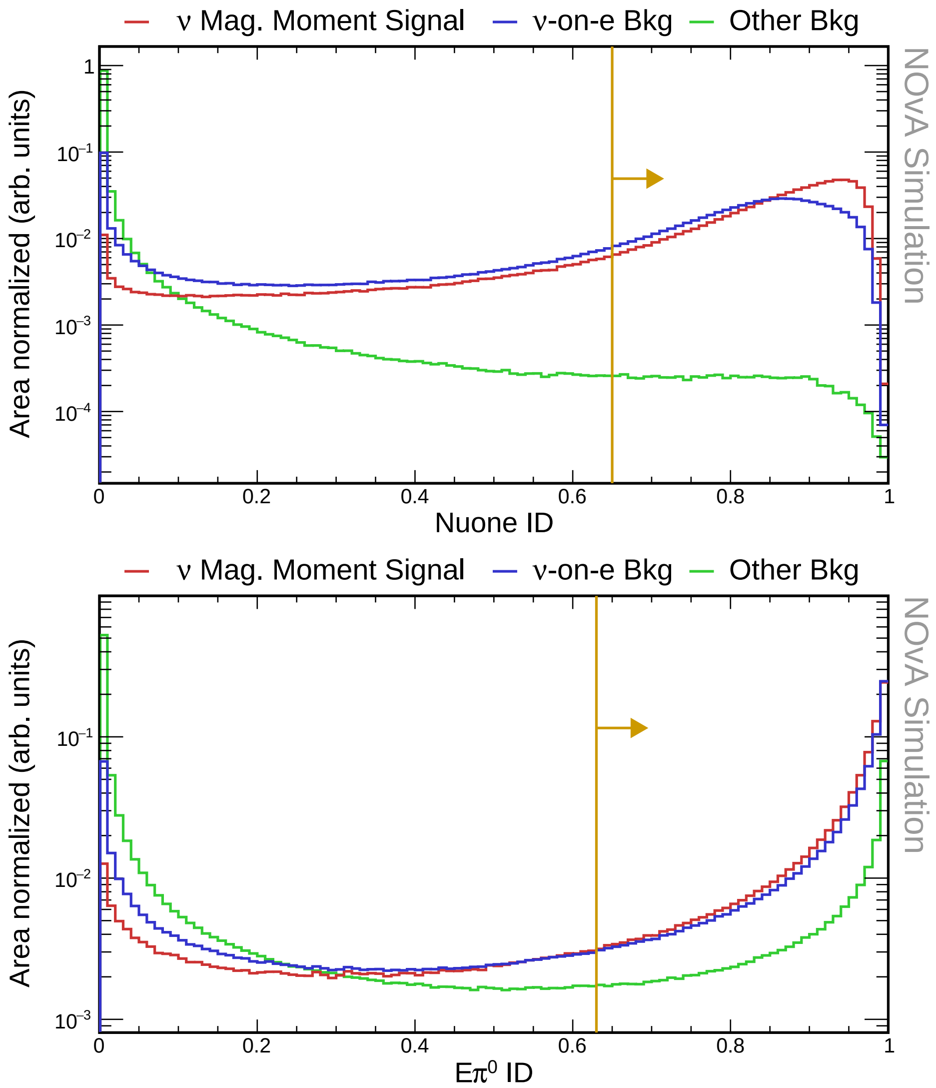

Figure 2.23: Relative comparison of signal (red), ν-on-e background (blue), and other background (green) events in the distribution of the NuoneID (top) and EPi0ID (bottom) event identifiers. All histograms are area-normalized and logarithmic in the y axis. The reconstruction quality, pre-selection, fiducial and containment cuts were applied prior to making these plots. Yellow lines show the cut values on the depicted variables, with arrows pointing towards the preserved events.

and

$$\text{FOM} = \frac{\text{Signal}}{\sqrt{\text{Signal+Background}}} = 2.06. \tag{2.55}$$

2.4 Systematic Uncertainties

We consider all the standard NOvA systematic uncertainties described in Sec. 1.8, grouped into four categories: neutrino flux, detector calibration, detector modelling, and neutrino cross section systematic uncertainties. Summary of the effect of both systematic and statistical uncertainties on the predicted number of SM background events is depicted in Fig. 2.24. The four categories of systematic uncertainties are assumed to be uncorrelated between each other, allowing to calculate their combined effect by summing their individual contribution in quadrature. The total prediction of the number of SM background events can be expressed as

$$N_{SM} = 700.33 \pm 26.46\,(\text{stat.})^{+72.48}_{-62.99}\,(\text{syst.})\,. \tag{2.56}$$

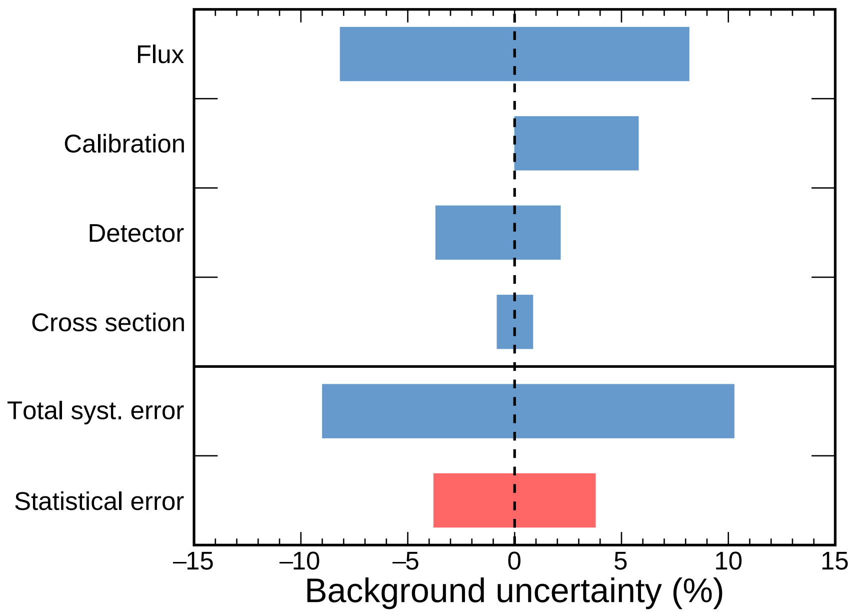

Figure 2.24: Relative effect of systematic and statistical uncertainties on the number of SM background events. The total systematic uncertainty (blue bottom bar) is calculated as a square root of the sum of squares of the four categories of systematic uncertainties, shown ordered by the size of their effect. These are the neutrino flux, detector calibration, detector modelling, and neutrino cross section systematic uncertainties.

To assess the effect of the neutrino flux systematic uncertainty, we use 8 ND-only principal components. Figure 2.25 shows their combined effect on the predicted SM background as a function of the primary shower's (electron for true ν-on-e events) reconstructed energy. Since the principal components are uncorrelated by construction, the total systematic uncertainty for each bin is calculated by adding the effect of all the principal components in quadrature. The effect of the neutrino flux systematic uncertainty does not depend on the primary shower's calorimetric energy and altering the neutrino flux prediction can be represented by a normalization shift. The final effect of the neutrino flux systematic uncertainty on the total number of SM background events is $\pm 8.16\,\%$ and is symmetric around the nominal prediction.

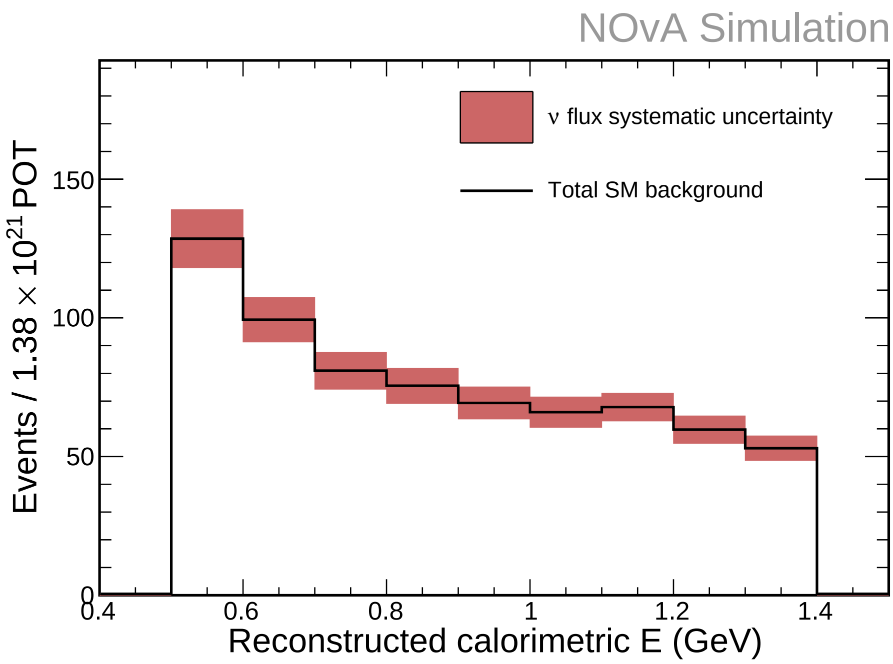

Figure 2.25: Effect of the total neutrino flux systematic uncertainty on the primary shower energy distribution of the SM background events.

The effect of the total detector systematic uncertainty, together with the calibration systematic uncertainties, is $^{+6.17\,\%}_{-3.69\,\%}$. This uncertainty is highly energy dependent, as can be seen in Fig. 2.26, and can significantly alter the shape of the energy distribution. The detector and calibration systematic uncertainties were combined due to their similar effect and origin. The largest systematic uncertainty in this group is the absolute energy scale uncertainty, which has a one-sided effect for our analysis and size $+5.72\,\%$. Therefore, both the positive and the negative shift change the total number of events in the same direction. This is followed by the light level systematic uncertainty, which is $1.13\,\% - 3.39\,\%$, and the Cherenkov systematic uncertainty, which is $1.82\,\% - 1.46\,\%$. The detector ageing and calibration shape systematic uncertainties are by default only one sided and their effect on the SM background is $+0.55\,\%$ and $+0.69\,\%$.

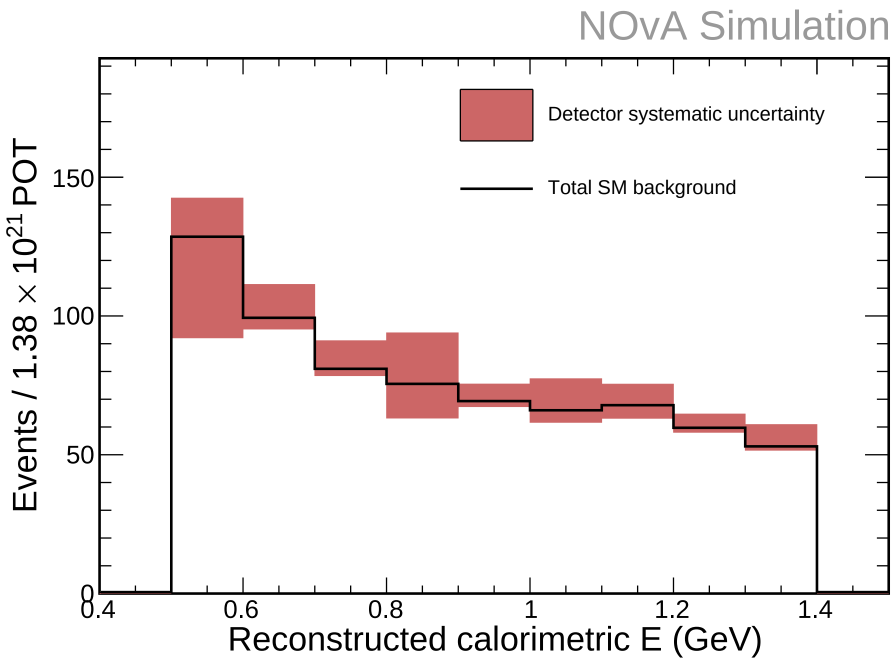

Figure 2.26: Effect of the total detector systematic uncertainty on the primary shower energy distribution of the SM background. The detector uncertainty consists of the absolute calibration, calibration shape, detector ageing, light level, and Cherenkov systematic uncertainties.

We assume that the ν-on-e interactions are known precisely in the predictions, therefore the dominant ν-on-e component of the SM background has no systematic uncertainty from neutrino interaction prediction. Therefore, the total cross section uncertainty on the SM background is very small and has a value of $^{+1.54\,\%}_{-1.49\,\%}$. The most dominant neutrino interaction systematic uncertainties are from the axial and vector masses of the NCRes interaction ($^{+0.97\,\%}_{-0.90\,\%}$ for axial and $^{+0.41\,\%}_{-0.35\,\%}$ for vector mass). Also significant is the effect of the coherent NC scaling ($^{+0.85\,\%}_{-0.85\,\%}$), of the QE normalization factor ($^{+0.31\,\%}_{-0.24\,\%}$), or of the mean free path of pions before they undergo an interaction ($^{+0.30\,\%}_{-0.43\,\%}$). Other uncertainties have only a very small impact. The ones that have an effect of ($> \pm 0.1\,\%$) are the suppression of long-range nuclear effect and Res events at low energy transfers, shape of the MEC tuning dependent on the neutrino energy, single π NCDIS production, distance parton travels before hadronization, axial mass of NC elastic and CCRes interactions, branching ratios of radiative and η-resonance decays, or the π angular distribution in the Δ resonance decays.

2.5 Results

The final distribution of the predicted SM background, the signal for $\mu_\nu = 10^{-9}\mu_B$ and the measured data in the primary shower reconstructed calorimetric energy is shown in Fig. 2.27. We do not use the energy distribution of events, but we are using this distribution to cross check the validity of our analysis. It appears that everything is grand. The data appears to be within the systematic and statistical uncertainty for all the displayed bins. The only exception is the bin within $(0.9\,\mathrm{GeV}, 1.0\,\mathrm{GeV})$, which is however still within two standard variations from the accepted values and therefore can be safely ignored.

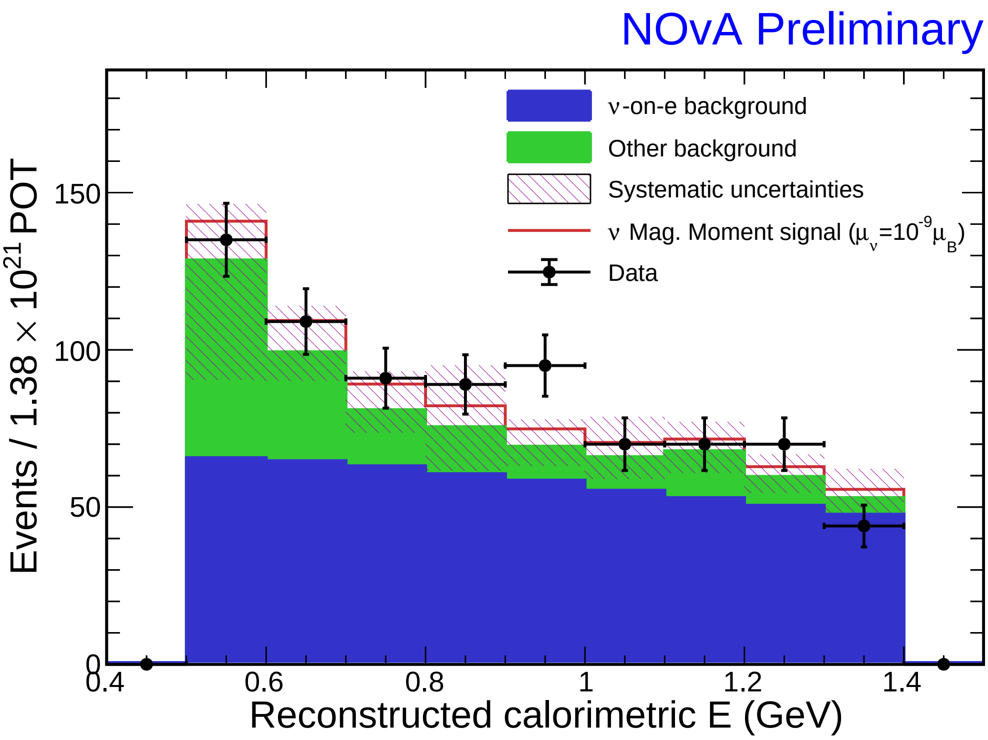

Figure 2.27: comparison of the prediction to the observed data.

The total number of observed events passing our selection is

$$N_{Observed} = 177. \tag{2.57}$$

The total number of predicted events for the SM background (without neutrino magnetic moment) is

$$N_{Predicted} = 700.33 \pm 26.46\,(\text{stat.})^{+72.48}_{-62.99}\,(\text{syst.}) \tag{2.58}$$

If the neutrino magnetic moment is $\mu_\nu = 10^{-9}\mu_B$, there would be 56.80 additional observed events.

2.5.1 Hypothesis Testing

We are testing the validity of the null hypothesis, which is in our case that there is no neutrino magnetic moment and therefore all the observed events are purely due to the SM processes.

Write out the total number of measured events and their corresponding uncertainties

Explain what are the results of the fit and the limits, discuss the statistical significance of the result

We are basically doing two separate things:

1. Testing a hypothesis that there is no magnetic moment present in the signal. Can we reject the null hypothesis given our data?

2. If we can reject the null hypothesis we want to estimate the best fit of the parameter. Additionally, we want to put a limit (set a confidence interval) on the magnetic moment parameter.

What should be included here:

- Fit methodology: Detail the fitting techniques used to extract the muon neutrino magnetic moment from the data.

- Fit validation: Describe how the fit is validated, including any statistical tests used.

Error on the best fit point - how to calculate? [NOvAResultsNuOnly2018.pdf] TABLE VI. Sources of uncertainty and their estimated average impact on the oscillation parameters in the joint fit. This impact is quantified using the increase in the one-dimensional 68% C.L. interval, relative to the size of the interval when only statistical uncertainty is included in the fit.

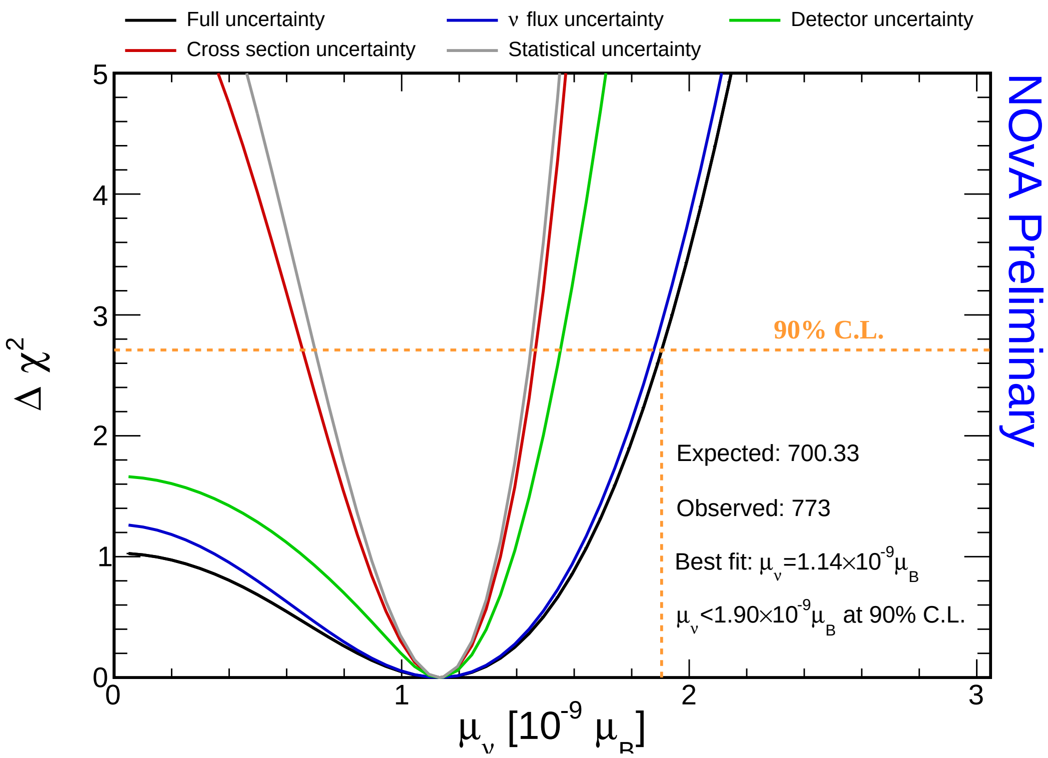

Figure 2.28: Results of the fit of the prediction to the observed data, with the neutrino magnetic moment as the sole fit parameter. We are profiling over the full range of systematic uncertainties.

Nitish's thesis: pg 156: As mentioned before, the nuisance parameters in the likelihood fit are derived by interpolating between shifts at given numerical sigma values for the above uncertainties for each analysis bin. One can then evaluate the size of the uncertainties in many ways. For the appearance channel, one can compare different systematics based on the effect it has on the total number of predicted signal and background events when varied by $\pm 1\sigma$, as shown in Fig. 4.12. One can also estimate its effect by fitting to Asimov data using the central value prediction and varying the MC expectation based on the systematic variation. This takes the form of the effect of the systematic on the individual oscillation parameters [79], as shown in Figs. 4.13 and 4.14. All of these metrics show that the analysis is statistically limited, i.e the systematic error is smaller than the statistical error in the prediction. - I think this basically mean, that I should use the best fit point in the fit˙bestFitPoint.C script and see what I get? Like the syst pulls?

Maximum likelihood with binned data:

READ NITISH NAYAK'S THESIS PAGE 132! [79]

N bins with a vector of data $n = (n1, ..., n_N)$ with expectation values $\mu = E[n]$

and probabilities $f(n;\mu)$. Suppose the mean values μ can be determined as a function of a set of parameters θ (I assume for us there's either only one parameter - magnetic moment, or three parameters - mag. moment, scale of SM signal and scale of SM background). Then one may maximize the likelihood function based on the contents of the bins.

If the n_i is regarded as independent and Poisson distributed (which I'd say is the case for us), then the data are instead described by a product of Poisson probabilities,

$$f_p(n;\theta) = \prod_{i=1}^{N} \frac{\mu_i^{n_i}}{n_i!} e^{-\mu_i}, \tag{2.59}$$

where the mean values μ_i are given functions of θ. The total number of events n_{tot} thus follows a Poisson distribution with mean $\mu_{tot} = \sum_i \mu_i$.

When using maximum likelihood with binned data, one can find the maximum likelihood estimators and at the same time obtain a statistic usable for a test of goodness-of-fit. Maximizing the likelihood $L(\theta) = f_P(n;\theta)$ is equivalent to maximizing the likelihood ratio $\lambda(\theta) = f_P(n;\theta)/f(n;\hat{\mu})$, where in the denominator $f(n;\hat{\mu})$ is a model with an adjustable parameter for each bin, $\mu = (\mu_1, ..., \mu_N)$, and the corresponding estimators are $\hat{\mu} = (n_1, ..., n_N)$ (called the 'saturated model').

Equivalently one often minimizes the quantity $-2\ln\lambda(\theta)$. For independent Poisson distributed n_i this is

$$-2\ln\lambda(\theta) = 2\sum_{i=1}^{N}\left[\mu_i(\theta) - n_i + n_i \ln\frac{n_i}{\mu_i(\theta)}\right], \tag{2.60}$$

where for bins with $n_i = 0$, the last term is zero. In our term $\mu_i(\theta)$ is the **expected number of events in bin i if magnetic moment is** θ and n_i is the observed (measured) number of events in that bin.

A smaller value of $-2\ln\lambda\left(\hat{\theta}\right)$ corresponds to better agreement between the data and the hypothesized form of $\mu(\theta)$. The value of $-2\ln\lambda\left(\hat{\theta}\right)$ can thus be translated into a **p-value as a measure of goodness-of-fit**. Assuming the model is correct, then according to **Wilk's theorem**, for **sufficiently large** μ_i and provided certain regularity conditions are met, **the minimum of** $-2\ln\lambda$ **follows a** χ^2 **distribution.** If there are N bins and M fitter parameters, then the number of degrees of freedom for the χ^2 distribution is $N - M$ if the data are threated as Poisson distributed - which they are for us.

The method of least squares coincides with the method of maximum likelihood in a special case where the independent variables are Gaussian distributed - so I suppose this means that if I have enough events in each single bin, then I could equate the method of log likelihood and the method of least squares...

2.5.2 Nuisance Parameters

In general the model is not perfect, which is to say it cannot provide an accurate description of the data even at the most optimal point of its parameter space. As a result, the estimated parameters can have a systematic bias. One can improve the model by including in it additional parameters. That is, $P(x|\theta)$ is replaced by a more general model $P(x|\theta,\nu)$, which depends on parameters of interest θ and *nuisance parameters* ν. The additional parameters are not of intrinsic interest but must be included for the model to be sufficiently accurate for some point in the enlarged parameter space.

Although including additional parameters may eliminate or at least reduce the effect of systematic uncertainties, their presence will result in increased statistical uncertainties for the parameters of interest. This occurs because the estimators for the nuisance parameters and those of interest will in general be correlated, which results in an enlargement of the contour.

To reduce the impact of the nuisance parameters one often tries to constrain their values by means of control or calibration measurements, say, having data **y** (I assume for us this would represent a control sample - like they use in the ND group). For example, some components of y could represent estimates of the nuisance parameters, often from separate experiments. Suppose the measurements y are statistically independent from x and are described by a model $P(y|\nu)$. The joint model for both x and y is in this case therefore the product of the probabilities for x and y, and thus the likelihood function for the full set of parameters is

$$L(\theta,\nu) = P(x|\theta,\nu)\, P(y|\nu)\,. \tag{2.61}$$

Note that in this case if one wants to simulate the experiment by means of Monte

Carlo, both the primary and control measurements, x and y, must be generated for each repetition under assumption of fixed values for the parameters θ and ν.

Using all of the parameters (θ, ν) to find the statistical errors in the parameters of interest θ is equivalent to using the *profile likelihood*, which depends only on θ. It is defined as

$$L_p(\theta) = L(\theta, \hat{\nu}(\theta)), \tag{2.62}$$

This equation is supposed to have double hat for the neutrino on RHS but that throws an error when compiling... where the double-hat notation indicates the profiled values of the parameters ν, defined as values that maximize L for the specified θ.

2.5.3 Unbinned Parameter Estimation

If the total number of data values is small, the unbinned maximum likelihood method is preferred, since binning can only result in a loss of information, and hence the larger statistical errors for the parameter estimates. Does't this mean that if the number of events for the neutrino magnetic moment analysis is small, it would be better to do a completely unbinned maximum likelihood method, instead of a single bin method?

2.6 Discussion

What should be included here:

- Interpretation: Interpret the results in the context of the current understanding of neutrino physics.
- Implications: Explain the broader implications of your findings for the field of particle physics.
- Future work: Suggest directions for future research based on your results.
  - Improvements in NOvA, more FHC data, including RHC data, better reconstruction, better simulation and calibration, better event selection, including sideband samples, more systematics studies, better fitting techniques...
  - Future beyond NOvA - DUNE

* What are the possibilities for DUNE?

2.7 Summary

Summarize the results and compare them to the introduction, including comparisons to other experiments and theory. Restate the significant of the measurement

Closing remarks

Acronyms

ν-on-e neutrino-on-electron (interaction). 26, 27, 29, 33–42, 44–52, 54–68, 70, 71

2p2h two particle - two hole. 10

ADC Analog-to-Digital Converter. 7, 14, 17, 18

APD Avalanche Photodiode. 5–7, 10, 17, 18, 46

ASIC Application-Specific Integrated Circuit. 7

BDT Boosted Decision Tree. 14

BPF Break Point Fitter. 12

BSM Beyond Standard Model. 26–28, 30, 31

C.L. Confidence Level. 26, 27

CC Charged Current. 10, 11, 24, 35, 41, 42, 49, 51, 64, 71

CMC Comprehensive Model Configuration. 10

CNN Convolutional Neural Network. 13, 64

COHπ Coherent π (production). 10, 24

CP Charge conjugation - Parity (symmetry). 1

CRY Cosmic-Ray Shower Generator. 10, 14

CVN Convolutional Visual Network. 13, 44, 47

DAQ Data Acquisition. 7, 11, 16

DCM Data Concentration Module. 7, 8, 43

DIS Deep Inelastic Scattering. 10, 24, 71

DUNE Deep Underground Neutrino Experiment. 1, 9

FB Fibre Brightness. 17, 18

FD Far Detector. 3–7, 10, 11, 17–19, 23

FEB Front End Board. 6–8, 17, 46

Fermilab Fermi National Accelerator Laboratory. 1, 3, 9

FHC Forward Horn Current (neutrino mode). 2, 3

FOM Figure Of Merit. 43, 51, 53–62, 64, 69

FPGA Field Programmable Gate Array. 7

FSI Final State Interaction. 10, 24

LDM Light Dark Matter. 27

LOWESS Locally Weighted Scatter plot Smoothing. 19, 20

MC Monte Carlo. 8–10, 14, 39, 63

MEC Meson Exchange Current. 10, 24, 41, 42, 71

MEU Muon Energy Unit. 21

MI Main Injector. 1, 2, 9

MIP Minimum Ionising Particle. 14, 18, 21

MIPP Main Injector Particle Production (experiment). 9

ML Machine Learning. 13, 14, 44

MVA Multi Variate Analysis. 42, 51, 63, 82

NC Neutral Current. 11, 14, 71

ND Near Detector. 1, 3–5, 7, 11, 12, 22–24, 26, 27, 29, 32, 39, 42, 47, 51, 70

NDOS Near Detector on the Surface. 3

NOvA NuMI Off-axis ν_e Appearance (experiment). 1, 3–14, 16–20, 22–24, 26, 27, 29, 32, 34, 36–39, 41, 42, 44, 47, 49, 63, 64, 69

NP New Physics. 31

NuMI Neutrinos from the Main Injector. 1–3, 8, 9, 11, 53

PCA Principal Component Analysis. 23

PE Photo Electron. 6, 7, 15, 17–19

PECorr Corrected Photo Electrons. 19, 21

PID Particle Identification. 13

PMNS Pontecorvo-Maki-Nakagawa-Sakata. 30, 31

POT Protons On Target. 2, 39, 41, 43, 48

PPFX Package to Predict the Flux. 9, 23, 39

PVC Polyvinyl chloride. 4–6, 22

QE Quasi Elastic (interaction). 10, 24, 71

ReMId Reconstructed Muon Identifier. 14

Res Resonant baryon production. 10, 24, 71

RHC Reverse Horn Current (antineutrino mode). 2, 3

SM Standard Model. 26, 28–31, 35–40, 43, 65, 69–73

TMVA Tool for MVA. 63–65

WLS Wavelength Shifting (fibre). 5, 6, 10, 14, 16, 19, 21

Bibliography

[1] Nova experiments official website. URL https://novaexperiment.fnal.gov. Cited February 2024.

[2] Fermi national accelerator laboratory official website. URL https://fnal.gov. Cited February 2024.

[3] Gary Feldman for the NOvA Collaboration. Physics of the nova experiment. White paper, 2012. URL https://nova-docdb.fnal.gov/cgi-bin/ShowDocument?docid=7733. Public NOvA document: NOVA-doc-7733-v1, cited on 05.2020.

[4] R.B. Patterson. The NOvA Experiment: Status and Outlook. *Nucl. Phys. B Proc. Suppl.*, 235-236:151–157, 2013. doi:10.1016/j.nuclphysbps.2013.04.005.

[5] P. Adamson et al. First measurement of muon-neutrino disappearance in NOvA. *Phys. Rev. D*, 93(5):051104, 2016. doi:10.1103/PhysRevD.93.051104.

[6] M.A. Acero et al. First Measurement of Neutrino Oscillation Parameters using Neutrinos and Antineutrinos by NOvA. *Phys. Rev. Lett.*, 123(15):151803, 2019. doi:10.1103/PhysRevLett.123.151803.

[7] M. A. Acero et al. Improved measurement of neutrino oscillation parameters by the NOvA experiment. *Phys. Rev. D*, 106(3):032004, 2022. doi:10.1103/PhysRevD.106.032004.

[8] M. A. Acero et al. Measurement of neutrino-induced neutral-current coherent π^0 production in the NOvA near detector. *Phys. Rev. D*, 102(1):012004, 2020. doi:10.1103/PhysRevD.102.012004.

[9] M. A. Acero et al. Measurement of the double-differential muon-neutrino charged-current inclusive cross section in the NOvA near detector. *Phys. Rev. D*, 107(5):052011, 2023. doi:10.1103/PhysRevD.107.052011.

[10] M. A. Acero et al. Measurement of the ν_e-Nucleus Charged-Current Double-Differential Cross Section at $\langle E_\nu \rangle = 2.4$ GeV using NOvA. *Phys. Rev. Lett.*, 130 (5):051802, 2023. doi:10.1103/PhysRevLett.130.051802.

[11] M. A. Acero et al. Measurement of ν_μ charged-current inclusive π^0 production in the NOvA near detector. *Phys. Rev. D*, 107(11):112008, 2023. doi:10.1103/PhysRevD.107.112008.

[12] P. Adamson et al. Search for active-sterile neutrino mixing using neutral-current interactions in NOvA. *Phys. Rev. D*, 96(7):072006, 2017. doi:10.1103/PhysRevD.96.072006.

[13] M. A. Acero et al. Search for Active-Sterile Antineutrino Mixing Using Neutral-Current Interactions with the NOvA Experiment. *Phys. Rev. Lett.*, 127(20): 201801, 2021. doi:10.1103/PhysRevLett.127.201801.

[14] M. A. Acero et al. Supernova neutrino detection in NOvA. *JCAP*, 10:014, 2020. doi:10.1088/1475-7516/2020/10/014.

[15] M. A. Acero et al. Extended search for supernovalike neutrinos in NOvA coincident with LIGO/Virgo detections. *Phys. Rev. D*, 104(6):063024, 2021. doi:10.1103/PhysRevD.104.063024.

[16] M. A. Acero et al. Search for slow magnetic monopoles with the NOvA detector on the surface. *Phys. Rev. D*, 103(1):012007, 2021. doi:10.1103/PhysRevD.103.012007.

[17] Peter N. Shanahan and Patricia LaVern Vahle. Physics with NOvA: a half-time review. *Eur. Phys. J. ST*, 230(24):4259–4273, 2021. doi:10.1140/epjs/s11734-021-00285-9.

[18] Peter Shanahan and Patricia Vahle. The NOvA Physics Program through 2025. Snowmass 2021 Letters of Interest NF, 135. URL https://www.snowmass21.org/docs/files/summaries/NF/SNOWMASS21-NF1_NF3_Patricia_Vahle-145.pdf.

[19] P. Adamson et al. The NuMI Neutrino Beam. *Nucl. Instrum. Meth. A*, 806:279–306, 2016. doi:10.1016/j.nima.2015.08.063.

[20] Records. URL https://operations.fnal.gov/records/. Performance records achieved by the Fermilab accelerators. Cited May 2024.

[21] Katsuya Yonehara. Megawatt upgrade of numi target system. 1 2022. URL https://www.osti.gov/biblio/1844332.

[22] Leonidas Aliaga Soplin. *Neutrino Flux Prediction for the NuMI Beamline.* PhD thesis, William-Mary Coll., 2016.

[23] Leonidas Aliaga Soplin. 2017-2018 Beam Plots. NOVA Document 20843. URL https://nova-docdb.fnal.gov/cgi-bin/sso/ShowDocument?docid=20843. NOvA internal document.

[24] D. S. Ayres et al. The nova technical design report. *NOvA Collaboration*, 2007. doi:10.2172/935497.

[25] Yury Kudenko. Neutrino detectors for oscillation experiments. *JINST*, 12(06): C06003, 2017. doi:10.1088/1748-0221/12/06/C06003.

[26] S. Mufson et al. Liquid scintillator production for the NOvA experiment. *Nucl. Instrum. Meth. A*, 799:1–9, 2015. doi:10.1016/j.nima.2015.07.026.

[27] Alex Sousa. Density of NOvA Liquid Scintillator at 69° F. NOVA Document 11886. URL https://nova-docdb.fnal.gov/cgi-bin/sso/ShowDocument?docid=11886. NOvA internal document.

[28] M.J. Berger, J.S. Coursey, M.A. Zucker, and J. Chang. ESTAR, PSTAR, and ASTAR: Computer Programs for Calculating Stopping-Power and Range Tables for Electrons, Protons, and Helium Ions (version 1.2.3). URL http://physics.nist.gov/Star.

[29] Luke Vinton. Calorimetric Energy Scale Calibration of the NOvA Detectors. NOVA Document 13579, document FA_Calorimetric_energy_scale.pdf. URL https://nova-docdb.fnal.gov/cgi-bin/sso/ShowDocument?docid=13579. NOvA Technical Note.

[30] Xinchun Tian. NOvA Data Acquisition Software System. In *Meeting of the APS Division of Particles and Fields*, 9 2011.

[31] Joao Coelho, Barnali Chowdhury, and Ryan Murphy. Tech note: Good data selection. NOVA Document 13546. URL https://nova-docdb.fnal.gov/cgi-bin/sso/ShowDocument?docid=13546. NOvA technical note.

[32] Jonathan M. Paley. BadChannels Technical Note. NOVA Document 12771. URL https://nova-docdb.fnal.gov/cgi-bin/sso/ShowDocument?docid=12771. NOvA technical note.

[33] A. Aurisano, C. Backhouse, R. Hatcher, N. Mayer, J. Musser, R. Patterson, R. Schroeter, and A. Sousa. The NOvA simulation chain. *J. Phys. Conf. Ser.*, 664(7):072002, 2015. doi:10.1088/1742-6596/664/7/072002.

[34] S. Agostinelli et al. GEANT4–a simulation toolkit. *Nucl. Instrum. Meth. A*, 506: 250–303, 2003. doi:10.1016/S0168-9002(03)01368-8.

[35] Zarko Pavlovic. *Observation of Disappearance of Muon Neutrinos in the NuMI Beam.* PhD thesis, Texas U., 2008.

[36] L. Aliaga et al. Neutrino Flux Predictions for the NuMI Beam. *Phys. Rev. D*, 94(9):092005, 2016. doi:10.1103/PhysRevD.94.092005. [Addendum: Phys.Rev.D 95, 039903 (2017)].

[37] C. Alt et al. Inclusive production of charged pions in p+C collisions at 158-GeV/c beam momentum. *Eur. Phys. J. C*, 49:897–917, 2007. doi:10.1140/epjc/s10052-006-0165-7.

[38] Gemma Maria Tinti. *Sterile neutrino oscillations in MINOS and hadron production in pC collisions.* PhD thesis, 2010.

[39] B Baatar, G Barr, J Bartke, L Betev, O Chvala, J Dolejsi, V Eckardt, HG Fischer, Z Fodor, A Karev, et al. Inclusive production of protons, anti-protons, neutrons, deuterons and tritons in p+ c collisions at 158 gev/c beam momentum. *The European Physical Journal C*, 73:1–66, 2013. doi:10.1140/epjc/s10052-013-2364-3.

[40] D. S. Barton et al. Experimental study of the a dependence of inclusive hadron fragmentation. *Phys. Rev. D*, 27:2580–2599, Jun 1983. doi:10.1103/PhysRevD.27.2580.

[41] Andrey V. Lebedev. *Ratio of Pion Kaon Production in Proton Carbon Interactions.* PhD thesis, 2007.

[42] T.T. Böhlen, F. Cerutti, M.P.W. Chin, A. Fassò, A. Ferrari, P.G. Ortega, A. Mairani, P.R. Sala, G. Smirnov, and V. Vlachoudis. The fluka code: Developments and challenges for high energy and medical applications. *Nuclear Data Sheets*, 120:211–214. ISSN 0090-3752. doi:10.1016/j.nds.2014.07.049.

[43] Alfredo Ferrari, Paola R. Sala, Alberto Fasso, and Johannes Ranft. FLUKA: A multi-particle transport code (Program version 2005). 10 2005. doi:10.2172/877507.

[44] A. Aduszkiewicz et al. Measurements of production and inelastic cross sections for p+C , p+Be , and p+Al at 60 GeV/c and p+C and p+Be at 120 GeV/c. *Phys. Rev. D*, 100(11):112001, 2019. doi:10.1103/PhysRevD.100.112001.

[45] H. Adhikary et al. Measurements of π^+, π^-, p, $\bar{p}$, K^+ and K^- production in 120 GeV/c p + C interactions. *Phys. Rev. D*, 108:072013, 2023. doi:10.1103/PhysRevD.108.072013.

[46] H. Adhikary et al. Measurements of KS0, Λ, and Λ^- production in 120 GeV/c p+C interactions. *Phys. Rev. D*, 107(7):072004, 2023. doi:10.1103/PhysRevD.107.072004.

[47] A. Aduszkiewicz et al. Measurements of hadron production in π^+ + C and π^+ + Be interactions at 60 GeV/c. *Phys. Rev. D*, 100(11):112004, 2019. doi:10.1103/PhysRevD.100.112004.

[48] Matej Pavin. Hadron production measurements for neutrino experiments, 2020. URL https://indico.fnal.gov/event/43209/contributions/187869/attachments/130502/159028/HadronProduction_neutrino2020.pdf. Presented on Neutrino 2020 conference.

[49] T. Akaishi et al. EMPHATIC: A Proposed Experiment to Measure Hadron Scattering and Production Cross Sections for Improved Neutrino Flux Predictions. 12 2019.

[50] C. Andreopoulos et al. The GENIE Neutrino Monte Carlo Generator. *Nucl. Instrum. Meth. A*, 614:87–104, 2010. doi:10.1016/j.nima.2009.12.009.

[51] J. Nieves, J. E. Amaro, and M. Valverde. Inclusive quasielastic charged-current neutrino-nucleus reactions. *Phys. Rev. C*, 70:055503, Nov 2004. doi:10.1103/PhysRevC.70.055503.

[52] Aaron S. Meyer, Minerba Betancourt, Richard Gran, and Richard J. Hill. Deuterium target data for precision neutrino-nucleus cross sections. *Phys. Rev. D*, 93:113015, Jun 2016. doi:10.1103/PhysRevD.93.113015.

[53] J. Nieves, I. Ruiz Simo, and M. J. Vicente Vacas. Inclusive charged-current neutrino-nucleus reactions. *Phys. Rev. C*, 83:045501, Apr 2011. doi:10.1103/PhysRevC.83.045501.

[54] R. Gran, J. Nieves, F. Sanchez, and M. J. Vicente Vacas. Neutrino-nucleus quasi-elastic and 2p2h interactions up to 10 gev. *Phys. Rev. D*, 88:113007, Dec 2013. doi:10.1103/PhysRevD.88.113007.

[55] Ch. Berger and L. M. Sehgal. Lepton mass effects in single pion production by neutrinos. *Phys. Rev. D*, 76:113004, Dec 2007. doi:10.1103/PhysRevD.76.113004.

[56] Ch. Berger and L. M. Sehgal. Partially conserved axial vector current and coherent pion production by low energy neutrinos. *Phys. Rev. D*, 79:053003, Mar 2009. doi:10.1103/PhysRevD.79.053003.

[57] A Bodek and U. K. Yang. Higher twist, xi(omega) scaling, and effective LO PDFs for lepton scattering in the few GeV region. *J. Phys. G*, 29:1899–1906, 2003. doi:10.1088/0954-3899/29/8/369.

[58] T. Yang, C. Andreopoulos, H. Gallagher, K. Hoffmann, and P. Kehayias. A Hadronization Model for Few-GeV Neutrino Interactions. *Eur. Phys. J. C*, 63: 1–10, 2009. doi:10.1140/epjc/s10052-009-1094-z.

[59] L.L. Salcedo, E. Oset, M.J. Vicente-Vacas, and C. Garcia-Recio. Computer simulation of inclusive pion nuclear reactions. *Nuclear Physics A*, 484(3):557–592. ISSN 0375-9474. doi:10.1016/0375-9474(88)90310-7.

[60] Chris Hagmann, David Lange, and Douglas Wright. Cosmic-ray shower generator (cry) for monte carlo transport codes. volume 2, pages 1143 – 1146. ISBN 978-1-4244-0922-8. doi:10.1109/NSSMIC.2007.4437209.

[61] C. N. Chou. The nature of the saturation effect of fluorescent scintillators. *Phys. Rev.*, 87:904–905, Sep 1952. doi:10.1103/PhysRev.87.904.

[62] M. Baird, J. Bian, M. Messier, E. Niner, D. Rocco, and K. Sachdev. Event Reconstruction Techniques in NOvA. *J. Phys. Conf. Ser.*, 664(7):072035, 2015. doi:10.1088/1742-6596/664/7/072035.

[63] Martin Ester, Hans-Peter Kriegel, Jörg Sander, and Xiaowei Xu. A density-based algorithm for discovering clusters in large spatial databases with noise. In *Proceedings of the Second International Conference on Knowledge Discovery and Data Mining*, KDD'96, page 226–231. AAAI Press, 1996. doi:10.5555/3001460.3001507.

[64] Leandro A. F. Fernandes and Manuel Menezes de Oliveira Neto. Real-time line detection through an improved hough transform voting scheme. *Pattern Recognit.*, 41:299–314, 2008. doi:10.1016/j.patcog.2007.04.003. URL https://api.semanticscholar.org/CorpusID:5996185.

[65] Mattias Ohlsson, Carsten Peterson, and Alan L. Yuille. Track finding with deformable templates — the elastic arms approach. *Computer Physics Communications*, 71(1):77–98. ISSN 0010-4655. doi:10.1016/0010-4655(92)90074-9. URL https://www.sciencedirect.com/science/article/pii/0010465592900749.

[66] R. Krishnapuram and J.M. Keller. A possibilistic approach to clustering. *IEEE Transactions on Fuzzy Systems*, 1(2):98–110, 1993. doi:10.1109/91.227387.

[67] Miin-Shen Yang and Kuo-Lung Wu. Unsupervised possibilistic clustering. *Pattern Recognition*, 39(1):5–21. ISSN 0031-3203. doi:10.1016/j.patcog.2005.07.005. URL https://www.sciencedirect.com/science/article/pii/S0031320305002943.

[68] Jianming Bian, Hongyue Duyang, and Alexander Radovic. Blessing package for Neutrino-Electron Scattering and Coherent Pi0. NOVA Document 13862. URL https://nova-docdb.fnal.gov/cgi-bin/sso/ShowDocument?docid=13862. NOvA internal document.

[69] Nicholas Jacob Raddatz. *Measurement of Muon Neutrino Disappearance with*

Non-Fiducial Interactions in the NOνA Experiment. PhD thesis, Minnesota U., 2016.

[70] Michael David Baird. *An Analysis of Muon Neutrino Disappearance from the NuMI Beam Using an Optimal Track Fitter.* PhD thesis, Indiana U., 2015.

[71] G. Lutz. Optimum track fitting in the presence of multiple scattering. *NIM-A*, 273(1):349–361. ISSN 0168-9002. doi:10.1016/0168-9002(88)90836-4. URL https://www.sciencedirect.com/science/article/pii/0168900288908364.

[72] Brian Rebel. Window tracking algorithm for cosmic ray muons. NOVA Document 15977-v1. URL https://nova-docdb.fnal.gov/cgi-bin/sso/ShowDocument?docid=15977. NOvA internal document.

[73] Christian Szegedy, Wei Liu, Yangqing Jia, Pierre Sermanet, Scott Reed, Dragomir Anguelov, Dumitru Erhan, Vincent Vanhoucke, and Andrew Rabinovich. Going Deeper with Convolutions. *arXiv e-prints*, art. arXiv:1409.4842. doi:10.48550/arXiv.1409.4842.

[74] A. Aurisano, A. Radovic, D. Rocco, A. Himmel, M.D. Messier, E. Niner, G. Pawloski, F. Psihas, A. Sousa, and P. Vahle. A Convolutional Neural Network Neutrino Event Classifier. *JINST*, 11(09):P09001, 2016. doi:10.1088/1748-0221/11/09/P09001.

[75] Fernanda Psihas. Measurement of long baseline neutrino oscillations and improvements from deep learning. 1 2018. doi:10.2172/1437288. URL https://www.osti.gov/biblio/1437288.

[76] Prabhjot Singh. *Extraction of Neutrino Oscillation Parameters using a Simultaneous Fit of ν_μ Disappearance and ν_e Appearance data with the NOvA Experiment.* PhD thesis, University of Delhi, Dept. of Physics and Astrophysics, India, Delhi U., 9 2019.

[77] Ryan J. Nichol. Fibre brightness from cosmic muon data. NOVA Document 34909. URL https://nova-docdb.fnal.gov/cgi-bin/sso/ShowDocument?docid=34909. NOvA technical note.

[78] Prabhjot Singh. Attenuation Calibration of the NOvA Detectors. In *The 38th International Conference on High Energy Physics (ICHEP 2016)*, 2024. URL https://nova-docdb.fnal.gov/cgi-bin/sso/ShowDocument?docid=15840. (cited on 03.2024).

[79] Nitish Nayak. *A Joint Measurement of ν_μ-Disappearance and ν_e-Appearance in the NuMI beam using the NOvA Experiment.* PhD thesis, UC, Irvine (main), UC, Irvine, 2021.

[80] M. A. Acero et al. Adjusting neutrino interaction models and evaluating uncertainties using NOvA near detector data. *Eur. Phys. J. C*, 80(12):1119, 2020. doi:10.1140/epjc/s10052-020-08577-5.

[81] M. Valverde, J.E. Amaro, and J. Nieves. Theoretical uncertainties on quasielastic charged-current neutrino–nucleus cross sections. 638(4):325–332. ISSN 0370-2693. doi:10.1016/j.physletb.2006.05.053.

[82] Richard Gran. Model Uncertainties for Valencia RPA Effect for MINERvA. 5 2017.

[83] M. Tzanov et al. Precise measurement of neutrino and antineutrino differential cross sections. *Phys. Rev. D*, 74:012008, Jul 2006. doi:10.1103/PhysRevD.74.012008.

[84] M. Kordosky. Ramifications of intranuclear re-scattering in MINOS. 159:223–228. ISSN 0920-5632. doi:10.1016/j.nuclphysbps.2006.08.040. URL https://www.sciencedirect.com/science/article/pii/S0920563206005342. Proceedings of the 4th International Workshop on Neutrino-Nucleus Interactions in the Few-GeV Region.

[85] A. Mislivec et al. Measurement of total and differential cross sections of neutrino and antineutrino coherent $\pi^\pm$ production on carbon. *Phys. Rev. D*, 97(3):032014, 2018. doi:10.1103/PhysRevD.97.032014.

[86] E. S. Pinzon Guerra et al. Using world $\pi^\pm$-nucleus scattering data to constrain an intranuclear cascade model. *Phys. Rev. D*, 99:052007, Mar 2019. doi:10.1103/PhysRevD.99.052007.

[87] K. Abe et al. Measurement of neutrino and antineutrino oscillations by the t2k experiment including a new additional sample of ν_e interactions at the far detector. *Phys. Rev. D*, 96:092006, Nov 2017. doi:10.1103/PhysRevD.96.092006.

[88] OErika Catano-Mur, V Hewes, and Lisa Koerner. NOvA Production 5.1 Detector Systematics Executive Summary. NOVA Document 53225. URL https://nova-docdb.fnal.gov/cgi-bin/sso/ShowDocument?docid=53225. NOvA technical note.

[89] Juan Miguel Carceller. Calibration shape systematic: middle region and final parameterizations. NOVA Document 49986, April 2021. URL https://nova-docdb.fnal.gov/cgi-bin/sso/ShowDocument?docid=49986. NOvA internal document.

[90] V Hewes Oleg Samoylov. NOvA Production 5 Detector Simulation Changes and Systematics. NOVA Document 43935. URL https://nova-docdb.fnal.gov/cgi-bin/sso/ShowDocument?docid=43935. NOvA technical note.

[91] Patrick Huber et al. Snowmass Neutrino Frontier Report. In *Snowmass 2021*, 11 2022.

[92] E. Aprile et al. Excess electronic recoil events in XENON1T. *Phys. Rev. D*, 102:072004, . doi:10.1103/PhysRevD.102.072004.

[93] E. Aprile et al. Search for New Physics in Electronic Recoil Data from XENONnT. *Phys. Rev. Lett.*, 129:161805, . doi:10.1103/PhysRevLett.129.161805.

[94] M. Atzori Corona, W. M. Bonivento, M. Cadeddu, N. Cargioli, and F. Dordei. New constraint on neutrino magnetic moment and neutrino millicharge from LUX-ZEPLIN dark matter search results. *Phys. Rev. D*, 107:053001. doi:10.1103/PhysRevD.107.053001.

[95] M. Agostini et al. Limiting neutrino magnetic moments with Borexino Phase-II solar neutrino data. *Phys. Rev. D*, 96:091103. doi:10.1103/PhysRevD.96.091103.

[96] Amir N. Khan. Light new physics and neutrino electromagnetic interactions in XENONnT. *Physics Letters B*, 837:137650. ISSN 0370-

2693. doi:10.1016/j.physletb.2022.137650. URL https://www.sciencedirect.com/science/article/pii/S0370269322007845.

[97] K. S. Babu, Sudip Jana, and Manfred Lindner. Large Neutrino Magnetic Moments in the Light of Recent Experiments. *JHEP*, 10:040. doi:10.1007/JHEP10(2020)040.

[98] L. B. Auerbach et al. Measurement of electron-neutrino electron elastic scattering. *Phys. Rev. D*, 63:112001. doi:10.1103/PhysRevD.63.112001.

[99] D. A. Krakauer et al. Limits on the neutrino magnetic moment from a measurement of neutrino - electron elastic scattering. 252:177–180. doi:10.1016/0370-2693(90)91100-P.

[100] L. A. Ahrens et al. Determination of electroweak parameters from the elastic scattering of muon neutrinos and antineutrinos on electrons. *Phys. Rev. D*, 41:3297–3316, Jun 1990. doi:10.1103/PhysRevD.41.3297.

[101] P. Vilain et al. Experimental study of electromagnetic properties of the muon-neutrino in neutrino - electron scattering. *Phys. Lett. B*, 345:115–118, 1995. doi:10.1016/0370-2693(94)01678-6.

[102] Biao Wang. *Muon-Neutrino Electron Elastic Scattering and a Search for the Muon-Neutrino Magnetic Moment in the NOvA Near Detector.* PhD thesis. URL https://scholar.smu.edu/hum_sci_physics_etds/1.

[103] Wenjie Wu and Yiwen Xiao. Constraint of the Integrated Neutrino Flux from Neutrino-Electron Elastic Scattering in the NOvA Near Detector. NOVA Document 56383. URL https://nova-docdb.fnal.gov/cgi-bin/sso/ShowDocument?docid=56383. NOvA technical note.

[104] Athula Wickremasinghe, Wenjie Wu, and Yiwen Xiao. Status of the Measurement of Neutrino-Electron Elastic Scattering in the NOvA Near Detector. In *Neutrino 2022*. URL https://indico.kps.or.kr/event/30/contributions/738/.

[105] Barnali Brahma, Tyler Horoho, and Mu Wei. TechNote: Light Dark Matter Search with NOvA Near Detector. NOVA Document 59439. URL https:

//nova-docdb.fnal.gov/cgi-bin/sso/ShowDocument?docid=59439. NOvA technical note.

[106] Carlo Giunti and Alexander Studenikin. Neutrino electromagnetic interactions: A window to new physics. *Rev. Mod. Phys.*, 87:531–591, Jun 2015. doi:10.1103/RevModPhys.87.531.

[107] Boris Kayser. Majorana neutrinos and their electromagnetic properties. *Phys. Rev. D*, 26:1662–1670, Oct 1982. doi:10.1103/PhysRevD.26.1662.

[108] José F. Nieves. Electromagnetic properties of majorana neutrinos. *Phys. Rev. D*, 26:3152–3158, Dec 1982. doi:10.1103/PhysRevD.26.3152.

[109] Carlo Giunti, Julieta Gruszko, Benjamin Jones, Lisa Kaufman, Diana Parno, and Andrea Pocar. Report of the Topical Group on Neutrino Properties for Snowmass 2021. 9 2022.

[110] R. L. Workman and Others. Review of Particle Physics. *PTEP*, 2022:083C01, 2022. doi:10.1093/ptep/ptac097.

[111] Nicole F. Bell, Mikhail Gorchtein, Michael J. Ramsey-Musolf, Petr Vogel, and Peng Wang. Model independent bounds on magnetic moments of Majorana neutrinos. *Phys. Lett. B*, 642:377–383, 2006. doi:10.1016/j.physletb.2006.09.055.

[112] Nicole F. Bell, Vincenzo Cirigliano, Michael J. Ramsey-Musolf, Petr Vogel, and Mark B. Wise. How magnetic is the Dirac neutrino? *Phys. Rev. Lett.*, 95:151802, 2005. doi:10.1103/PhysRevLett.95.151802.

[113] M.C. Gonzalez-Garcia and Michele Maltoni. Phenomenology with Massive Neutrinos. *Phys. Rept.*, 460:1–129, 2008. doi:10.1016/j.physrep.2007.12.004.

[114] Carlo Giunti and Chung W. Kim. *Fundamentals of Neutrino Physics and Astrophysics*. 2007. ISBN 978-0-19-850871-7.

[115] P. Vogel and J. Engel. Neutrino electromagnetic form factors. *Phys. Rev. D*, 39:3378–3383, Jun 1989. doi:10.1103/PhysRevD.39.3378.

[116] E. Valencia et al. Constraint of the MINERνa medium energy neutrino flux using neutrino-electron elastic scattering. *Phys. Rev. D*, 100:092001, Nov 2019. doi:10.1103/PhysRevD.100.092001.

[117] Jens Erler and Shufang Su. The weak neutral current. 71:119–149. ISSN 0146-6410. doi:10.1016/j.ppnp.2013.03.004. URL https://www.sciencedirect.com/science/article/pii/S0146641013000239. Fundamental Symmetries in the Era of the LHC.

[118] D.Yu Bardin and V.A. Dokuchaeva. On one-loop electroweak corrections to neutrino-electron elastic scattering. 246(2):221–230. ISSN 0550-3213. doi:10.1016/0550-3213(84)90293-1. URL https://www.sciencedirect.com/science/article/pii/0550321384902931.

[119] Teresa Lackey. Data Quality Technical Note Prod5.1/2023. NOVA Document 59876. URL https://nova-docdb.fnal.gov/cgi-bin/sso/ShowDocument?docid=59876. NOvA technical note.

[120] Erin Ewart. Primary and Secondary Vertexing Update for February 2024 Collaboration Meeting. NOVA Document 61190, February 2024. URL https://nova-docdb.fnal.gov/cgi-bin/sso/ShowDocument?docid=61190. NOvA internal document.

[121] Leonidas Aliaga, Derek Doyle, Matthew Judah, Norm Buchanan, Linda Cremonesi, Mat Muether, and Jon Paley. Measurement of the Double-Differential Inclusive Electron-Neutrino Charged-Current Cross Section in the NOvA Near Detector. NOVA Document 37668, 04 2020. URL https://nova-docdb.fnal.gov/cgi-bin/sso/ShowDocument?docid=37668. NOvA technical note.

[122] Rene Brun et al. root-project/root: v6.22/08. URL https://doi.org/10.5281/zenodo.3895860.

[123] Andreas Hoecker, Peter Speckmayer, Joerg Stelzer, Jan Therhaag, Eckhard von Toerne, and Helge Voss. TMVA: Toolkit for Multivariate Data Analysis. *PoS*, ACAT:040, 2007.